Probing the Interplay Between Chemical Mechanisms and Crystal Growth in Synthesis using Sodium Yttrium Fluoride

Alexander B. Bard

A dissertation
submitted in partial fulfillment of the
requirements for the degree of

Doctor of Philosophy

University of Washington

2023

Reading Committee:

Peter J. Pauzauskie, Chair

Brandi M. Cossairt

James J. De Yoreo

Daniel R. Gamelin

Program Authorized to Offer Degree:
Department of Chemistry

University of Washington

Abstract

Probing the Interplay Between Chemical Mechanisms and Crystal Growth in Synthesis using Sodium Yttrium Fluoride

Alexander B. Bard

Chair of the Supervisory Committee:
Associate Professor Peter J. Pauzauskie
Department of Materials Science and Engineering

To fully understand crystal growth, we have to consider chemistry. To fully understand chemistry, we have to consider crystal growth. This dissertation aims to understand the relationship between these two processes that are too often thought of as independent. We also take a look at some of the techniques that can be used to study these processes and when and why one might choose one technique over another. The primary system in which we study these mechanisms is in the aqueous synthesis of sodium yttrium fluoride (NaYF). Here I present research in which we studied the nucleation and growth mechanisms during all stages of that synthesis, and in doing found multiple instances of non-classical crystallization that fundamentally alter not just how the crystals themselves form but also the chemical composition and phase of those crystals. Following the NaYF chapters, we take a look at the atom probe tomography (APT) of bulk diamond and the challenges that we face in making those measurements, allowing us to delve into a technique that is not heavily used but which could potentially allow us to study crystal growth and other processes in an entirely different way.

This dissertation begins with a deep dive into the theory that underlies the scientific questions that we're asking. This can be broken up into two parts: the synthesis and the measurement. In the discussion of the synthesis, I start with an overview of crystallization

theory, beginning with classical crystallization and the mathematical formulae and concepts developed by Gibbs and others that describe how crystals are "supposed" to grow, and then look toward all of the non-classical ways that crystals have also been observed to grow. I then give a background on NaYF—why it is important in the greater scientific community and to our group's research specifically, and why we should care about its crystallization process. In the discussion of measurement, I provide a brief overview of the history, physical basis, and current use of the two microscopic techniques that I used most in this dissertation: transmission electron microscopy (TEM) and APT. The goal of this discussion is to convey the importance of these processes and techniques to our research and provides the background necessary to understand why we did the experiments that we did.

The following four chapters describe the research that I have been conducting in my time here. Chapters 2-4 discuss the NaYF project, and Chapter 5 discusses the APT of diamond. We start our study of NaYF by using a combination of analytical TEM, powder X-ray diffraction (XRD), in situ liquid cell TEM, APT, and extended x-ray absorption fine structure (EXAFS) measurements to show that hexagonal NaYF nanowires form hydrothermally through a non-classical crystal growth mechanism involving the formation and subsequent oriented attachment of mesocrystals consisting of cubic (α) phase units. EXAFS spectroscopy also suggests that substitutional Yb^{3+} point defects within NaYF are distributed evenly throughout the crystal lattice without clustering, and also that they may exhibit selective substitution into one of the two possible trivalent yttrium sites in the unit cell for hydrothermally synthesized β-NaYF.

We then transition to a study of the initial nucleation of NaYF in water. Two-step crystallization mechanisms based on spinodal decomposition followed by nucleation are commonly observed both in the laboratory and in nature. While this pathway may require chemical reactions, subsequent nucleation and growth are often considered as separate, discrete events from the reaction itself. In this chapter, using both experimental measurements and

atomistic computational modeling, we report another step in the aqueous synthesis of sodium yttrium fluoride of solid state chemical diffusion, thus showing a mechanism of at least four discrete steps, including 1) the segregation of aqueous ions into a dense liquid phase, 2) the formation of an amorphous aggregate, 3) solid-state diffusion of sodium and fluoride ions into the amorphous aggregate toward a $NaYF_4$ stoichiometry, and 4) the crystallization of a stable nonstoichiometric cubic sodium yttrium fluoride phase. The penultimate step involves a continuous, gradual change of the solid phase's chemical stoichiometry from YF_3 toward $NaYF_4$. Unlike previously studied nucleation and growth mechanisms, the stoichiometry of the final solid phase evolves throughout the crystallization process rather than being determined at the time of the initial separation from solution. This novel four-step mechanism provides a new perspective into the nucleation and growth of many other crystalline materials given the ubiquity of nonstoichiometric compounds in nature.

Following this, we conclude our study of the NaYF system by examining its relationship with YF_3. In the previous chapter, we found that in the initial step of the aqueous NaYF synthesis, an amorphous YF_3 phase separates from solution but is unable to crystallize until enough NaF diffuses into the matrix that it can form cubic NaYF. This prompts the question: what happens if there isn't enough NaF left for that? We find that in that situation, the gel still initially forms, but then appears to dissolve away and then renucleate as orthorhombic YF_3, rather than nucleate within the solid gel phase as the NaYF does. This creates a "switch" mechanism of sorts in which the relative concentrations of the reactants can be used to select between two different products with a different composition and crystal phase from each other, and the mechanism by which that occurs is directly via the crystallization process, showing that the chemistry and the crystallization are fundamentally intertwined. We then delve deeper into the YF_3 nucleation process in which we observe with nuclear magnetic resonance spectroscopy (NMR) and predict with computational modeling that as the gel redissolves into the solution, it forms various solvated YF_n species that can interact to form the final

solid YF_3 product. Finally, we show with dynamic light scattering (DLS) that the growth rate of the YF_3 particles is not constant and likely involves some nonclassical processes that merit further study.

The final research chapter represents a departure from the NaYF system, and rather we consider the APT of bulk diamond. APT is a technique that allows us to map out atoms in a sample in three dimensions by field evaporating ions off of a sharp tip, assisted by a pulsed laser, and detecting them with a two-dimensional mass spectrometer with the third dimension being detected in time as a function of the laser pulse rate. This technique can be challenging for samples like diamond both in terms of sample preparation and the measurement itself. APT samples are typically prepared with a focused ion beam (FIB), but due to diamond's inherent hardness, it is difficult and time-consuming to mill bulk diamond, and the high beam dose needed to mill diamond introduces a considerable amount of damage. Once a sample is made, the measurement is also difficult due to the extremely high evaporation field of diamond, necessitating high voltages that introduce mechanical strain in the sample, often causing it to fracture. We address the fabrication problem by producing an array of tips using reactive ion etching to minimize the required interaction of the sample with the ion beam, and we consider strategies to improve data collection on diamond in APT. We find that diamond requires much higher pulse energies than most other materials in order to reduce the required voltage for field evaporation, but we show through computational modeling as well as experimental data that diamond is able to handle those increased pulse energies with negligible storage of heat, which is typically the greatest problem with high pulse energies. We were able to successfully collect APT data on diamond, showing the distribution of nitrogen and hydrogen, and we were also able to use our APT results to show the damage incurred by the FIB. These results show that APT can be a useful method for studying diamond, and that an optimization of the technique can reduce many of the problems classically associated with these measurements. Furthermore, this demonstrates a

unique potential application of diamond in APT as a sample mount. APT sample mounts should have low background and high thermal conductivity, and diamond would be an ideal material for this. As such, this potential application warrants further study.

This dissertation concludes by summarizing our results and, perhaps more importantly, by formally posing many of the questions that this research has helped us to uncover. A recurring theme among these projects is that these are complex systems that we are studying, and oftentimes every new thing we learn creates even more questions. This concept applies not just to these experiments but to all of science—many of the chemical and physical processes that occur in nature involve many steps and a high degree of interplay, and as such resist being fully characterized by simple models. From this perspective, as we consider NaYF or the APT of diamond, we can apply these lessons broadly to other systems and use them to learn more about how things happen in real life rather than how they happen in textbooks. It is my hope that the results in this dissertation nucleate many years of research into these fields so that we can make discoveries that I never could have imagined in my time here.

TABLE OF CONTENTS

LIST OF FIGURES

GLOSSARY

APT: Atom probe tomography

CNT: Classical nucleation theory

DLP: Dense liquid phase

DLS: Dynamic Light Scattering

EDS: Energy dispersive (X-ray) spectroscopy

EELS: Electron energy loss spectroscopy

ETEM: Environmental transmission electron microscopy

FIB: Focused ion beam (milling)

FIM: Field ion microscope

FWHM: Full width at half-maximum

LCTEM: Liquid cell transmission electron microscopy

MS: Mass spectrometry/spectrometer

NAYF: Sodium yttrium fluoride, in its natural (nonstoichiometric) state

NIR: Near infrared

OA: Oriented attachment (also can be used for objective aperture and oleic acid, but for the sake of clarity those are written out in full here)

PNC: Pre-nucleation cluster

SAXS: Small-angle X-ray scattering

SD: Spinodal decomposition

SEM: Scanning electron microscopy/microscope

STEM: Scanning transmission electron microscopy/microscope

TEM: Transmission electron microscopy/microscope

TOF: Time of flight (mass spectrometry)

UCNP: Upconverting nanoparticle (usually of NaYF)

XRD: X-ray diffraction, used in this dissertation generally to refer to powder diffraction as opposed to single-crystal diffraction unless otherwise specified

Some passages and figures have been adapted or reproduced in part or full with permission as needed from the following sources:

- Bard, A. B. et al. A Mechanistic Understanding of Nonclassical Crystal Growth in Hydrothermally Synthesized Sodium Yttrium Fluoride Nanowires. *Chemistry of Materials* **2020**, *32*, 2753–2763, DOI: 10.1021/acs.chemmater.9b04076

- Bard, A. B. et al. Chemically-Driven Multi-Step Crystallization in the Synthesis of Sodium Yttrium Fluoride Via a Porous, Electrochemically-Active Intermediate. *In Submission* **2023**

- Bard, A. B. et al. Concentration-Selective Nucleation "Switch" in the YF_3-$NaYF_4$ System. *In Preparation* **2023**

- Bard, A. B. et al. Microfabrication from Bulk and Measurement of Nanoscale Diamond Tips for Atom Probe Tomography. *In Preparation* **2023**

ACKNOWLEDGMENTS

While I am officially the sole author of this dissertation, the work contained within represents the collective efforts of many, many people who have been a part of my research career. While I could not possibly list each of the literally hundreds of people by name who in some small or large part contributed to the completion of my Ph.D, I would like to first acknowledge the innumerable people who at some point were friends, office-mates, professors, teachers, co-workers, collaborators, custodians, support staff, and administrators who allowed my Ph.D to proceed as smoothly as possible. That said, I would like to specifically thank each of the people who have come and gone from my research group in the time that I've been here, specifically Matt Crane, Elena Dobretsova, Greg Felsted, Andy Feng, Lars Forberger, Stuart Frazer, Abbie Ganas, Rachel Gariepy, Chaman Gupta, Sankhya Hirani, Matt Lim, Ivan Liu, Andrew Nuhaily, Anupum Pant, Alexey Soldatenko, Chris Woodburn, Xiaojing Xia, and Xuezhe Zhou. Graduate school can often be difficult, and having these excellent coworkers and friends has made the difficult times much more tolerable and the good times even better. Thank you for working with me over the years, making our office and lab a fun place to be, and most of all for laughing at my dumb jokes.

I would also like to thank all of my collaborators and coauthors on my published papers as well as those currently in progress, especially the many excellent collaborators from our years of successful work with PNNL. One of the great joys of science is that it is inherently a collaborative process, and I have been very fortunate to have many collaborators, all of whom have taught me something, and all of whom have been a

joy to work with. Their work made it possible to present these research findings and allowed us to answer questions that I could not have answered on my own. While my collaborators are too numerous to list by name here, every one of them is appreciated, and I owe each of them a drink. With that said, I would be remiss if I did not specifically thank Danny Perea and Steven Spurgeon for providing me access to their labs at the PNNL and the expertise to be able to use them. Their contribution not only vastly improved the quality of the data presented in this dissertation, but also vastly improved my quality as a scientist, allowing me to think about things in a way that I never would have otherwise.

The most consequential decision one makes in grad school is the choice of their advisor, and I have been very lucky to have Peter Pauzauskie as mine. When I first transferred to this group, I was just learning how to do research, and some weeks I felt like I hadn't achieved anything at all. The only reason I didn't crash and burn during that time was because no matter how garbage my research update was, Peter was unfailingly able to find something in it to get excited about and to motivate me to continue trying. That attitude has carried me through grad school and has permanently changed how I think about science. Furthermore, I cannot adequately express my appreciation for Peter's patience at times when I have insisted on being convinced that something is a good idea. I know that I can be opinionated at times, and it would be easy for an advisor to tell their students to just do it, but Peter has always been more than willing to work with me to come up with ideas that work for both of us, and I think we've done better science as a result of that.

There have also been many people outside of work who nonetheless helped me to succeed in grad school. First and foremost are my friends and family for supporting me during my Ph.D. They have kept me sane, and have welcomed me home whenever I decided to visit. My entire lab group would especially like to thank my parents, Ed

and Becky Bard, for instilling in me the wisdom that a person's worth is determined primarily by the quality of snacks they bring to group meeting. I also would especially like to thank my grandfather, Allen J. Bard, to whom this dissertation is dedicated, for introducing me to science at a young age, and who is without question the reason that I am in this field at all. While this likely means that I would have had a Real Job™ by now if not for him, I nonetheless am grateful for his encouragement that I pursue science and make the intellectual investment in graduate school. I also would like to acknowledge the many mentors I had during my undergraduate career at the University of Texas, especially my research coordinator Lauren DePue, who gave me the confidence at an early stage in my career to be able to pursue research.

Much of this work was completed during the COVID-19 pandemic, which had an impact that nobody would have expected at the time that I began my Ph.D, and which radically changed how we were able to do research during that time. While the pandemic affected us all in various ways, mostly negative, the people who kept our society running during that time were also those who were the most personally affected by the pandemic. Therefore I must acknowledge the contributions of the many healthcare and other essential workers for doing what they needed to do during the pandemic to allow the rest of us to live as normally as possible, as well as the many scientists who developed the vaccines that allowed us to return to normal. My science doesn't do that. Furthermore I acknowledge the work done by our union, UAW 4121, for taking collective action to ensure that I and other student employees can be fairly compensated and treated well during our time here.

Finally, I would like to thank my committee for taking the time to read through my dissertation and attend my defense, and for providing the necessary guidance after my general exam such that I could make the requisite progress in order to finish this dissertation.

DEDICATION

To Prof. Allen J. Bard, technically my first research advisor

Chapter 1

INTRODUCTION

Over the past several years, most of my waking life has been dedicated to studying the chemistry and crystal growth processes of sodium yttrium fluoride (NaYF). This, in fact, was not on purpose. As I will briefly discuss later, our group was originally studying NaYF as a laser cooling material, and we had noticed a few oddities about how the crystals were growing as we were synthesizing it. As we started looking more directly at the crystal growth processes, we started noticing more and more properties that were outright surprising, ultimately opening our eyes to a mechanism in which crystal growth and chemistry are fundamentally intertwined. Typically, chemists talk about mechanisms in terms of molecular bonds forming and breaking and electrons being transferred, while materials scientists talk about crystal growth in terms of unit cells assembling into larger structures. Rarely is it discussed that both of these processes occur simultaneously, with each inherently affecting the other.[5,6] It is especially profound that this is something we found entirely by accident. Perhaps we stumbled on an anomaly—maybe NaYF is just weird. But there are many, many papers in the literature about NaYF, and I have yet to find any that describe the processes we observed. If nobody has bothered to look for these processes in NaYF before, then it is probable that there are many other systems that could behave in "weird" ways that nobody has bothered to look for. Louis Pasteur's quote is often repeated that "in the fields of observation, chance favors only the prepared mind." This is arguably the basis of fundamental science. If you view NaYF as simply a vehicle for upconversion, then you will find it to be a very effective upconversion material, and there's nothing wrong with focusing on just that, but as we've found, there's so much more about NaYF that makes it interesting, and the fact that we learned these things about NaYF's crystal growth when we were just

looking to use it for laser cooling emphasizes the importance of actively pursuing the weird behaviors and surprising observations that we may encounter. If we just happened to stumble upon these observations about the NaYF system, one can't help but wonder* what other phenomena in other systems may be hiding in plain sight that might fundamentally alter our understanding of how they form.

1.1 Crystallization

For those of us who were classically trained in chemistry, it is easy to think of reactions only in the solution or gas phase. Much attention is given to free atoms, ions, and molecules. and how they interact with each other on a one-on-one basis, with solid products being viewed as "falling out of" the reaction, rather than as active participants. We were also taught that everything is chemistry—that all matter we interact with is a chemical which can undergo chemical reactions and interact with its surroundings. Yet the matter we interact with is, for the most part, solid. How do we reconcile the aqueous and gas phase chemistry we learned in class with the solid world we live in? Understanding how solids form and interact is key to understanding much of the universe around us, from the formation of planets[7] to the mineralization of our bones[8] to the production of nature's perfect foods.[9–11] It can also tell us why carbon can be so soft that it can be fractured simply by drawing a pencil across paper, yet it also comprises the hardest known natural material in diamond, despite having an identical chemical composition. To study the chemistry of the world we live in, it is essential to understand solids. However, in doing so we must not lose sight of the fundamental chemistry—the making and breaking of bonds—that allows everything to exist the way it does. Here we consider the processes by which solids form and evolve within an active, changing chemical environment. But first we must understand the principles by which they can form and evolve in the first place.

While crystals have been recognized since antiquity for their optical and morphological

*Unless you're a Nature reviewer

properties, it wasn't until the year 1611 that Kepler (of planetary motion fame) noted that snowflakes always have precisely six corners, whereas liquid water is shapeless.[12] He further considered that this structure resembles the pattern created by the close packing of spheres, and concluded that snowflakes must be formed from similar close packing of individual units, a concept that can still be seen in modern crystal theory. This concept further developed with the progression in understanding of atoms, molecules, and unit cells, and the development of experimental techniques such as X-ray diffraction. This ultimately became the reliable and mathematically-consistent study of crystal theory that is ubiquitous today, in which we know that crystalline solids have a unit cell that repeats in three dimensions in a symmetrical pattern. Crystallography is a field of its own with applications that span a wide array of physical and life sciences, but thinking all the way back to the questions Kepler asked about the snowflake over 400 years ago, one very fundamental point remains somewhat poorly understood: how can crystals even form in the first place? Even with a full understanding of modern chemistry, physics, and materials science, it boggles the mind (as it likely did Kepler's) that a disordered, highly entropic water vapor in the atmosphere can and does spontaneously arrange itself into perfect, ordered snowflakes. This concept, which seems so backwards from what we would expect from entropy, is yet ubiquitous not just in the heretofore-mentioned bad weather, but also in nearly every field of science and industry, and the importance of understanding crystallization is apparent to everyone from physicians[13] to jewelers[14] to microbiologists[15] to candy makers.[16] As such, it goes without saying that crystallization is a topic that merits study.

Crystallization can be broadly broken up into three distinct phases: nucleation, growth, and evolution. The nucleation step consists of the initial separation of the solid from the solution, the growth step consists, appropriately enough, of the growth of the nuclei into larger crystals, and the evolution step consists of the changes that occur after the crystals have formed. These processes can occur either "classically" or "non-classically." As non-classical crystallization inherently is defined as any crystallization process that does not proceed classically, this section will first discuss classical crystallization and then will discuss some

situations in which other, non-classical processes prevail.

Classical crystallization is defined here as classical nucleation and subsequent monomer-by-monomer growth of crystalline particles. Classical nucleation, in turn, is defined by classical nucleation theory (CNT), as originally described by Gibbs.[17] CNT describes the formation of crystal nuclei as the result of random fluctuations in concentration in a supersaturated solution. *[18] This means that in order to understand CNT, and in turn classical crystallization, we must understand solubility equilbria. It is taught in first year chemistry courses that solubility is an equilibrium and that solubility can be quantified for the monomer A with the equilibrium constant K_{sp} for the chemical equilibrium $A(aq) \rightleftharpoons A(s)$. What this means is that a solution with a reaction quotient Q that is higher than the K_{sp} for the particular equilibrium (i.e. is supersaturated) will precipitate. As a non-equilibrium process, we can therefore describe the Gibbs free energy of the nucleation as $\Delta G = -RTln\frac{Q}{K_{sp}}$, or from a monomeric standpoint, $\Delta\mu = -k_BTln\frac{Q}{K_{sp}}$. We can define the value of $ln\frac{Q}{K_{sp}}$ as the supersaturation, σ. In a supersaturated solution, this value will always be negative, and thus nucleation will occur spontaneously. However, this is resisted by the difficulty in forming an interface between the solid and solvated regions, which is quantified by the interfacial free energy, α. This can ultimately be put together into an equation for the nucleation rate J_n of

$$J_n = C \exp\left(-\frac{B\alpha^3}{\sigma^2}\right) \tag{1.1}$$

where C is a constant that depends on the material's properties and B is proportional to the volume of a monomer unit over temperature.[19] What this results in is that classically, crystallization occurs when nuclei reach a critical radius, r_c, at which point the bulk free energy will compensate the surface free energy, and the rate at which the nucleation can occur depends strongly on both the surface free energy and the supersaturation. Summarily, nuclei form due to random density fluctuations and those that reach a critical size (as determined by the energetics and the supersaturation of the solution) can continue growing until the

*This theory was actually written for gases, but is broadly applicable to the solution-based chemistry that forms the bulk of our research

solution reaches equilibrium. This explains how crystals "know" that other nuclei have formed—as crystals grow in solution, it reduces the supersaturation of the surrounding medium, which increases the critical radius needed to stabilize crystals, therefore causing larger particles to grow and smaller particles to dissolve away until the solution is no longer supersaturated—a process known as Ostwald ripening.[20*] This is a robust mathematical explanation of macroscale crystal growth and nucleation, but it's important to keep in mind that this theory was developed at a time when nanoscale crystal nuclei were not able to be viewed microscopically. Thus, any subtleties that occur prior to the crystals reaching a size that could be readily observed with the optical microscopes of the time would not have been detectable. As electron microscopy and other techniques have developed, it has been observed that many crystallization pathways cannot be strictly described by CNT. This is known, appropriately, as non-classical crystallization.

For the purposes of understanding non-classical crystallization, I find it most intuitive to consider the nucleation and the growth phases separately. Classical nucleation theory, as described above, is based on the idea that crystalline nuclei of a critical radius form spontaneously from random fluctuations in a supersaturated solution, and that the crystalline ordering of those nuclei is identical to that of the end product.[†] If this sounds like a contrived definition, that's because it largely is. At the time that CNT was developed, there was no way of directly observing these nuclei, so by necessity the theory was based solely on the macroscopic observation of crystal formation and thermodynamics. As such, the best explanation for the initial nucleation that could be asserted based on the information they had was that crystal nuclei form spontaneously as tiny versions of macroscopic crystals. Current technology has allowed us to, in many cases, observe the nucleation process directly, and what we've found is a considerably more complex picture than that of self-similar nuclei

---

*This is in fact a gross oversimplification of Ostwald ripening, which also has to account for things such as diffusion rates, but those details are beyond the scope of this discussion.

†More precisely, the ordering is identical to that of the initial crystalline product as determined by Ostwald's step rule.[21]

forming as a result of spontaneous nucleation.[22] This can be thought of as a realization of Ostwald's step rule on the microscopic scale—on the macroscopic scale, Ostwald's step rule predicts that other phases besides the thermodynamically stable phase will form first if there is less of an energy barrier to reach them.[21] It makes sense that this would be the case at the microscopic level as well. Especially for materials or conditions that would require a relatively large critical nucleus in order to grow, one would expect that the spontaneous formation of larger nuclei would be a relatively uncommon event,* and as such, if other pathways exist, it may be more favorable to proceed through those other pathways instead of classical nucleation. One such pathway is the formation of metastable molecular cluster intermediates. These clusters are even sometimes observed at undersaturated conditions, in this case termed pre-nucleation clusters (PNCs), which allow a separate pathway to nucleation.[24,25] Molecular cluster formation has been reported in calcium carbonate[26] and phosphate,[27] among other systems, and similar phenomena have been observed in the synthesis of quantum dots.[28,29] This is a very important phenomenon and one that may play a role in the YF_3 nucleation that we study in Chapter 4, however the chemistry and physics of their formation are largely beyond the scope of this dissertation.

Another nucleation mechanism that is often observed is the wonderfully ambiguously-named "two-step" nucleation. While this name is perhaps ambiguous by design to allow for some variation in complex systems, the general process of a two-step nucleation mechanism is one in which the energy barrier to crystallization is high enough that the solution is able to reach a sufficient level of supersaturation to reach the spinodal, resulting in a liquid-liquid phase separation (or spinodal decomposition) into a dense liquid phase (DLP) and a dilute liquid phase (not DLP, somewhat confusingly). The DLP is then able to spontaneously order into crystalline nuclei.[30] This is a particularly common mechanism for protein crystallization, owing to the lower likelihood of ordered nuclei randomly forming from large and irregular molecules.[30–32] However, this mechanism has also been predicted and/or observed in inter-

*In fact all nucleation events are by definition low-probability, but as the size of the critical nucleus increases it becomes much less likely for one to spontaneously form[23]

esting systems, such as calcium silicate,[33] calcium carbonate,[34,35] tungsten carbide,[36] iron oxide,[37] and many others. In principle, one should expect this mechanism to be favored in any system at a sufficiently high supersaturation.[38,39] In the original picture of two-step nucleation, the DLP is only metastable and thus exists only microscopically prior to crystallization, however some DLPs have been observed to be stable with respect to the solution, allowing for it to be observed as a bulk amorphous phase that precedes crystallization.[40–42]

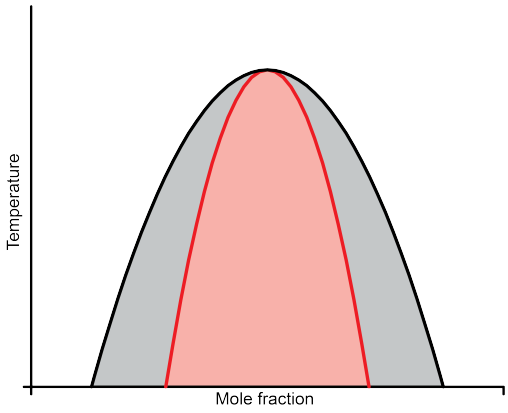

Figure 1.1: General illustration of a spinodal (red) and binodal (black) curve for an arbitrary system. At a given mole fraction and temperature, a two-component system can either exist in a single phase (i.e. the components are completely soluble, shown in the unshaded region), in two phases only (i.e. the components are completely insoluble, shown in the red shaded region), or metastable solvated and solid phases can coexist (shown in the grey shaded region). Because of this property, classical nucleation and growth occurs in the grey region whereas spinodal decomposition occurs in the red region.

To understand the driving forces behind this liquid-liquid phase separation, we need to understand the physics of spinodal decomposition (SD). The mathematics of this system were derived by Cahn and Hilliard in 1958,[43] and there is some discussion of the Cahn-Hilliard equation and its extension for multi-phase systems in Chapter 3, but for the purposes of this discussion, we can simplify this to a qualitiative discussion of a two-phase system (in wet chemistry terms, a solvent and solute). At a given temperature and mole fraction (i.e. concentration), a solute will either be stable (soluble) or unstable (insoluble). The curve that defines this limit is called the binodal (sometimes called the coexistence curve, shown in black in Figure 1.1). At any mole fraction and temperature below the binodal, the phases will eventually separate (i.e. the solution will precipitate). However, as discussed previously, nucleation is a rare event based on spontaneous fluctuations producing a sufficiently large particle, and as such, there is initially an energy barrier that precedes the successful nucleation of a solid phase. This allows for metastable supersaturated solution and solid phases to coexist temporarily, which is, by definition, a necessary condition for classical nucleation, and is physically realized as the existence of energetically-unfavored nuclei below the critical radius. However, as

the mole fraction gets further away from the binodal within the unstable region (i.e. the supersaturation increases), the energy barrier to nucleation (again realized as the critical radius of a nucleus) will decrease to zero, at which point any density fluctuation will cause the entire system to rapidly separate into two stable phases free of any energy barrier.[44] The curve that defines that limit is known as the spinodal (shown in red in Figure 1.1), and the rapid separation is known as spinodal decomposition. It is important to note that this initial phase that separates cannot be crystalline due to entropic considerations, and as such any ordering that is observed in the final product must necessarily occur as a subsequent step, separate from the initial phase separation.[45] As such, it then becomes clear that the spontaneous fluctuations model only applies above the spinodal curve, and below the spinodal we should instead expect a two-step nucleation mechanism in which a DLP will initially separate via SD, and depending on the stability of that initial separation phase, ordered regions will form within either nanoscale droplets in the case of a classical (metastable) two-step mechanism, or following the formation of a stable amorphous phase in the case of crystallization via SD.

As stated previously, in addition to non-classical nucleation, we can also observe non-classical growth of crystals following the initial formation. Classically, we would expect the growth rate to occur monomer-by-monomer based on Equation 1.1. Non-classical growth, therefore, is any way that crystals can grow other than that. While this necessarily refers to a wide variety of processes, the simplest and most commonly observed of these is the oriented attachment (OA) of nanocrystals,[46–48] first described by Penn and Banfield in 1998.[49] Instead of individual solvated ions attaching to single crystalline nuclei, in OA multiple nanocrystals will form and attach to each other along a crystallographic axis. This process is driven by Brownian motion, and therefore is more common in solutions with a high concentration of small, fast-moving nanocrystals in which collisions are more likely. A fairly robust macro-scale analogy for OA would be Lego bricks. One can think of each Lego as as an individual nanocrystal with a particular lattice. One can easily attach two Legos into a larger structure, but only at particular orientations. Furthermore, one could imagine a Lego that is stretched in some dimension, thus changing its "lattice spacing," and preventing it from attaching to a

Lego with a different "lattice spacing." In OA, particles can attach to each other, but only if there is a correctly-oriented lattice match at the surface where the particles meet. This process is highly size-dependent, with smaller particles undergoing OA much more readily than larger particles.[50] This is somewhat intuitive, as the collision rate is decreased and it is harder to perfectly align larger surfaces, which can result in particles that begin their growth process by an OA-mediated process and then convert to classical Ostwald ripening after they reach a certain size.[51] Because of this property, however, it can be easy to miss early OA-mediated growth mechanisms, which underscores the importance of studying these mechanisms directly rather than incidentally.

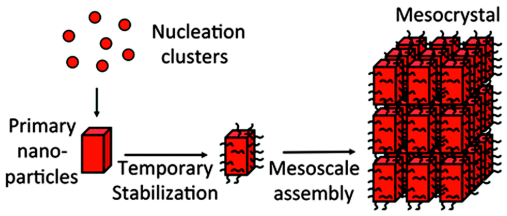

Figure 1.2: Illustration of mesocrystal formation by the oriented aggregation of ligated nanoparticles, adapted from the open access (CC BY 3.0) article by Sturm et al.[52]

Oriented attachment simply describes the attachment process, but there are multiple ways in which systems can reach a point at which OA can occur. In the most basic form of OA, the orientation step and the attachment step occur at the same time. Particles move in Brownian motion, and when they happen to collide at the correct orientation, they attach. This is the type of oriented attachment that was first observed by Penn and Banfield,[49] and is also the focus of the seminal *in situ* TEM study of OA systems by Dongsheng Li (discussed in more detail in Section 1.3.1).[53] However, the orientation step and the attachment step do not have to occur at the same time. This is especially true if the nanoparticles are passivated with a ligand that prevents the bare crystalline surfaces from coming into contact. Intuitively, one may not expect these systmes to be able to undergo OA, but by forming oriented aggregates known as mesocrystals that can then drive off their surface species and fuse together, they are able to overcome this limitation (Figure 1.2).[54–56] This mesocrystal model was first described by Cölfen in 2003,[57] and has since been observed in a wide array of systems both synthetic[1,58–61] and natural.[62–66] This mechanism is discussed in the context of our research in Chapter 2, and is yet another way in which we observe deviations from CNT in real-world systems. All of this taken together, it becomes obvious that crystallization is an incredibly complicated

process in which many different steps can occur in the process of forming crystals, and which can occur across scales ranging from the formation of molecular pre-nucleation clusters all the way to assemblies of micro-scale superstructures.[67,68] The initial separation from solution may occur via nucleation or it may occur via a liquid-liquid phase separation. Following that, crystals may grow by ion-by-ion classical growth, or they may grow via OA, which, in turn, can occur either as a result of random collisions or via the formation of mesocrystals. Complicating matters further, many of these processes can occur at the same time. Even this is a simplification, as all of these growth processes presuppose that the solvated monomer units are chemically the same as the final crystals (which I will discuss in depth in Chapters 3 and 4). This is not a safe assumption, and in fact the crystal growth and solution-phase chemistry are often inherently intertwined, with each fundamentally affecting the other. This is the crux of my thesis: that a purely physical view of crystal growth and a purely chemical view of precipitation reactions are both fundamentally incomplete explanations that cannot be assumed to occur independently of each other.

1.2 Sodium Yttrium Fluoride

The majority of the work presented in this dissertation focuses on the crystal growth processes of a particular material, sodium yttrium fluoride (NaYF). While it will be introduced in the context of the particular projects in later chapters, NaYF is important enough to the overall thesis that it merits the inclusion of its own section here. NaYF is a material that finds use in various forms in many areas of research, most of which focused on its luminescent properties when doped with lanthanide ions. In particular, when co-doped with Yb^{3+} and Er^{3+} ions, NaYF becomes the most efficient known NIR-Vis upconverting phosphor.[69] This superior upconversion capability combined with a wide tunability of upconverted wavelengths with different lanthanide dopants leads to an extremely wide variety of applications including but not limited to bioimaging,[70,71] solid-state

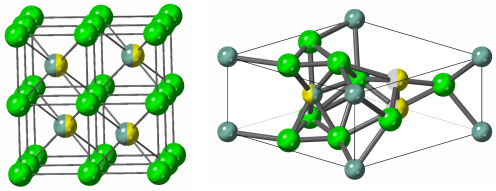

Figure 1.3: The two stable polymorphs of NaYF, cubic (α, left) and hexagonal (β, right). These are shown in the idealized $NaYF_4$ stoichiometry.

lighting,[72] photovoltaics,[73–75], anti-counterfeiting,[76–78] smart wound dressing,[79] gene editing,[80] brain stimulation,[81] fingerprinting,[82] nano-barcoding,[83] night vision,[84] the disinfection of medical masks used to protect against COVID-19,[85] and of greatest interest to our group, laser refrigeration.[86–89]

NaYF has two major polymorphs that are observed at ambient conditions: cubic (α) and hexagonal (β) (Figure 1.3). Historically, NaYF has been synthesized via high-temperature melt processes such as the Czochralski or Bridgman method.[90,91] These methods are capable of producing large single crystals of the cubic phase, however they are unable to produce single crystals of the hexagonal phase for general use due to large anisotropic thermal expansion coefficients that cause the crystals to break apart as they cool.[92] Nonetheless, melt-grown NaYF has been used for several detailed studies of the NaYF phase diagram.[92–96] These studies and others[97,98] reveal that NaYF is a nonstoichiometric material with a variable composition of $Na_{0.5-x}Y_{0.5+x}F_{2+2x}$ for the cubic phase and $Na_{3x}Y_{2-x}F_6$ for the hexagonal.[99] While the implications of this are to be discussed in later chapters, it is important to bring this up at this time because of the notation that is used throughout this dissertation. The typical notation that is used in the literature for this material is $NaYF_4$. However, due to the variable stoichiometry, this notation is not accurate at ambient conditions. At the same time, it would be unwieldy to write out the technically correct variable composition every time I reference the material,* so I choose to use the notation "NaYF" as an abbreviation rather than a chemical formula in order to emphasize and specifically acknowledge this point.

While melt-grown NaYF has been instrumental for much of the fundamental study of the material's properties, it cannot produce usable β-NaYF single crystals, and it also requires extreme conditions for its synthesis. This, along with the increase in focus in nanoscience throughout the scientific community over the past 20 years,[100] has made solution-based syntheses of nanoscale NaYF particles much more prevalent both in the fundamental science and especially in the applications literature.[101–103] Solution-based synthesis typically proceeds

*297 times, if you must know

through versions of one of two general processes: the solvothermal (or hydrothermal when aqueous) route, which reacts any of several precursor salts in a solvent that is heated in a sealed vessel, or the thermolytic route, in which trifluoroacetates (typically) of sodium and yttrium are heated under an inert atmosphere until they decompose, forming NaYF nanoparticles.[104] These methods have their own uses to which they are best suited—the thermolytic method, for example, excels at quickly and scalably making monodisperse, small β-NaYF particles,[105] whereas the solvothermal method is generally more versatile, especially for shape and phase control of the final particles, and also allows the reaction to proceed in water,[106] which is ideal for green chemistry techniques and also limits the exposure of the particles to organic species. A more detailed study of the process by which one version of the hydrothermal synthesis proceeds is discussed in Chapter 2. Another method that is sometimes used is simple precipitation from solution at ambient pressure and often temperature. This method is rarely used for applications due to difficulty in controlling the size and shape of the particles,[106] but it can be useful in studying crystal growth processes and for quickly synthesizing large amounts of material, particularly in the α phase, as we will show in Chapter 3. While other synthetic routes certainly exist, it is helpful to understand these commonly-used syntheses and the properties that result from each of them when reading a paper or designing an experiment.

In our group, the primary intended application for the NaYF materials we synthesize is laser cooling (also referred to as laser or optical refrigeration) applications. While the precise physics surrounding laser cooling are largely beyond the scope of this particular thesis, it can be useful to have a basic understanding of the process in order to understand what may be important for a synthesis of NaYF for that purpose. Laser cooling in solids was first demonstrated by Epstein in 1995,[107], and has since been demonstrated in many crystalline fluoride materials doped with lanthanides,[108–113] including NaYF.[88,89,114] Put simply, the ground and excited states of a particular transition (in this case for Yb^{3+}) are further split into vibrational energy states, on which the electrons reside in a Boltzmann distribution. This means that the emitted photons can have a slightly different energy than the photons

used to excite the transition. Most of the time the emitted photon is lower in energy than the excitation photon (referred to as a Stokes shift), which results in the resulting energy being dispersed non-radiatively into the lattice. However some photons can experience an anti-Stokes shift, in which the emitted photon has a higher energy than the excitation photon. Due to the conservation of energy principle, this additional energy must be extracted from the crystal lattice. By choosing an excitation wavelength that limits the only possible shifts to anti-Stokes (Figure 1.4), energy will be extracted from the lattice and the lattice will cool.[108]

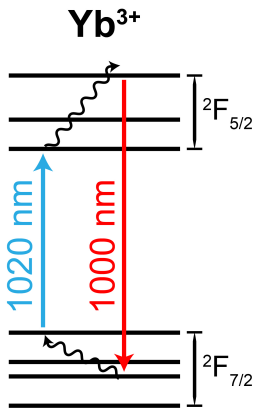

Figure 1.4: Energy level diagram showing a 1020 nm photon being used to cool a lattice containing Yb^{3+} ions

What this means for those of us who are concerned with synthesis is that we want a material that has a minimum energy transition that is close to the energy of a standard commercial laser, and which does not have any external sources of heating. The former is a property of the the dopant and its crystal field and thus is not strongly affected by the particulars of the synthesis. However the latter is a very important concern when synthesizing materials. External heating typically results from background absorption from the lattice, which may come from such sources as organic impurities or coatings, hydroxyl groups, lattice defects, density fluctuations, and any number of other components that would cause the host lattice or coating to have a nonzero absorption coefficient at the excitation wavelength.[115] Thus, the most important factor for a material to be used for laser cooling, assuming it already has an appropriate transition, is that the base lattice is as transparent as possible at the wavelength of that transition. One factor to consider is particle size—ligands, contaminants, and inherent surface reconstructions can cause the particles to absorb radiation—so it can be more challenging to cool smaller particles with a higher surface area to volume ratio.[116] Despite this, there has been significant research as of late on the laser cooling of nanoparticles.[117–119] Even so, it is harder to cool extremely small particles, and for these reasons, the thermolytic method, which produces very small particles and inherently incorporates organic contaminants, is not an ideal method for synthesizing laser cooling particles. As such, we focus on the hydrothermal and simple

precipitation methods to synthesize the materials in our work. However, these methods still have challenges—larger crystals contain more crystalline defects, materials that are synthesized in water tend to incorporate oxides and hydroxides, and as will be discussed in detail, the processes by which these form are anything but simple. As such, it is imperative that we understand the crystal growth mechanisms for these NaYF syntheses in detail so that the sources of heating can be addressed with surgical precision in an effort to improve the cooling efficiency up to its theoretical limit.

One final consideration regarding the fundamental chemistry of NaYF that is often overlooked is that of its relationship to YF_3. Ask anybody in a freshman chemistry course what happens when you react NaF and YCl_3, and they will write the reaction $3NaF(aq) + YCl_3(aq) \longrightarrow YF_3(s) + 3NaCl(aq)$.* Technically, they would be right, but only sometimes.[120] This is, of course, because we also observe the reaction $4NaF(aq) + YCl_3(aq) \longrightarrow NaYF_4(s) + 3NaCl$. To complicate matters further, as we've established, the stoichiometry of NaYF is variable, with true compositions as described earlier in this section. There are also reports of cubic YF_3 in the literature that is largely isostructural to cubic NaYF. This leads to a view of cubic NaYF as being akin to a solid solution of cubic YF_3 and NaF. But as we discuss in Chapter 3, calculations show that cubic YF_3 cannot exist with the reported crystal structure, leading to an updated view that cubic NaYF in fact is best viewed as being *the stable form* of cubic YF_3.† So to return to the original question of what happens when NaF and YCl_3 are reacted, we in fact have three possible solid products: cubic NaYF, hexagonal NaYF, and orthorhombic YF_3. And in fact we can isolate relatively pure samples of each depending on the reaction conditions. By studying these mechanisms, we've found that the reaction pathways that select for these products (the chemical mechanisms) are inherently based in crystallization and the formation of solid-state intermediates via processes such as spinodal decomposition and oriented attachment, each of which is a realization of Ostwald's step rule

*As somebody who has taught general chemistry classes, I admit that some may come up with more creative answers to this question.

†This is also true of NaYF's analogues including KYF and $(NH_4)YF$.

not only in terms of crystal structure but also chemical composition. This again showcases the point that crystallization and chemistry should be considered together, and at least in the case of NaYF, one would not be able to reach an accurate conclusion about its formation by considering the two processes separately.

1.3 Microscopy and Microanalysis

There are, of course, innumerable experimental methods that one could use to investigate the NaYF crystal growth process, and indeed we used many of them in our own work in order to paint a comprehensive picture of the process. However, one might ultimately respond to claims of crystal growth processes the same way they might respond to a fanciful story on the internet: pics or it didn't happen.[121] In all seriousness, the most powerful tools we have to watch crystal growth processes are those which allow us to literally watch crystals grow. When Gibbs first described crystal growth in the 19th century, he had never seen a nanocrystal: nobody had. The best microscopes at the time were limited by the diffraction limit of visible light, making it physically impossible to image features below about half a micron. This meant that any discussion of classical nucleation theory or the ion-by-ion growth mechanism was purely theoretical. That many systems are now known to proceed via classical crystallization mechanisms is a remarkable testament to the insight of these early scientists. Beyond crystal growth, there are so many other principles in chemistry and materials science that were purely theoretical, only to be confirmed decades or centuries later with microscopic and microanalytic techniques. One need not look further than atomic theory itself, which was painstakingly developed through philosophy and clever experimentation dating all the way back to Democritus in Ancient Greece, in the fifth century B.C.E. Atoms were first imaged directly by Erwin Müller using the field ion microscope (FIM) nearly 2500 years later, in 1955 C.E. (Figure 1.5).[122] Today, I can take 50 atomic-resolution images of almost any nanomaterial on the transmission electron microscope (TEM) and be finished in time for lunch (and I am not an early riser). What could once only be philosophized about can now be imaged as easily as any photograph.

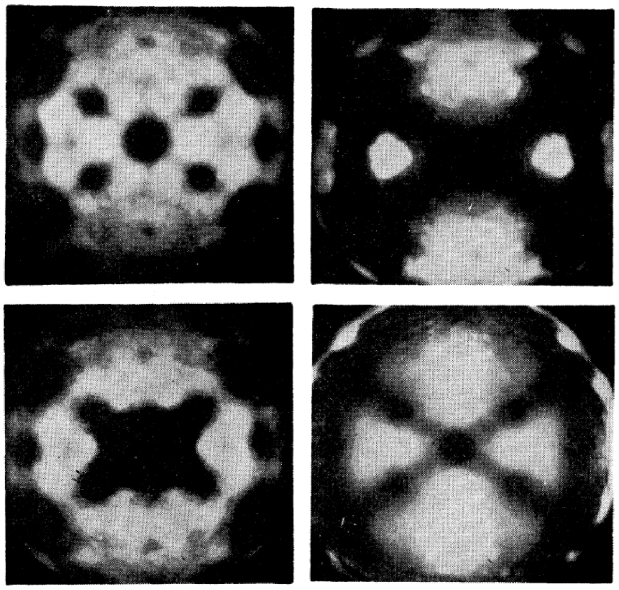

Figure 1.5: The first reported atomic resolution images, collected with FIM by Erwin Müller. Figure reprinted with permission from Müller, E. W. Field Desorption.*Physical Review* **1956**, *102*, 618–624, DOI: 10.1103/PhysRev.102.618 Copyright 1956 by the American Physical Society.

As impressive it is that microscopic techniques have been able to confirm ancient wisdom, it should also come as no surprise that it has also revealed nuances in certain systems that would not necessarily have been predicted with classical methods. Relevant to this work, of course, is the earlier-discussed 1998 discovery of the oriented attachment crystal growth mechanism by Penn and Banfield using TEM.[49] While TEM has been used to show particles growing classically, notably and very beautifully by the Frances Ross group,[123–127] other novel methods of crystal growth have also been directly observed in ways that would not have been possible before, of course by the aforementioned Penn and Banfield study, as well, notably, as by our colleague Dongsheng Li.[53,128] This direct insight motivates the use of microscopy as a primary method to study crystal growth processes. While one may casually use the terms "microscopy" and "microanalysis" interchangeably, or may use either as an umbrella term, strictly, "microscopy" refers to imaging whereas "microanalysis" refers to the measurement of chemical properties at that scale. To avoid cumbersome text, however, in this work, "microscopy" and its derivatives can be understood as an umbrella term that encompasses both the strict definitions of "microscopy" and "microanalysis" unless otherwise specified.

Microscopy as a field refers to a massive range of techniques that allow for the structural characterization at the microscopic or nanoscopic scale. This term is not specific to the method of making those measurements, allowing techniques that bear little superficial resemblance to each other to all be used in this context. The most ubiquitous of these, of course, is optical microscopy, which is a technique most of us were introduced to as young children. Optical

microscopy derives from the same principles of optical lenses, which have been known since antiquity. These single lenses, when well-crafted, can achieve high levels of magnification and allow for the study of single cells and microbes, a field that was first developed by the early microscopist Antonie van Leeuwenhoek.[129] The development of compound lenses around the 17th century brought the field of optical microscopy roughly to where it is today (disregarding techniques for improving contrast such as fluorescence and polarization). While the quality of lenses and imaging techniques have improved in the past 400 years, optical microscopy reaches a fundamental limit when the particles being studied approach the size on the order of and proportional to a single wavelength of light. This is known as the diffraction limit, which for an average wavelength of visible light is roughly a quarter of a micron. Regardless of the theoretical magnification of the lens system, it is impossible to optically image a feature in the visible spectrum that is smaller than the diffraction limit.* What this implies, though, is that smaller features can theoretically be imaged by shorter wavelengths of radiation. For various physical and historical reasons (to be discussed in more depth in Section 1.3.1) electron beams, which have a wavelength on the order of picometers, are typically used for this purpose. Thus, electron microscopes are able to resolve features as small as individual atoms. Other forms of microscopy also have similarly high resolution but radically different ways of magnifying the sample. FIM (discussed further in Section 1.3.2) was the first method of to achieve atomic resolution, and works by field evaporating ions off of a sharp point toward a 2D detector, and using the curved shape of the tip itself to create the magnification. Finally, one can also very precisely measure surfaces at atomic resolution using scanning probe microscopy, which works by passing an atomically-sharp tip over a specimen and measuring its interaction with the surface in varying ways. Scanning probe microscopy encompasses a set of very powerful techniques that can be used to precisely study crystal growth (among other things)[130–132] on

*While there are super-resolution techniques that are able to get around this theoretical limit in various ways and which are commonly used in biology, typically exploiting the properties of fluorophores in postprocessing, these techniques are beyond the scope of this work, and generally don't break the diffraction limit so much as circumvent it to an extent

an atomically flat surface, in some cases even *in situ*,[133] however because the crystal growth that I focus on here does not necessarily occur on an atomically flat surface, these techniques are largely beyond the scope of this work.

1.3.1 Transmission Electron Microscopy

Physical Basis

Due to its ability to routinely collect structural information at the nanoscale, nearly all of the work in this dissertation relies heavily on TEM data. As previously discussed, the TEM is, in concept, identical in operation to a standard desktop optical microscope, in that a source of radiation is passed through a sample and then magnified through a series of lenses in order to be viewed by the user. However, instead of using visible light as the radiation source, the TEM uses an electron beam, with wavelengths on the order of x-rays, in order to reduce the diffraction limit to below an atomic radius. The astute reader may notice, however, that while visible light is purely electromagnetic radiation, electrons are subatomic particles that have mass. This means that electrons, as they pass through a material, will lose momentum, and thus can only be used to image very thin samples in an ultra-high vacuum. One may reasonably wonder then why we use electrons rather than X-rays in these microscopes. This is a practical decision—while X-ray microscopes do exist, they are unusual relative to electron microscopes because it is extremely difficult to focus X-rays. This is easily understood by considering the colloquial usage of the word "X-ray." We associate X-rays with medical internal imaging because X-rays cannot be appreciably refracted by solids, so they can pass directly through the body. X-rays pass through things. It's what they do. This creates a challenge, however, in that they also pass directly through lenses without being refracted (i.e. without being focused).[134] Electrons, of course, would not be able to pass through a traditional glass lens at all, but their properties make them much more amenable to precise focusing using electromagnetic lenses. This property was first described in Ernst Ruska's undergraduate

thesis* in 1931, who went on to successfully assemble the first electron microscope during his Ph.D, which he completed in 1933.† At that time, the resolution was no better than that of the already existing optical microscopes (Figure 1.6), but nonetheless the ability to focus electron beams and image samples was a major breakthrough in the field of microscopy and for the first time eliminated the diffraction limit as the limiting factor for microscopic imaging.

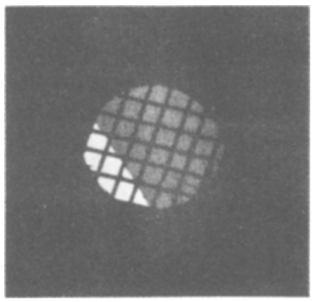

Figure 1.6: One of the first TEM images ever taken by Ernst Ruska and Bodo von Borries, of a molybdenum mesh with holes of 142 μm and a wire thickness of 30 μm. Reproduced with permission from Springer Nature.[135]

This concept of breaking the diffraction limit of optical microscopes by using electrons is so fundamental to the field of electron microscopy that it's worth spending time to fully understand why electron beams (sometimes referred to as "cathode rays") are such a good option as a source of radiation for microscopy. To understand this, we need to think back to the concept of wave-particle duality: a concept that I was certain I would never touch again after taking Physical Chemistry 2 in my undergraduate studies. For the purposes of electron microscopy, it is typically more convenient to think of the electron beam used for imaging as a wave, similar to a laser beam. However, we also know that electrons are particles with a negative charge and a nonzero mass (this behavior as a charged particle, as discussed previously, is what allows them to be focused with electromagnetic lenses, unlike X-rays at the same wavelength). As such, we can calculate the wavelength, λ, of the particle wave using De Broglie's equation, $\lambda = \frac{h}{p}$, where h corresponds to Planck's constant and p is the momentum of the particle.[136] Momentum is classically defined as $p = mv$, where m is the mass of the particle and v is its velocity, which, in the case of electron microscopy, is defined by the accelerating voltage of the microscope (200 kV being typical, though there is variation on different microscopes used for different purposes). Therefore, De Broglie's equation can be rewritten as $\lambda = \frac{h}{mv}$. Substituting

*Damn showoff.

†Damn showoff.

momentum into this equation will ultimately result in the equation $\lambda = \frac{h}{\sqrt{2meV}}$.[137] One could then use this equation to calculate the wavelength of the electron beam. However, if one were to do that, one would be, regrettably, wrong. This is due to the very annoying property of energy to convert to mass when particles move at high speeds.[138] At speeds to which we are generally accustomed, this contribution is not significant, but the electrons in a TEM move at a speed that can only be described as ludicrous,[139] on the same order of magnitude as the speed of light, and as such, the relativistic contribution cannot be ignored.[137] This means that we have to use the equation that almost everybody can recite and almost nobody can explain: $E = mc^2$.*† The full derivation of the relativistic momentum equation can be found in Appendix A, but the equation that results from including this relativistic contribution is as follows:

$$\lambda = \frac{h}{\sqrt{2meV(1 + \frac{eV}{2mc^2})}} \tag{1.2}$$

In Equation 1.2, all of the variables are fundamental constants of the electron except V, which is the acceleration voltage of the microscope. Therefore, for a typical 200 kV microscope, we can calculate the wavelength of the electron to be 2.51 pm, an order of magnitude smaller than the covalent radius of a helium atom, which means that the diffraction limit is not a concern for atomic resolution TEM.

Even though TEMs are not diffraction limited, there are nonetheless other factors that limit the resolution of conventional TEMs. These aberrations are similar to aberrations encountered in much of optical microscopy: as with light, electron beams experience both spherical aberration, in which the beam is imperfectly focused due to the shape of the lens,

*In reality this extended discussion of the relativistic contribution to the momentum when calculating the wavelength of the electron beam in the TEM is probably overkill as far as the scope of this thesis about crystal growth is concerned. However most people only get to write at most one dissertation in their lifetime, and as someone who has been a science nerd for nearly 30 years, I could not pass up this opportunity to use $E = mc^2$ somewhere in mine.

†I am not proud of the amount of time I invested in setting up the above joke.

and chromatic aberration, in which different energies of radiation are focused to different points by the same lens. Chromatic aberration can be addressed fairly straightforwardly, by monochromating the beam, however spherical aberration is a more complicated challenge. In optical microscopes, one can theoretically grind a glass lens to the exact specifications needed to perfectly focus a microscope, and thus spherical aberrations significant enough to limit the resolution are only seen in cheap and/or novelty microscopes. However, because electron optics are not manufactured objects but rather an electromagnetic field in space, their "shape" cannot be fine-tuned the way that glass lenses can, and thus conventional electron microscopes are at the mercy of the best focusing that the lenses can do, which one review described as "the equivalent [of] something like the bottom of a beer glass."[140*]

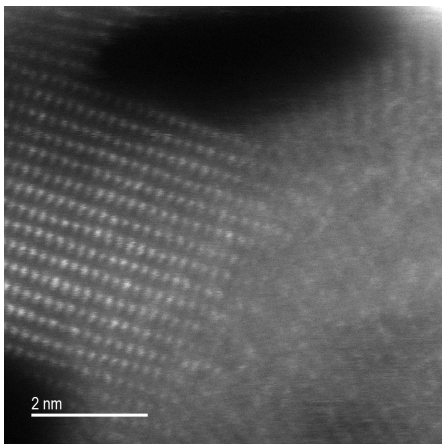

Figure 1.7: An aberration-corrected STEM image of the NaYF gel with sub-Ångstrom resolution, taken on the GRAND ARM at PNNL. Original work.

These spherical aberrations were determined by Scherzer in 1936 to be fundamental and unavoidable,[141] but just eleven years later he was able to show that these aberrations could theoretically be circumvented.[142,143] In 1997, 50 years after Scherzer showed that aberration correction was possible, the first aberration-corrected microscope was developed at the European Molecular Biology Laboratory in Heidelberg.[144] This emphasizes the technical difficulty of achieving aberration correction in a TEM. The specific physics of why aberration correction works is well beyond the scope of this dissertation. However, to simplify greatly, Scherzer's theorem relies on the assumption that the beam is rotationally symmetric, among other assumptions, and he was able to mathematically overcome the aberrations by lifting these assumptions.[143] Thus, the next 50 years of experimental research were spent trying to create a system that could modify the beam in those ways. Today, aberration-corrected microscopes, while still expensive specialty products, can be routinely produced and used as

*Indeed I have tested this hypothesis many times after late nights analyzing TEM data

facilities instruments in both TEM and STEM mode with sub-Angstrom resolution, including (under ideal conditions) atomic-resolution atomic analysis. While aberration-correction is not necessary for the majority of the microscopy that we do, and therefore most of our routine microscopy is done on uncorrected microscopes, I have had the opportunity to spend some time using a corrected microscope to collect STEM data on some of my samples (Figure 1.7), and it is truly amazing to see what kind of resolution is possible. I often have found that on the corrected microscope, many of the poor-quality throwaway images I've taken while attempting to focus are still much higher resolution than what can easily be achieved on a standard microscope, and thus for certain purposes, access to an aberration-corrected microscope can be extremely useful. It boggles the mind that one can routinely take pictures not just of atoms, but of the space between atoms. Democritus would be astounded.

TEM in context

Given the ubiquity of TEM in my research, it is undoubtedly important to understand the physics behind its operation in order to understand how it interacts with the material and how to interpret data. That being said, TEM is fundamentally an imaging technique, and the reality is that most of the work I (and most chemists) do with it focuses more on the collection and interpretation of high-resolution image data rather than worrying about how the electron beam passes through the column. As such, this section will focus more on the imaging and analysis techniques that help us to understand the processes of crystal growth (and other chemical processes) in various ways.

Perhaps the most widely used and fundamental of these techniques is electron diffraction. As noted previously, electron beams have a similar wavelength to x-rays. Because of this, electron beams interact with matter similarly to x-rays, most importantly in that they can be diffracted. While the physics of diffraction in general are largely beyond the scope of this dissertation, very briefly, the concept of using crystals as a "diffraction grating" for radiation of a wavelength comparable to the lattice spacing was first described by Max von

Laue in 1912.[145*] This discovery was quantified the following year by the father and son team William and Lawrence Bragg, who realized that x-rays would only be diffracted by a crystal lattice at certain angles, as described by the Bragg equation, $n\lambda = 2dsin\theta$.[146†] By carefully measuring the angles to which the x-rays are diffracted, this can tell us where the atoms are located within the crystal lattice. This effect is also observed in the TEM simply by changing the focus of the beam. In imaging mode, the diffracted electrons are either focused back onto the image or blocked by the objective aperture. In diffraction mode, however, the image is focused to a single point and the diffracted electrons are offset from the direct beam by their Bragg angle. While it is unusual (though not unheard of)[147–150] to solve entire crystal structures using electron diffraction due to the fewer number of visible diffraction spots relative to x-rays as well as the damaging effects of the electron beam on the sample after the repeated exposure required for a full crystal structure, electron diffraction is an extremely useful technique to identify local crystal phases and to confirm expected crystal structures at the hyper-local scale. Electron diffraction, like x-ray diffraction, can also be used to measure multiple crystallites in random orientations, with the peaks being integrated radially to produce a local "powder pattern." One technique that electron diffraction uniquely allows is dark field imaging. As previously mentioned, in imaging mode, the diffracted beam can be blocked by the objective aperture, allowing only the direct beam to form the image. This is usually done to increase contrast by darkening the strongly

---

*Many of the scientists cited in this research lived in Germany in the years preceding and during the Second World War. Though few actively supported the Nazis, Laue stands out as somebody who went beyond just believing the right thing but rather supported his views with his actions. Laue risked his career, and potentially his life, by openly opposing and refusing to collaborate with the Nazis, and he helped his Jewish colleagues in Germany to escape to safety. Following the war, he was instrumental in restoring Germany's ability to contribute to the international body of science. Laue's moral conviction in the most dire of situations and his patriotic dedication to do science in a better version of his homeland should be an inspiration to us all.

†The Braggs shared the 1915 Nobel Prize for this discovery, with the younger Bragg receiving his prize at the age of 25. Damn showoff.

scattering objects in the image. However, if instead of selecting the direct beam with the objective aperture, one were to select a diffraction spot, this would allow only diffracted electrons to form the image (or, more precisely, electrons scattered to the angle allowed by the objective aperture). As a result instead of the sample appearing dark on a bright background, the background will appear dark and the image of the sample will appear bright.

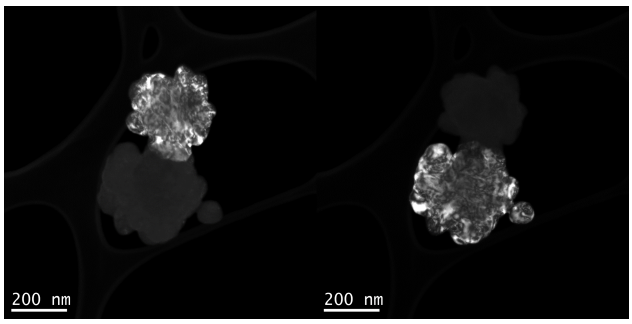

Figure 1.8: Dark field images of two separate cubic NaYF single crystals showing the ability to select diffraction spots from two separate crystals. Original work.

Due to diffraction being a relatively low-probability event, these images are much fainter and much lower in resolution than bright field imaging, however this technique is nonetheless quite powerful for those of us who study nanocrystals. Because particles with a different crystal structure or in a different orientation will diffract to different spots, this method can be used to image and select individual single crystalline domains, as seen in Figure 1.8. This is extremely valuable in studying irregularly-shaped particles as well as processes like oriented attachment that rely on crystallographic alignment.

Electron diffraction gives local information about crystal structures, which, of course, indirectly gives information about the local chemical environment. However, many materials have similar crystal structures, and not all materials are crystalline, or have well-enough defined crystalline domains to be able to definitively assign peaks. For that reason, it is also important to consider other methods of studying the local chemistry of materials using the TEM. Because electrons have similar energies to x-rays, the electron beam can also be used for spectroscopy. The principle of electron spectroscopy (and its analogue, x-ray spectroscopy) is that the beam will induce the ejection of an electron from the sample. This process absorbs a characteristic amount of energy from the beam depending on the particular electron that was ejected, which can be measured as a form of absorption spectroscopy called electron energy loss spectroscopy (EELS).[151] Following the loss of the electron from the material, higher-energy electrons will fill the hole left by the electron that was ejected, which releases

energy in the form of x-rays, which can be measured in a form of emission spectroscopy called energy-dispersive x-ray scattering spectroscopy (EDS).[152*] Either of these techniques can be used to identify composition locally by measuring the characteristic absorption or emission of a given element, and this information can be used to identify samples, map concentration gradients, identify interfaces, and do many other things that are of interest to a chemical microscopist. There are various reasons why one might choose to use EELS vs. EDS: EDS tends to be somewhat more user friendly and better at identifying heavier elements, whereas EELS can give information about bonding and electronic structures. In practice, we typically use EDS because the microscope in our facility happens to have an EDS detector.

Another issue that plagues the electron microscopist is that the sample typically needs to be dry and mounted on a grid in an ultra-high vacuum. This is a fundamental limitation of the technique due to the fact that electrons have mass, and therefore lose momentum as they pass through matter, unlike their analogous massless x-rays, which, of course, can pass all the way through your foot if you absentmindedly step off a curb and fracture your ankle (not that I speak from experience). As such, anything besides the sample in the chamber, including gas, will inherently harm the image. Those of us who are lucky enough to be chemists and materials scientists don't often need to worry about this, as we mainly image very small rocks, which are typically very stable and natively have very high contrast, making *ex situ* imaging sufficient in most contexts. Unfortunately, however, some people happen to be biologists. Biological samples typically are not as easily imaged *ex situ* due to their high native water content as well as the thin, noncrystalline carbon-based cell membranes and structures that don't strongly scatter the beam, and as such, biological samples typically need to prepare their samples by first "fixing" them by treating them with chemicals that rigidify the structure, then dehydrating them, potentially embedding them in resin and slicing them thin, and then staining them with a heavy metal salt (often osmium or uranium) in order to increase contrast.[153] This process does work for imaging, and this is how probably

*Also sometimes referred to as EDX, EDXS, EDAX, XEDS, X-ray fluorescence (XRF), etc. It's hard to get scientists to agree on stuff, okay?

most biological TEM images are still made, but obviously all of this pre-processing causes chemical and physical changes to the sample that may inherently limit what can be claimed from TEM images. Furthermore, nearly all biological samples naturally exist in a hydrated state, so it is inherently limiting to only be able to view them as dehydrated structures. As such, though I take no joy in saying this, the biologists deserve significant credit for many of the advancements in *in situ* TEM.

The first major progress in this field was the development of cryo-TEM. The idea behind cryo-TEM is that, while liquid water would instantly boil off in the ultra-high vacuum and poison the column, solid ice, if kept properly frozen, will stay in that state.* Therefore, by quickly freezing aqueous samples in a very thin, vitreous (non-crystalline) layer, one can trap biological samples in their native state while minimizing the background from the water itself. This technique was first developed in the 1970s,[154] and has since been used to study not only (relatively) large cells and viruses but also individual proteins with near-atomic resolution. These developments in molecular biology won the 2017 Nobel Prize for Jacques Dubochet, Joachim Frank and Richard Henderson,[155] and it's easy to see why: previously the only way to structurally characterize proteins was through x-ray crystallography, and it is impossible to do x-ray crystallography on proteins in their native state. As such, cryo-TEM has become an indispensable technique among structural biologists. However, this technique is also worth consideration by chemists and materials scientists. While our samples tend to be more robust and we can typically achieve greater resolution *ex situ*, we want to understand not just our products, but also the intermediates, processes, and mechanisms that get us to our product, and by literally freezing the reaction as it is in progress, we may be able to see crystalline intermediates and metastable phases that we wouldn't normally be able to observe *ex situ*.

---

*This is the same principle that allows the gas giant planets to exist in our solar system. When the planets were forming, at a certain distance from the sun, water in the protoplanetary disc transitioned to a solid state, which is stable in the vacuum of space and was able to accrete into the cores of the much larger planets that we know and love today, whereas inside this "snow line" only rocks and metals could accrete into planets.[7]

This capability gets to the heart of this thesis: chemists tend to think about mechanisms in the context of forming molecules, and materials scientists tend to think of mechanisms in the context of forming solids. However, we know in reality that often both of these things are happening at the same time, and the ability to study intermediates in detail will give us far more insight into the detailed mechanisms by which syntheses occur.

Despite the huge impact that cryo-TEM has had in allowing us to view materials in their native state, it is still not quite a true *in situ* technique, since we still are viewing a snapshot in time and can't view active processes unfold. Furthermore, cryo-TEM is optimized for aqueous samples, for obvious reasons, but not all processes occur in water, especially in the chemical/materials space. While many other solvents can theoretically be frozen for cryo-TEM purposes, this is not always straightforward—cryo-TEM grids are typically frozen in liquid ethane to avoid the Leidenfrost effect that would be seen with liquid nitrogen, but many organic solvents are soluble in ethane, so this is not always a possibility. Even if they can be frozen, it needs to have a high enough melting point to not be immediately melted to a high degree by the high-energy electron beam, and even if it does meet that condition, organic species have a tendency to be carbonized by the beam and redeposited on the sample, severely limiting resolution.[156] These reasons and others motivate the study of true *in situ* TEM. *In situ* TEM can take place in the gas or liquid phase, and can use either specialized microscopes or specialized holders in order to study various processes. The most straightforward way to do this in the gas phase is to simply introduce a small amount of gas into the column. At low pressures, this will not significantly harm the image quality, and it can be used to very precisely control gas-mediated processes. This technique is called environmental TEM (ETEM), and has been used to very precisely observe crystal growth, for example in the earlier cited papers by Frances Ross, as shown in Figure 1.9. This technique is extremely

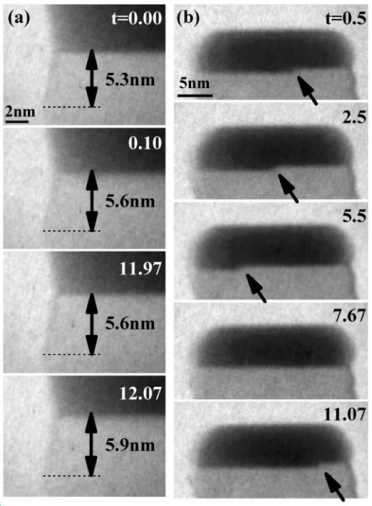

Figure 1.9: ETEM study of silicon nanowire growth showing defined step edges below the catalyst. Figure adapted from Ross, 2010[124]

useful to show crystal growth and other chemical processes in nearly the same detail as standard *ex situ* TEM and has really allowed us to observe crystal growth directly for the first time. I have yet to meet a TEM microscopist who has not spent considerable time watching these videos in awe. Unfortunately, the obvious limitation of this method is that it has to be a gas-mediated process. In real life, many processes are not gas-mediated. In order to appropriately understand the world, we can't limit ourselves to only studying the phenomena that are the easiest to study with current technology. And perhaps most pertinently to this work, most non-classical forms of crystal growth occur in solution and are solvent-mediated. This means that we need to find a way to look at things that happen in solution inside the TEM.

As previously discussed, everything that the electron beam passes through will scatter the electron beam to some extent. This means that any solvent will inherently reduce your image quality. Beyond that, the solvent obviously needs to be contained somehow, and whatever is used to contain the solvent will also inherently reduce the image quality. There is no way to prevent this. In theory, we can minimize this effect relatively straightforwardly—the particles we're looking at have to be very small anyway, so if we use a column of solvent that is only slightly wider than the particle size, and use an extremely thin membrane to contain the mixture on both sides, that will minimize the contribution to overall scattering from anything that isn't the sample. This is obviously harder to achieve in practice. Despite this, it has long been seen as a worthwhile goal. Owing perhaps to the obvious benefit of being able to observe biological materials in situ, the first *in situ* TEM experiments apparently happened remarkably soon after the development of the TEM, by Marton in 1934 or 1935.* Marton apparently sandwiched living cells in thin aluminum foil and was able to image them at high voltage. While I have not been able to locate these images to verify the magnification, knowing the amount of scattering that would be involved and

*I use the word "apparently" because, while I was able to locate many references to these experiments in later works by reputable authors,[157–159] I was not able to locate a copy of the original reference,[160] or any images that I could verify were from that original reference by Marton.

the power of TEMs at that time, it can be claimed with certainty that he would not have been able to image them at a higher resolution than what was easily achievable on optical microscopes at that time. It is likely for this reason that there was very little progress made in this field until 2003, when the first true liquid cell (LCTEM) holder was developed by someone whose name should be quite familiar at this point: the venerable Frances Ross. Her original sample holder sandwiched the sample between two silicon wafers that were coated on the sample side with 100 nm of silicon nitride, with the silicon selectively etched away to form a 100x100 μm window, with the chips separated by a silicon oxide spacer.[161] While these methods have been refined over the years, this is still essentially how LCTEM works: the sample in question is sealed between two silicon chips with (usually) silicon nitride windows, essentially creating a miniature cuvette in which to view the sample (Figure 1.10).

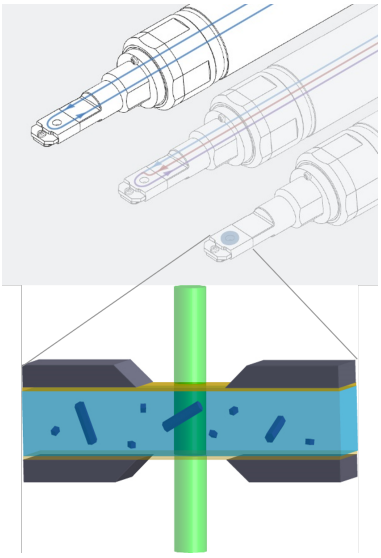

Figure 1.10: Schematic of a an LCTEM holder with detail showing the sample chamber. Images of holder from Hummingbird Scientific, inset original drawing.

These holders have now been engineered for many purposes and can be used for electrochemical biasing,[161] heating,[162] mixing,[163], and many other applications. Additionally, advancements in both holder engineering and TEM techniques have allowed for high resolution, atomic scale imaging that, importantly for our purposes, allowed for the first time the direct imaging of crystal growth by oriented attachment.[53] This is not to say that LCTEM doesn't have its challenges and limitations: aside from the aforementioned inherent scattering and the obvious size limitations, there are also challenges with quantifying, predicting, and rationalizing the effects of beam interactions with the sample and the solvent, as well as the dimensional limitations of only allowing interactions perpendicular to the beam. Even so it is no exaggeration to say that LCTEM has revolutionized the study of nonclassical crystal growth and brought it from a theoretical phenomenon to something that is directly observable.

The dimensional limitations that LCTEM suffer from are also to some extent fundamental

to all direct TEM imaging, and really any transmission imaging at all. When we image things with our eyes, we are actually measuring light that has been scattered off a surface (for the most part). Because of that, we can easily intuit the shapes and arrangements of items based on how the light scatters and how certain objects obscure other objects. The corollary to this in electron microscopy is the scanning electron microscope (SEM): the SEM measures electrons that have scattered off the surface of a material,* and as a result, SEM images have a very lifelike, photographic, three-dimensional quality to them. This likely explains why SEM images are so popular among the general public—they are easy and intuitive to interpret because they look like normal photographs of macro-scale objects. TEM, however, is a transmission technique, meaning that, rather than measuring backscattered electrons, it measures the electrons that have transmitted, or passed through the material. In this sense it can most intuitively be compared in the macroscopic scale to medical X-ray imaging. This means that, unlike SEM, TEM can give information about internal structures that would otherwise be hidden by the surface, but the drawback is that, because the radiation source passes through the entirety of the material (or body part) before it is detected, we only observe a two-dimensional projection of the object being imaged, as seen in Figure 1.11.† In the case of TEM, this projection is usually sufficient. Most TEM samples tend to be relatively homoge-

Figure 1.11: Example of a medical x-ray image of a fractured ankle. Note the apparent flattening of the image and the impossibility of determining whether the image was taken from the front or the back due to the two-dimensional projection effect of transmission imaging. Ankle is the author's own.

*More accurately, it can measure either primary electrons from the beam that have been backscattered or secondary electrons from the sample that have been ejected from the surface, but the result appears similar in either case.

†Let it be known that the author of this dissertation fractured his ankle specifically so that the concept of transmission imaging could be better illustrated in this dissertation.

neous and of a known (or not particularly interesting) shape. But sometimes it is important to understand where certain features are relative to each other on the particles being imaged, and in that sense, two-dimensional projections will lie to you. In this sense, the X-ray analogy is particularly apt, as the solution to the problem is exactly the same for both techniques. In medical imaging, if you need three-dimensional detail in your X-rays, you perform a computed (axial) tomography scan (CT/CAT scan). The way this works is straightforward: the region of interest is placed inside a tubular device and X-rays are taken at a bunch of different angles, allowing many different views of the object, and observing how features appear to move relative to each other will provide information on their three-dimensional structure. How these images are mathematically stitched together is less intuitive. Luckily, the method for doing so was described by Johann Radon* in 1917.[164] While the detailed mathematics of the Radon transform are beyond the scope of this dissertation, qualitatively, the projection at each tilt is integrated and stitched together into what is referred to as a sinogram, and then the sinogram can be "untwisted" to produce a three-dimensional model. There are a number of ways to do this in practice, and the mathematics of all of them are rather dizzying, and in fact people have written entire dissertations on this topic alone,[165] but luckily these methods are by now well-described and can be performed with several existing software packages at the click of a button.[166,167] The Radon transform is extremely versatile and as such, tomography can be a useful technique to understand the internal structures of objects at all scales, from just a few unit cells of crystals[168] to micron-sized objects[169] to, of course, the human body, all the way to entire oceans,[170] planets,[171†] and even galaxies and greater.[172] As cool as it would be to map out entire galaxies, here we focus on that which can be achieved in the TEM, and unfortunately there are not any known galaxies at this time that will fit inside a TEM.[173] TEM tomography operates in much the same way as a medical CT scan, except insofar as

---

*Of no relation to the radioactive noble gas

†Seismic tomography, as it's known, is able to reconstruct Earth's internal structures by measuring seismic data from earthquakes from multiple points on the Earth's surface, and is in my opinion one of the most clever scientific techniques I've ever encountered.

that the sample is tilted rather than the radiation source.* Samples that are mounted on wires (or are themselves wires) can be mounted in a specialized holder that can be rotated a full 180 degrees. This gives the Radon transform the best chance of creating a faithful reconstruction because the algorithm doesn't need to "guess" what the sample looks like over any large interval of angles. This technique is difficult for most samples however, as only one sample can be loaded into the TEM at the time (as opposed to grids that can hold several liftouts or thousands of particles), not to mention the practical limitation that it requires a specialized holder that costs many thousands of dollars and can't really be used for anything else.

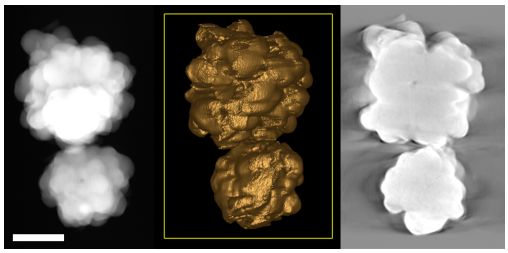

Figure 1.12: STEM Tomography of α-NaYF. From left, the raw STEM image of the particles, the reconstructed isosurface, and a reconstructed tomographic slice through the center showing a low-density feature near the center of the upper particle. Scale bar = 200 nm. Original work.

As such, for most samples it is more practical to tilt 120-140 degrees, which is achievable for most samples in a fairly standard low-profile holder, and allow the Radon transform to approximate the rest. Using this technique, we can not only determine the size and shape of particles in three dimensions, but we can also observe internal structures that are largely obscured in the raw images, as seen in Figure 1.12. This can be useful in understanding heterogeneous structures as well as in gaining a truer sense of the three-dimensional shape and size of the particles. With a combination of skill, very powerful microscopes, and favorable samples, using techniques pioneered by Jianwei Miao and Peter Ercius, people have even been able to build TEM tomographic reconstructions with atomic precision, potentially revealing the locations of individual crystalline defects.[168,174–177]

*This is really a deficiency of CT; it's much simpler to keep the radiation source fixed than the sample, but unfortunately medical "samples" have an annoying tendency to complain about being spun around in a tube, so they have to spend big money on a movable X-ray source. This is one of many reasons why microscopists make bad physicians.

1.3.2 Atom Probe Tomography

It is easy to understand why one might want to study the three-dimensional structure of materials with atomic or near-atomic precision. Being able to see these details can give us unprecedented detail into how local defects and structures affect the chemistry and physics of a material. TEM is without question the easiest way to achieve this level of detail in two dimensions, and it is easy to tilt samples, making it tempting to jump immediately to TEM tomography. However, atomic electron tomography is not always practical. The Radon transform assumes monotonic contrast, so the phase contrast in TEM mode that dominates at high resolution is not compatible with the technique. Therefore at this scale only STEM tomography will reconstruct correctly. Taking potentially hundreds of STEM images of the same particle can induce considerable beam damage and/or contamination, both of which threaten the ability of the tilt series to reconstruct correctly. And more fundamentally, the inverse Radon transform, as applied in the real world, inherently makes assumptions and introduces artifacts that may be difficult to reconcile. Additionally, while EDS and EELS tomography do exist,[178] even at the atomic scale,[179] doing this for every tilt, including off axis tilts, is prohibitively difficult in almost every case, making it effectively impossible to collect significant chemical information about each reconstructed atom. As such, we see that while atomic electron tomography is a powerful technique, it lacks the versatility to be the sole technique for studying materials in three dimensions at this scale. With these limitations, it is worth considering a completely different method of collecting these data.[180]

While TEM is the workhorse technique for imaging atomic and near-atomic detail in nanoscale samples, it is not the only technique capable of that. In fact, as I briefly foreshadowed at the beginning of Section 1.3 in Figure 1.5, the first ever atomic resolution images were in fact collected not with TEM but with field ion microscopy (FIM). FIM is a remarkably elegant technique in which a sample is milled to a fine tip and a strong enough voltage is applied to the sample to field evaporate ions from the tip. The shape of the tip itself creates a point projection effect, naturally magnifying the ions, which can then be imaged with,

originally, a fluorescent screen.[181] Assuming the material is well-ordered and oriented on axis, this allows individual columns of atoms to be detected directly. While this is a very elegant method, it is very rare to see it used directly anymore. The reason for this is largely because it was realized in 1967 by Müller (who you may remember from Figure 1.5) and Panitz that, given that the FIM is projecting ions from the sample, those ions should be measurable with a mass spectrometer (MS), thus providing information about the identity of the ions in addition to their physical location.[182] At this time, MS detectors did not have spatial resolution, so Müller and Panitz built a FIM screen with a hole in it that was connected to a time of flight (TOF) MS detector. The image on the screen could then be positioned such that the ions in a particular region of interest would pass into the MS detector, thus allowing it to probe the atomic composition at that location in the sample, and was therefore termed the "atom probe." Eventually, two-dimensional MS detectors were developed and integrated by Blavette et al. in 1993, allowing for the collection of data in three dimensions—the two spatial dimensions of the MS detector as well as time, which corresponds to the z dimension of the sample.[183] This technique was often called 3D Atom Probe (3DAP) in its early years, but is now referred to as atom probe tomography (APT).*

Originally, APT (and, in fact, all FIM-derived technology) was a rather specialized technique that could only be used for conductive samples. This is due to the fact that it relies on controlled field evaporation of the sample. This was induced by a large applied electric field that is pulsed such that field evaporation occurs at known, discrete moments, which are set as t = 0 for the TOF spectrometer. For conductive samples, this is a very effective and robust method, because the induced charge readily redistributes to the surface and concentrates at the

*Some may argue that 3DAP is actually a more technically accurate term, as the typical definition of tomography, as discussed in Section 1.3.1, is the mathematical reconstruction of two-dimensional data taken from various angles into a three-dimensional model using the Radon transform. APT instead measures the three dimensional data by sequentially and destructively measuring xy "slices" along the z axis, more akin to an archaeological dig than a CT scan, thus using the term "tomography" loosely to just refer to any 3D reconstruction. However, APT is the common term in use today and is therefore the term that I use here.

tip, thus allowing it to field evaporate in an orderly manner. Non-conductive materials, however, will store charge, which exerts a mechanical force on the tip, often causing it to literally explode (Figure 1.13).[184] While it is theoretically possible to collect data on nonconductive or poorly conductive samples this way, it typically takes several hours or days to lift out, mount, sharpen, load, and position a single APT tip, so the return on investment is sufficiently low that it's usually not worth it to attempt. But as chemists, we want to learn about our samples, and therefore we have to take them as they come. Yet we would like to be able to collect APT data. While an induced electric field is inherent to all FIM derivatives, we can at least reduce the applied voltage and eliminate the voltage pulsing that leads to mechanical fracture.

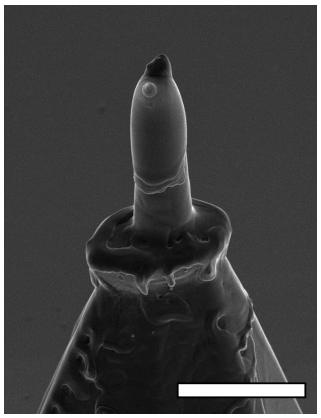

Figure 1.13: SEM image of an APT tip of (formerly) diamond that fractured after building up charge, destroying the silicon mount as well. Scale bar = 20 µm. Original work (unfortunately).

While field evaporation is required for APT, there is not a requirement that the evaporation be entirely induced by the applied field. Thus, we can hold the applied voltage at a level that is somewhat below that which is required for field evaporation, and then we can use a pulsed laser to thermally excite the tip above the point of evaporation.[185] This is is a robust and useful method, and has allowed for countless studies of nonconducting and poorly-conducting materials.[186] It does, however, add in some additional considerations when collecting APT data. Very generally, higher laser pulse energies allow lower voltages to be used, which reduces the mechanical strain on the sample. It can also lead to overheating of the sample or runaway heating, which can cause thermal tailing on the mass spectrum* and can also lead to weakening or melting of the sample itself.[187] Additionally, different laser pulse energies can cause different components of the sample to evaporate at different rates, making it important to optimize the laser pulse energy for each new material studied.[188] Even though there are many considerations that make APT

*Thermal tails arise from the sample remaining above the temperature required for field evaporation for a finite amount of time. Because the laser pulse sets the start time for the TOF detector, any ions that leave the sample after the pulse are measured as a longer-than-true time of flight.

a complicated technique, in practice is it is a very versatile and often surprisingly user-friendly technique that allows us to understand the very local chemistry of materials, especially when complemented with other methods such as TEM.

1.4 Summary

Here we have looked at how crystals have classically been thought to grow as well as a more modern understanding of the many ways that that process can happen in reality, we have looked into the particular material that we have used to study these processes, and we discussed some of the techniques that we've used to study them. These are concepts that recur in some way or another in each of the following chapters, and hopefully this introduction makes clear what the overarching goals were of our research and why we made some of the experimental decisions that we did. While each chapter can stand alone as an individual manuscript, the goal of this dissertation as a whole is to show the rigorous study of crystal growth processes in NaYF from both a physical and a chemical point of view, and to make the case that both of those points of view are required in order to be able to fully understand this system. As I wrote in the beginning of this chapter, there is no reason to expect that this type of behavior is unique to NaYF. We just happened to find it there. Our initial goal in studying NaYF in this way was to improve its capability for laser cooling. But one could imagine that for other systems (or even the same system) this could matter, for example, for the engineering of battery electrodes,[189] drug development,[190] and simply for the fundamental understanding of chemical reactions,[191] just to name a few. If a solid is being produced, we should understand how that happens both chemically and physically, because ultimately, those are two sides of the same coin, and to overlook one is to misrepresent the other.

Chapter 2

MECHANISTIC STUDY OF THE HYDROTHERMAL NAYF PHASE TRANSITION

We begin our study of NaYF by taking an in-depth look into the two common crystalline phases: cubic, and hexagonal. In the hydrothermal synthesis that we have typically used to produce NaYF, we can observe both phases depending on the temperature that we heat the reactor to. At lower temperatures, we observe a pure cubic phase, and at higher temperatures, we observe a nearly pure hexagonal phase. However, we can also produce the cubic phase by heating to high temperatures for a short time. This suggests that the cubic phase always forms first and then converts to the hexagonal phase. This chapter discusses that phase conversion and the mechanism that underlies it. We find that the conversion is driven by a non-classical mechanism that occurs via the formation and oriented attachment of mesocrystals, which could have implications in the engineering of atomically-precise materials, among other applications. These results were published in Chemistry of Materials in 2020, and the following text and figures are largely reproduced with permission from that publication.[1]

2.1 Introduction

Lanthanide-doped rare-earth fluoride crystals are a class of materials that have attracted great interest for decades due to their optical upconversion properties.[192–195] This has led to a wide range of applications in biomedicine[195–198], solar energy[199–202], anti-counterfeiting[83,203,204], solid-state laser refrigeration[86,87,114,205], and more recently, claims of enhanced night vision in living rodents via upconversion of infrared wavelengths into the visible region.[84] Lanthanide ions doped within fluoride crystals are also under active investigation for applications such as long-lived optical quantum memories[206]. One important example of these materials is

sodium yttrium fluoride (NaYF), which has been studied not only for its optical and electronic properties,[207–210] but also for its morphological and crystallographic microstructure[93,195,211]. Traditionally, bulk single crystals of NaYF have been grown using high-temperature Czochralski or Bridgman methods[93,212,213], but this method has shown difficulties in obtaining single crystals of the hexagonal phase due to large anisotropic thermal expansion coefficients[92].

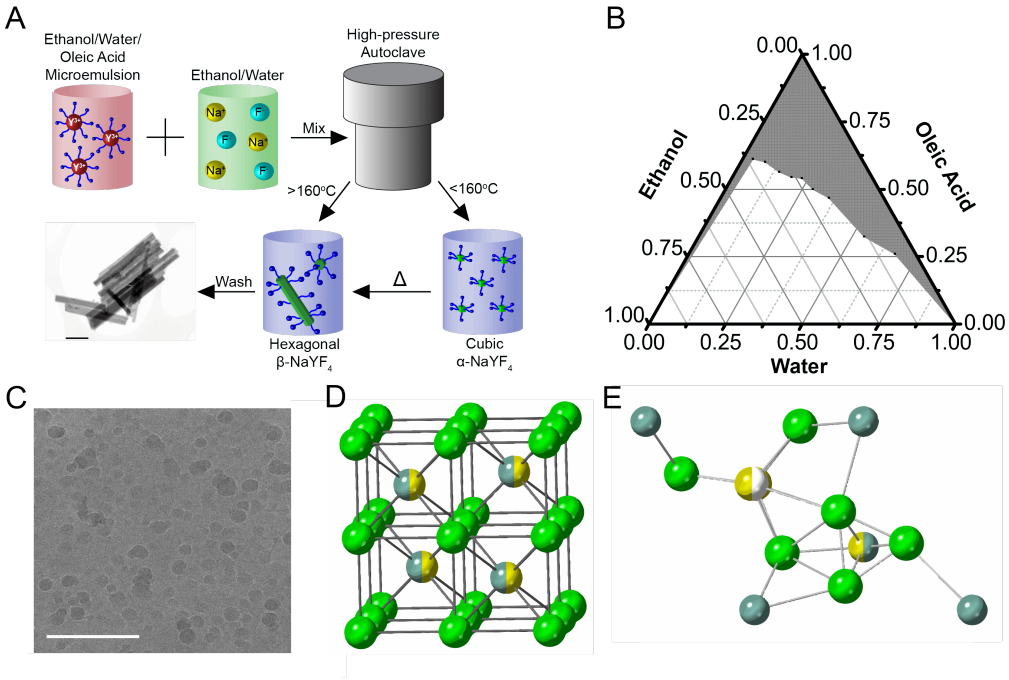

Figure 2.1: (A) Hydrothermal synthesis of NaYF (scale bar on STEM image = 500 nm) and (B) ternary phase diagram for water/ethanol/oleic acid microemulsion. Shaded region is microemulsion and unshaded region is heterogeneous mixture. (C) Cryo-TEM of mixture frozen in liquid ethane seconds after mixing showing microemulsion at 77 K. Scale bar = 200 nm. (D) Cubic and (E) Hexagonal crystal structures for NaYF, yellow = Na, blue = Y,Yb, green = F, white = vacancy. Half-shaded atoms indicate split occupancy.

In contrast to Czochralski or Bridgman single crystal growth, hydrothermal syntheses allow for safer, lower-cost, and more controlled growth of single-crystalline nanostructures[101,102,214,215]. Furthermore, the use of water as the major solvent naturally allows for greater control and limitation over the incorporation of organic species than other solvothermal methods. This is of particular importance for applications involving laser refrigeration,

where organic impurities often cause heating.[216] Hydrothermal methods also do not require an inert atmosphere or harsh solvents, making them more approachable, scalable, and green than thermolytic and nonaqueous solvothermal methods.[104] Finally, hydrothermal methods typically produce much larger β-NaYF particles than thermolytic and solvothermal methods.[101] However, while the hydrothermal process shown in Figure 2.1A allows for an easily-controllable, safe, and green synthesis of either cubic (α) nanoparticles or hexagonal (β) nanowires, hydrothermal processes by their nature, take place at elevated temperatures and pressures inside a sealed vessel, making it challenging to probe the chemical and physical phenomena that govern the nucleation and growth within.[217,218] The thermodynamics underlying the synthesis and growth of NaYF and similar species has been the subject of some research,[219–221] indicating that the alpha phase nucleates first based on both volumetric and surface contributions to the overall free energy. Above a critical grain size, however, the hexagonal phase becomes more thermodynamically stable.[222] With this in mind, classical thermodynamic calculations by definition are independent of the kinetic and mechanistic phenomena that exist under particular synthetic conditions. For example, theoretical modeling of the solvation and diffusion of sodium (Na^+) ions in water is still a subject under active investigation.[223] Furthermore, the solvation and subsequent diffusion of ions in solution is complicated by a further in ternary microemulsion systems (Figure 2.1) This system is thought to work by creating segregated microenvironments, which makes these reactions difficult to model.[163] Moreover, because the α phase is more thermodynamically stable at small grain sizes, the cubic phase appears first during crystallization, raising fundamental questions about how the formation of the hexagonal β-NaYF nanowires follows the initial formation of the cubic phase, and how specifically that phase conversion occurs.

One difficulty in characterizing this phase conversion mechanism is that there are discrepancies in the literature regarding the exact crystal structure of the hexagonal phase.[97,224–230] While it is clear that the crystal structure of β-NaYF is hexagonal in nature, the occupancy of the cation sites and the level of delocalization is a matter of discussion. For example, Grzechnik showed in 2002 that the exact crystal phase changes as a function of pressure[97],

but molecular dynamics calculations by Szefczyk in 2014 showed that it is theoretically possible for any of the three most widely reported crystal structures to exist at atmospheric conditions.[224] It should be noted that, to our knowledge, all single crystal XRD studies of β-NaYF reported to date have been made with Czochralski-grown materials,[230] which cannot be assumed to undergo the same growth mechanisms as hydrothermal β-NaYF. For this reason, the crystallographic microstructure between the two may not be identical between crystals grown by these two methods.

The cubic crystal structure is well-characterized as a solid solution of tetrahedrally-arranged sodium and rare earth cations with an opposing tetrahedron of vacancies in a cubic lattice of fluoride ions, analogous to the well-known fluorite crystal structure (Figure 2.1D).[94,227] Notably, the sodium and rare earth ions are arranged randomly on the cation sites, meaning that a phase transition to one of the known reported β-NaYF structures would involve the reordering of trivalent cations due to the change in coordination number. This reordering is straightforward to consider in a Czochralski process, where the NaYF is grown directly from the liquid phase and therefore eliminates the phase conversion entirely or in a classical process like the ones observed in some solvothermal NaYF syntheses,[231] where the α particles dissolve fully into solution. However, it is more difficult to contemplate in a system that undergoes non-classical crystal growth such as oriented attachment (OA)[232]. Nonetheless, in light of recent results on a number of synthetic systems that yield nanowires of a bulk phase starting from primary particles of a transient nanoscopic phase via OA[233,234], this mechanism of β-NaYF nanorod formation must be considered.

During OA, crystal growth mostly proceeds by assembly of primary particles that typically attach on lattice-matched faces, for example by crystallographic alignment on a twin plane[46,49,53,235–237], to form the final bulk crystal. This mechanism contrasts with classical growth processes that proceed through ion-by-ion addition to atomic steps on the crystal surface.[49] While the primary particles are typically of the same phase as the secondary particles, oriented attachment can also occur in systems where primary particles of a different phase either transform before attaching,[234] attach on faces of the secondary particle that

nonetheless produce a lattice match[233], or attach to form a disordered aggregate that evolves to a single crystal over time[238,239]. The latter of these modes of OA often involves the formation of mesocrystals, which are ordered superstructures of small crystals, with the individual particles typically separated by surface ligands.[240]. These mesocrystals are by their nature a kinetic product, in which the thermodynamic product would be a single crystal.[57]. The energy barrier, typically, is the (often considerable) energy required to remove the surface ligands.[241] Once these surface ligands are removed, the crystallites are already oriented crystallographically with respect to each other, and therefore can rapidly and easily undergo oriented attachment.[242] Because oriented mesocrystalline intermediates can be structured in complex ways, they are often found in nature, where single crystals of complex morphologies can be desirable,[243–245] notably in sea urchin spines.[246,247] However, crystal growth involving mesocrystalline intermediates is also an important process in synthetic chemistry.[47,234,248,249]

In this work, we present a multifaceted approach to understand the fundamental growth mechanism of β-NaYF nanowires under hydrothermal conditions. Firstly, we present a "time series" approach in which we study the properties of NaYF particles synthesized in reactions that were quenched before the β-NaYF could fully form, using TEM and XRD to study the evolution of their physical and chemical properties. We then transition to a "post-growth" approach in which we study the properties of fully-formed β-NaYF and α-NaYF nanostructures using *in situ* and *ex situ* TEM, Energy Dispersive X-ray Spectroscopy (EDS), Electron Energy Loss Spectroscopy (EELS), atom probe tomograpy (APT), and EXAFS to examine the particles for chemical insights into how they form.

2.2 Results and discussion

To understand the phase conversion mechanism, we first attempted to deepen our understanding of the final β-NaYF product to examine for any clues as to how they formed. To begin this investigation, we examined the crystal structure of the hexagonal β-NaYF using extended X-ray absorption fine structure (EXAFS) spectroscopy to study the ytterbium centers in doped β-NaYF (Figure 2.2). EXAFS spectra were fit to a known $P\bar{6}$ crystal structure for

β-NaYF,[97] modified for compatibility with FEFF, as discussed previously. These data were then processed and fit with a variety of models to determine the spacing and occupancy of the ytterbium ions. The $P\bar{6}$ unit cell for β-NaYF has a stoichiometry of $Na_{1.5}Y_{1.5}F_6$, with one Y^{3+} ion (Y1) residing on the corner and the remaining half-ion (Y2) in an internal split-occupancy site with sodium (Figure 2.1E). Ytterbium replaces these yttrium ions in the doped structure, so EXAFS models were fit with Yb^{3+} in both of those sites. Surprisingly, in contrast with bulk Bridgman single crystals,[230] the fit only improved in quality when the only substitution was in the Y1 site, which would seem to be consistent with the Yb only doping into the Y1 site and not the split occupancy Y2 site. Further experiments are needed to determine definitively whether the Y2 site is truly undoped in hydrothermal NaYF. The EXAFS data fit well with our substituted $P\bar{6}$ model, except that most distances are shorter, which can be explained by the smaller ionic radius of Yb^{3+} as compared to Y^{3+}. Further insights into the synthesis mechanism and the resulting crystal structure can be gathered by considering how lanthanide dopants incorporate into the crystal matrix.[250,251] This is useful not only for our own mechanistic studies, but also for myriad other studies involving the upconversion properties of lanthanide-doped NaYF.[98,114,252]. Specifically, the dopant can be uniformly distributed, or it might undergo some sort of clustering, which could result in fluorescence quenching.[253–255] To determine whether the Yb dopant clusters, a model was fit with some of the nearest Y1 sites replaced with Yb^{3+}. This decreased the quality of the fit, suggesting that the nearest rare earth neighbors to ytterbium in this structure are yttrium ions, and therefore that the ytterbium dopant does not cluster.

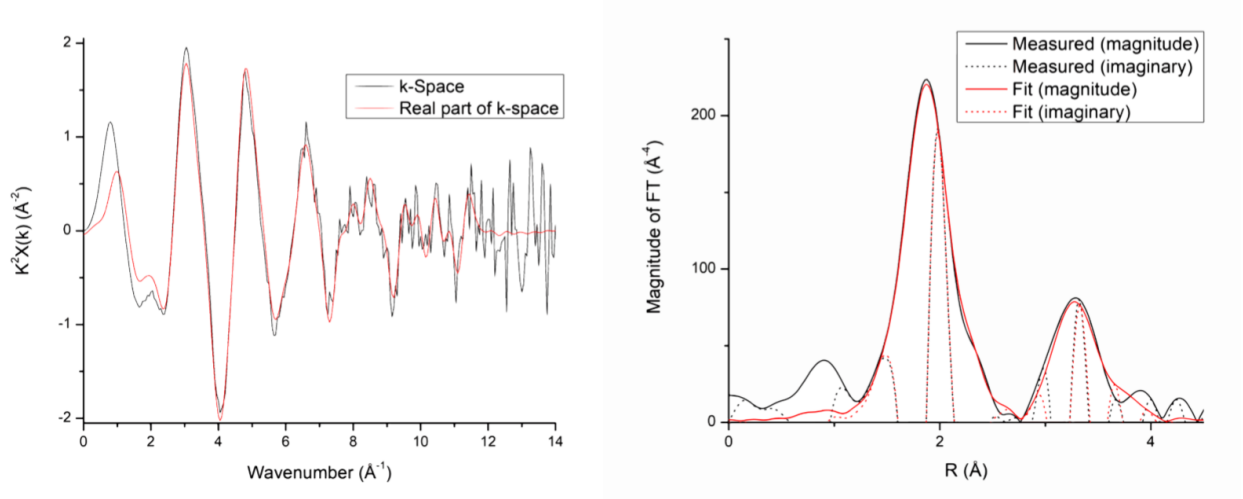

Figure 2.2: EXAFS analysis of β-NaYF:10%Yb nanowires. (A) EXAFS data in k space. (B) Fourier transformed Yb spacing data and calculated best fit. Data collected by Xuezhe Zhou and Matthew Marcus.

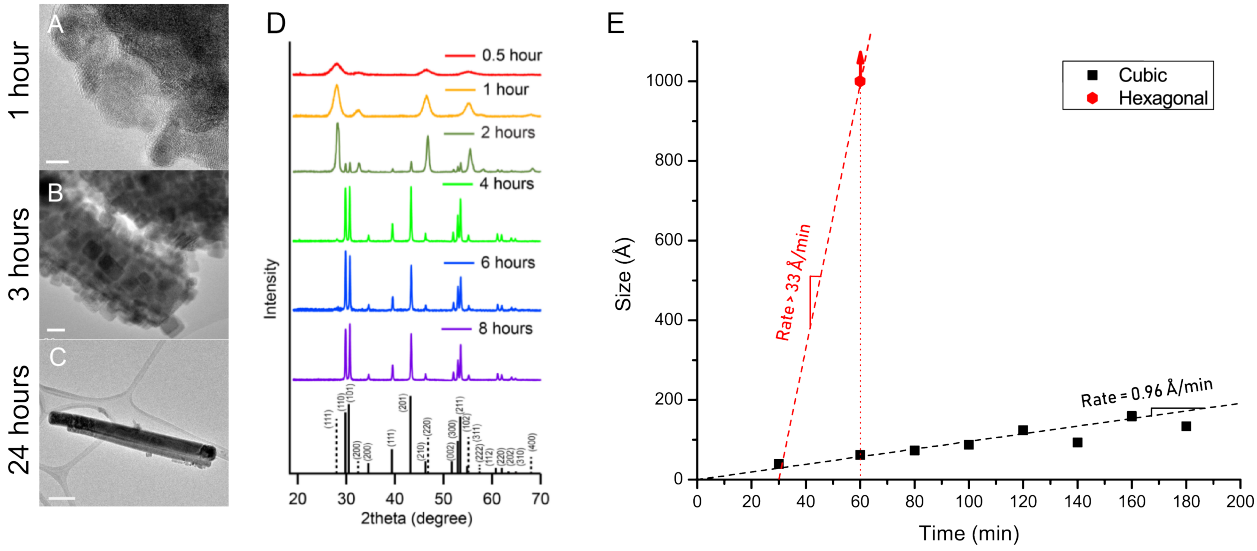

Figure 2.3: (A-C) TEM images of the progression of NaYF growth at (a) one hour, (b) three hours, and (c) 24 hours. Scale bar A = 5 nm, B = 50 nm, C = 200 nm. (D) Powder XRD study of NaYF growth at selected time points. Dashed black lines represent the theoretical α-NaYF peaks and solid black lines represent the theoretical β-NaYF peaks. (E) Scherrer analysis of XRD spectra. β-NaYF is first observed at the one hour time point at a size that is already too large to measure with a Scherrer analysis. This indicates a growth rate for α-NaYF of approximately 0.96 Å/min, or 0.176 unit cells per minute, and a minimum initial effective growth rate of at least 33 Å/min, or 5.6 unit cells per minute for β-NaYF.

To begin studying the phase conversion mechanism directly, we started with a hydrothermal time series approach. By varying the time of synthesis, T_s, from 30 minutes to eight hours, we show using TEM and XRD (Figure 2.3) that the cubic α phase nucleates within 30 minutes, while the hexagonal β phase is first detectable by high-dose XRD after approximately one hour. After four hours in the oven, the β phase is the only phase detectable by XRD (Figure 2.3D), though it should be noted that a small amount of α-NaYF still remains after even 24 hours, as shown in subsequent TEM data. A Scherrer analysis of these XRD spectra (Figure 2.3E) shows that the β-NaYF nucleates with a diameter much larger than that which the α-NaYF ever achieves, showing a minimum effective growth rate over that time period (33 Å/s) that is more than 30 times faster faster than that of the α-NaYF (0.96 Å/s). It should be emphasized that the maximum size measurable with a Scherrer analysis is generally on the order of 100 nanometers, depending on the precision of the spectrometer and the number of reflections measured,[256,257] and as such, we cannot use this method to determine that the β-particles nucleate at any specific size greater than 100 nm, but rather that they are first observed much larger than the α-NaYF particles, and that the α-NaYF particles continue to grow even after the β-NaYF particles have already formed. This is consistent with the hypothesis that the hexagonal (β) phase nanowires are not nucleating by a classical crystal growth mechanism, in which they would grow steadily as the feedstock dissolves.[258–260] The fact that the Scherrer analysis unambiguously shows that the α-NaYF particles continue to grow with time rather than dissolve supports the argument that the phase conversion mechanism itself is non-classical regardless of the eventual growth mechanism of the β-NaYF. The growth rate of α-NaYF does eventually appear to slow, as TEM images (such as the one shown in Figure 2.5) indicate that the particle diameters at 24 hours are still 40-50 nm, rather than the approximately 160 nm we would expect from a consistent growth rate, which we attribute to a decrease in the supersaturation as the reaction proceeds. It should also be acknowledged that, if after three hours the volume fraction of α-NaYF becomes undetectable by XRD, then small β-NaYF grains would likely also have too small a volume fraction to be visible in XRD, particularly given its peaks' superimposition over much sharper peaks of

large β-NaYF grains. However, the lack of any TEM observation of small β-NaYF at any time point stands in stark contrast to the observation of plentiful α-NaYF after the XRD sensitivity limit is met, and this crucial difference reinforces our data suggesting that the β particles do not nucleate and grow classically from solution.

The non-classical crystal growth hypothesis is supported further by experiments in which α-NaYF nanocrystals were nucleated both with and without lanthanide dopant ions, where the doped samples contained 20% Yb and 2% Er. The doped and undoped α-NaYF samples were mixed together and heated in order to form doped β-NaYF nanowires. If the doped α-NaYF nanocrysytals dissolved and precipitated β-NaYF nanowires through a classical mechanism, then we would expect the distribution of dopant lanthanide ions in the β-NaYF nanowires to be homogeneous. If the β-NaYF nanowires were formed through oriented attachment, then we would expect the lanthanide dopant distribution to be heterogeneous. A STEM-EDS analysis of the resulting nanowires (Figure S1 in Appendix B) shows that the ytterbium concentration is not homogeneous across the material, suggesting that they are not growing classically from a homogeneous solution based on the dissolution of α-NaYF grains. We hope to use advanced techniques in future work to determine the exact nature of the boundaries between the doped and undoped regions of these particles.

These observations are corroborated by TEM images (Figure 2.3A-C) which show β particles first appearing orders of magnitude larger than the α particles. A further analysis of TEM images from the 3 hour time point shows that the β-NaYF particles appear to form from clusters of α-NaYF that are roughly 200 nm in size at the three hour time point (Figure 2.4, also see Figures S6 and S7). We also directly observed clustering of α particles in water with *in situ* TEM (Figure S8 in Appendix B). At first glance, one may only recognize these clusters as random, if relatively monodisperse, agglomerations of α-NaYF particles, but a closer examination reveals that the particles in the clusters have crystallographic order and physical faceting, appearing to form mesocrystals.

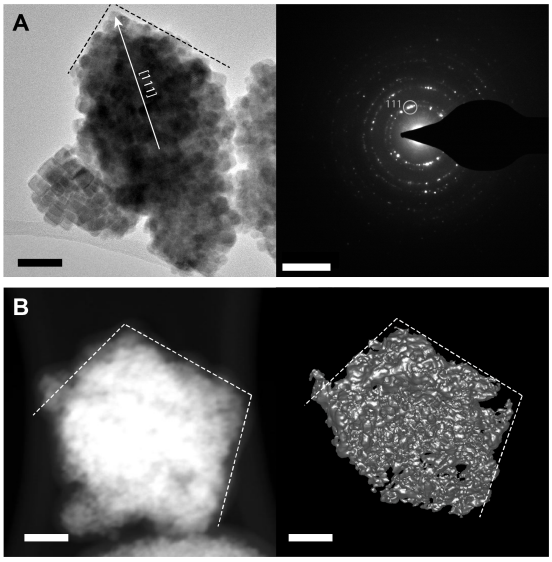

Figure 2.4: NaYF mesocrystals forming after a three hour synthesis. (A) Anisotropic cluster of α-NaYF and SAED showing a [111] axis parallel to the elongation axis of the particle, with [111] vector and emphasis of faceting shown on TEM. The approximate zone axis of the mesocrystal is [011]. Scale = 50 nm for TEM and 5 nm^{-1} for the SAED. (B) STEM HAADF of another mesocrystal and tomographic reconstruction showing faceting. Scale = 100 nm.

Figure 2.4 shows an anisotropic, faceted cluster of α-NaYF, with a diffraction pattern that clearly shows that the particles in the cluster preferentially align with a [111] axis parallel to the direction in which the cluster is elongated. It should be emphasized that this cluster contains only α-NaYF and no detectable β-NaYF. However, other clusters from the same time point (such as several shown in Appendix B) appear to surround large β-NaYF rods, suggesting that the nucleation of β-NaYF happens within these clusters. This observation is also consistent with the TEM data in Figure 2.3, where the only β-NaYF we observe is over an order of magnitude larger than the α-NaYF and furthermore that we observe no α-NaYF particles larger than approximately 50 nm in diameter, but that we do observe these mesocrystals forming with diameters of roughly 200 nm. These observations suggest a plausible mechanism in which α-NaYF mesocrystals undergo an oriented attachment process to form large particles that rapidly convert to β-NaYF due to thermodynamic driving forces, and then afterwards proceed to grow classically. The energy barrier initially preventing the oriented attachment of the mesocrystals most likely is the energy required to remove the oleic acid from the surface of the α particles. Presumably the magnitude of this energy barrier would be vastly different in the two phases of the microemulsion system, which may shed light onto further details of the conversion mechanism. A detailed study of these kinetics remains a subject for future investigation.

Even after a 24-hour synthesis, small ($\sim$ 30 nm), morphologically cubic particles remain on the surface of the nanowires, as can be seen in the STEM tomographic reconstruction in Figure

2.5A and in the TEM image in Figure 2.5C, though it should be noted that their overall mass fraction becomes too low for them to be observed with XRD after approximately three hours. By measuring the d-spacing from the HRTEM image (Figure 2.5E) as 2.71 Å and comparing the projection and FFT to simulated crystal axes of possible species in the synthesis vessel, the image in Figure 2.5E was indexed to the [100] projection of α-NaYF (Figure S2 in Appendix B). This demonstrates that α particles can not only survive the high temperature synthesis conditions but that they continue to grow and form morphological structures even in the immediate presence of β particles. TEM images of particles at short synthesis times serve to illustrate a non-classical growth mechanism, as shown in Figure 2.5B, after a 160 minute synthesis, as compared to the 24 hour synthesis in Figures 2.5C-E. Here, moiré fringes can easily be seen in the HRTEM image, which suggests minor deviations from perfect crystallographic alignment.[261] The Fast Fourier Transform (FFT) of the crystal matrix, which is related to a diffraction pattern and shows the degree of single crystallinity through the spreading (or lack thereof) of the spots,[262] also illustrates the partial alignment of crystallites in the particle. Taken as a whole, considering the moiré fringes, the FFT, and the crystal lattice, we can see that the particle in Figure 2.5B seems to be comprised of several smaller, partially-aligned crystallites. While it should be acknowledged that conclusions should not be drawn from individual images in isolation, this observation is consistent with, and serves to illustrate, the rest of our data

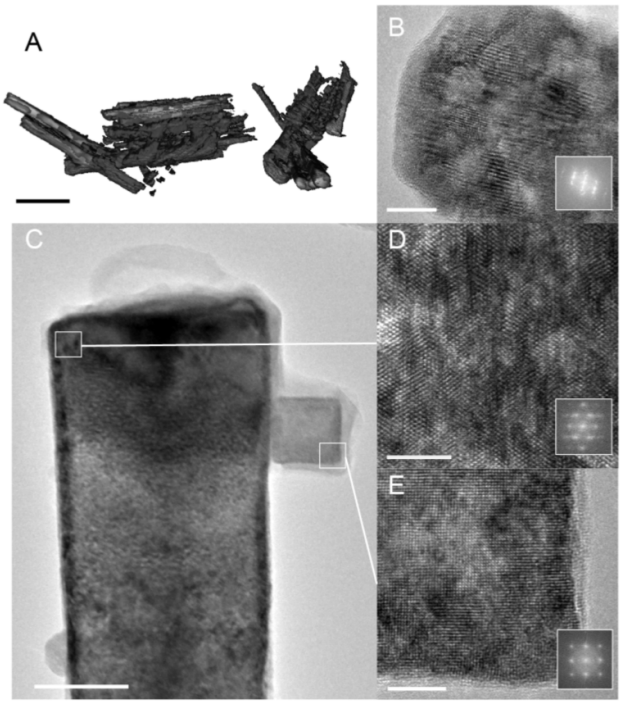

Figure 2.5: (A) Tomographic reconstructions of clustered β-NaYF particles with α-NaYF particles on the surface. Scale = 500 nm. (B) TEM image and FFT of a β-NaYF particle after a 160 minute synthesis, noting the slight crystallographic mismatch evident in the lattice. Scale = 10 nm. (C) TEM image of a β-$NaYF_4$ particle (left) with an α-NaYF particle on the surface (right). Scale = 50 nm. (D,E) HRTEM images of β- and α-$NaYF_4$ particles, respectively. Scale = 5 nm.

suggesting that the β-NaYF is formed by a mechanism that involves oriented attachment of mesocrystals.[263]

An amorphous coating appears to be present on the end cap of the β-NaYF rod and on all surfaces of the α-NaYF cube (Figure 2.5B). EDS mapping data is consistent with the presence of oleate, as discussed further below. Density functional theory calculations by Sui et al.[264] suggest that oleate can influence the growth of NaYF in complex ways, which leads us to hypothesize that the presence of sodium oleate on the end caps influences the classical growth of the β-NaYF after the phase conversion. The presence of sodium oleate in those end caps is suggested by EELS and EDS maps of the sodium content of the nanowires (Figure 2.6). The EDS map in Figure 2.6F indicates an enrichment in sodium on the caps, and the EELS map in Figure 2.6B shows clearly that the sodium is aggregating on the caps rather than the sides of the wires, as well as uniformly around α-NaYF particles. The apparent lack of sodium within the nanowires in the EELS map can be attributed to multiple scattering as a result of the large diameter of the nanowires.[265] The superposition of the sodium and the fluorine EELS maps (Figure 2.6D) shows that the sodium is present in regions of amorphous material outside of the nanowire, and preferentially on the tips, rather than it accumulating within the structure. This behavior indicates that there is sodium in that amorphous material, which is consistent with our hypothesis that that material is sodium oleate. This finding is further supported by a mass spectrum of the surface, measured with atom probe tomography (APT, Figure S3 in Appendix B), which shows several organic groups and sodium, but no yttrium, indicating that we are only measuring the material on the end cap. The fact that we observe this enhancement of oleate on a particular face leads us to hypothesize that it is relevant to the growth mechanics of the crystal, and the specific nature of this influence remains a subject for potential future work.

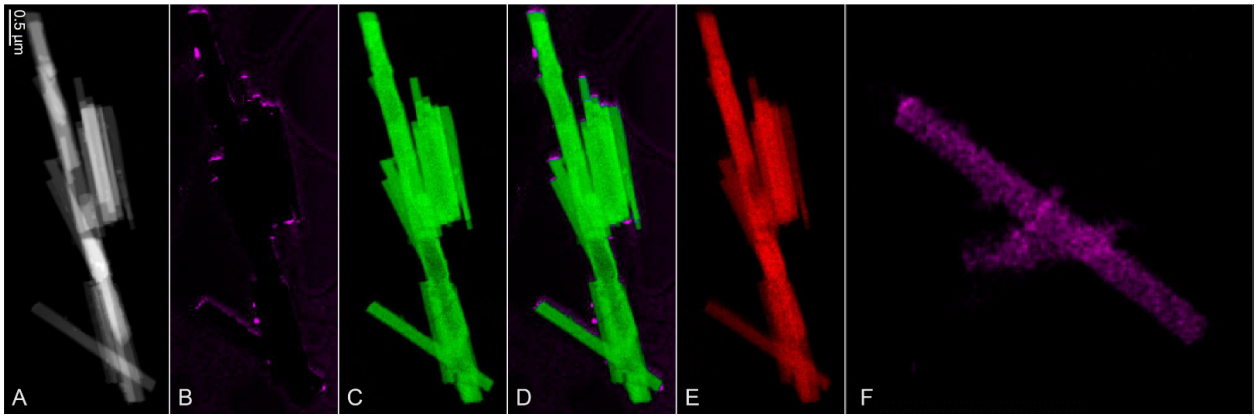

Figure 2.6: (A) STEM HAADF image of $NaYF_4$ cluster (scale = 500 nm). (B-E) EELS maps of (B) Na-K edge, (C) F-K edge, (D) Na + F, (E) Y-L edge. (F) EDS map of Na-K edge (on a different cluster of NaYF at the same magnification). Data collected by Steven Spurgeon.

Dynamic light scattering (DLS) measurements (Table S4) show a significant change in zeta potential during the phase conversion. The α-phase is observed to have a highly negative zeta potential in water (-70mV), while the final β-phase has a positive zeta potential in water (+20mV). Although the zeta potentials reported here likely differ from those within the hydrothermal microemulsion, along with an intrinsic complexity due to the random orientation of non-spherical particles[266], it is possible that the kinetics of oriented assembly of the α-phase could be significantly altered as the magnitude of the zeta potential becomes less negative during the transition to the β-phase. The different zeta potentials may also explain the TEM observation of cubic α-phase grains attached to the surface of β-phase nanowires.

2.3 Conclusions

In this work, we present several data sets consistent with the hypothesis that hexagonal NaYF nanowires synthesized by a hydrothermal method do not form through classical crystal growth mechanisms but rather through a non-classical mechanism involving oriented attachment of mesocrystalline intermediates. The oriented attachment component of this mechanism suggests that this hydrothermal synthesis could be used to build nanoparticles from multiple components, which could be employed in nanoscale devices with novel optoelectronic

properties. EXAFS measurements suggest that the Yb^{3+} ions in doped NaYF are evenly distributed across the crystal lattice rather than clustering, and that the Yb doping is possibly site-specific in the β-NaYF structure. This finding motivates future work using low-temperature spectroscopy to further investigate the exact nature of the doping and how it relates to the synthetic method of the particles.[267] Furthermore, a thorough understanding of the synthesis mechanism based on particle interactions can inform future experiments meant to direct the morphology of β-NaYF particles, and could even help to design a predictive model to control the morphology and size of NaYF materials.

2.4 Materials and Methods

Hydrothermal Synthesis of $NaYF_4$

2 mL of a 2.875 M aqueous NaOH solution were added to 8 mL of 100% ethanol. 3 mL of oleic acid were then added to the mixture while stirring. 1 mL of a 1 M aqueous $RECl_3$ stock solution (RE = 90% Y, 10% Yb or 100% Y) was then added to the mixture (Solution A) and it was stirred for 30 minutes. Meanwhile, 4 mmol of NaF were dispersed in 3 mL of water and 3 mL of ethanol (Solution B). Solution B was added to Solution A dropwise while stirring. After 30 minutes of stirring, the mixture was transferred into a PTFE-lined stainless steel autoclave (Parr 4747, 25 mL) and sealed. The autoclave was placed in a 200°C oven in the case of β-NaYF, or 100°C in the case of α-NaYF, for a specified amount of time, T_s, and then allowed to return to room temperature. The product was washed and centrifuged with both ethanol and water. T_s is 24 hours for the full synthesis of either α- or β-NaYF, and it was varied from 30 minutes to 8 hours for the time series.

TEM Measurements

TEM images were taken on an FEI G^2 TECNAI F20 S/TEM at 200 kV with a Gatan Ultrascan CCD camera. For *in situ* measurements, an α-NaYF sample was dispersed in water and dropcast into a Hummingbird static liquid cell TEM holder and imaged through silicon

nitride windows. Tomographic reconstructions were compiled using publicly available Matlab code[166] or FEI Inspect3D software, and were visualized using Matlab or IMOD[167]. TEM and STEM samples were prepared by dropcasting particles sonicated in a dilute suspension onto a lacey carbon grid. High-angle annular dark field (STEM-HAADF) images were collected on a JEOL GrandARM-300F microscope operating at 300 kV, with a convergence semi-angle of 29.7 mrad and an inner collection angle of 75 mrad. Energy-dispersive X-ray spectroscopy (STEM-EDS) maps were collected using a dual JEOL Centurio detector setup (∼1.6 sr solid angle), with a 1 Å probe size, roughly 237 pA probe current, 10 μs px^{-1} dwell time, and a roughly 3.5 min total acquisition time. Electron energy loss spectroscopy (STEM-EELS) maps were collected using the same probe settings and a spectrometer acceptance angle of roughly 113 mrad, with a 1 eV ch^{-1} energy dispersion, 10 ms px^{-1} dwell time, and 6 min 18 s total acquisition time. The spectrometer was fully binned in the non-dispersive axis to improve signal-to-noise. No plural scattering correction was performed and no principal component analysis (PCA) or other denoising was applied.

Cryo-TEM Measurements

A small volume (3.5 μL) was taken directly from a stirred vessel containing the NaYF reaction mixture at room temperature just after mixing. This was applied to a glow-discharged C-flat holey carbon EM grid (Protochips), blotted, and plunge-frozen in liquid ethane with an FEI Vitrobot plunge-freezing device. The grid was stored under liquid nitrogen until imaging, which was done using an FEI TECNAI G^2 Spirit operating at 120 kV and liquid nitrogen temperature, and a Gatan Ultrascan 2000 CCD. Automated data collection was accomplished via the Leginon software package.[268]

EXAFS Measurements

Samples for EXAFS were prepared by dropcasting a suspension of β-NaYF in water onto an X-ray transparent polyimide (Kapton) tape substrate. The sample was placed in the LBNL ALS Beamline 10.3.2 under a helium environment. Hard X-rays were focused on the

sample around the Yb L3-edge, from 8.8-9.9 keV. Two scans were taken in QXAS (continuous-scan) mode, with count time/point increasing roughly linearly in the post-edge region from 4 to 11 seconds. Data were taken in fluorescence and transmission mode simultaneously. The two fluorescence scans were pre-edge subtracted, post-edge normalized, corrected for overabsorption, then averaged.

EXAFS Analysis

Our model was fit based on the $P\bar{6}$ structure of β-NaYF as reported by Grzechcnik[97]. This model has a unit cell stoichiometry of $Na_{1.5}Y_{1.5}F_6$ with two Y sites, one of which (Y2) is half-occupied and shared with a half-occupied Na site (Na1) at the same position. There is another Na site (Na2), which is half-occupied. We made the assumption that all Yb dopants would substitute in a Y site. Because split occupancy crystal structures are incompatible with the use of FEFF[269] and Artemis[270], we modified the unit cell such that it contained two of the original $P\bar{6}$ unit cells with full occupancy of Y and Na, respectively. For further details on this modification, see Appendix B. Shell-by-shell fitting was performed using Artemis running FEFF6l. These fits were done in q-space with a distance range of 1-4.5 Å, a k-weight exponent of 3, and a q range of 2-14 $Å^{-1}$.

DLS Measurements

Dynamic light scattering (DLS) measurements were taken on a Malvern ZEN3600 Zetasizer™ Nano-ZS with a 633 nm red laser. $NaYF_4$ samples were centrifuged and rinsed 3 times with Millipore water, and resuspended in Millipore water before final DLS measurements. Particle size measurements were taken in 1 cm polystyrene cuvettes, and zeta potential measurements were taken in Malvern disposable folded capillary cells.

XRD Measurements

Powder X-Ray Diffraction (XRD) samples were prepared by dropcasting a concentrated slurry of sample onto ⟨100⟩ silicon wafers. Spectra were taken on a Bruker D8 Discover Microfocus diffractometer with a Dectris Pilatus3 R 100K-A 2D detector and a Cu Kα X-ray source with a 0.5 mm collimator. A Coupled $2\theta/\theta$ scan was performed from 16° to 93° with a 5.5° increment to create overlap, with a scan time of 30 seconds per θ. During the scans, the sample was oscillated in the x, y, and ϕ directions to remove the effects of texture and improve statistics. An air scatter screen was used to reduce background. Scans were integrated, indexed, processed, and analyzed using Bruker Diffrac.Eva software. The growth rate for α-NaYF was measured using a linear regression set to an intercept of zero using OriginPro 8, using a lattice constant of 5.4700Å. The minimum effective growth rate for β-NaYF was measured with the assumption that the particles were larger than the maximum particle size measurable by a Scherrer analysis on this instrument of roughly 100 nm, and with the zero point set to the last measurement in which no β-NaYF was observed. The lattice constant used for β-NaYF was 5.9148Å.

APT Measurements

Atom probe tomography (APT) samples were prepared from β-NaYF nanorods using a FEI Helios Nanolab DualBeam scanning electron microscope/focused ion beam. APT was performed using a Cameca LEAP 4000X-HR housed at the Environmental Molecular Sciences Laboratory at the Pacific Northwest National Laboratory. The detected ion count rate was set to 300 ions per second using a 355 nm UV laser pulsed at 100 kHz. The specimen stage temperature was 44K. The data were processed using IVAS software version 3.8.

Chapter 3

STUDY OF THE NUCLEATION OF NAYF IN WATER

In Chapter 2, we looked at the phase transition of NaYF from cubic to hexagonal during the hydrothermal synthesis. This synthesis took place in a rather complicated microemulsion solvent system. This likely helped to limit particle size, however it also obfuscated the nucleation process due to the variety of dynamic microenvironments within the solvent. In order to understand the initial nucleation of cubic NaYF, we settled on studying a simpler system: NaF and YX_3 in water. While we can't guarantee that this proceeds in exactly the same way as the more complicated nucleation in the microemulsion system, it does allow us to observe the process in much more detail, which in turn allowed us to reconsider the entire concept of cubic NaYF and where it fits in with related compounds.

In this chapter, we discuss the initial separation of a YF_3-like phase from solution immediately after mixing via a liquid-liquid phase separation that is then followed by the solid state diffusion-assisted nucleation of cubic NaYF from the dense liquid phase. This is similar to previously-reported two-step nucleation mechanisms, however the compositional change adds a layer of complexity and emphasizes the interconnectedness of the chemical reaction with the crystal growth process. We also show with computational modeling that this compositional change is a necessary precursor to nucleation, as the cubic phase of YF_3 that has been reported in the literature is not a stable compound and it requires some amount of stabilization from monovalent cations in order to nucleate. This predicates the importance of our final NaYF study in Chapter 4 considering the overall relationship between NaYF and YF_3.

3.1 Introduction

Classical nucleation theory (CNT), first described by Gibbs over 140 years ago, has been a robust model for describing the formation of crystals from homogeneous solution.[271] However, despite its simplicity and general validity for many crystallization processes, some proceed via so-called "nonclassical" mechanisms.[40,272] These mechanisms include, but are not limited to, the formation of amorphous or poorly-crystalline species and the oriented aggregation and attachment of individual building blocks.[272] Broadly speaking, nonclassical crystallization is a realization of Ostwald's step rule, which suggests that systems will not necessarily take the most direct route to their most stable phase, but rather that they tend to go through a series of intermediates that are closer in free energy to the initial state.[21,273]

One such nonclassical crystallization mechanism is two-step nucleation via a dense liquid phase (DLP), typically formed through spinodal decomposition (SD).[274,275] In this mechanism, the highly supersaturated initial phase spontaneously separates free of a thermodynamic energy barrier[275] into ion-rich and ion-poor liquid phases, and crystals then nucleate from the ion-rich phase, often via an amorphous intermediate.[276] This mechanism has been observed directly via liquid cell transmission electron microscopy (TEM) of gold nucleation from solution[276] as well as in electrochemical reactions in nanoparticles,[277] in molecular dynamics (MD)[278] and kinetic studies of calcium carbonate,[279] in bulk chemical studies of $MgSO_4$ at high temperature,[71] by optical microscopy in crystallizable polymer solutions,[280] in MD simulations of highly supersaturated NaCl solutions,[38] and in optical microscopy and light scattering studies of protein solutions.[274] Some systems have also shown a distinct intermediate step in which the DLP condenses into an amorphous phase prior to crystallization.[281] These studies, among others, suggest that the two-step mechanism via a DLP can readily be accessed in a wide range of solution-based systems, because, when taken to sufficiently high supersaturation, nearly all solutions will reach their limit of stability.[282]

One aspect of these two-step pathways via a DLP that remains largely unexplored is that the stoichiometry of the intermediate phase is variable and ill-defined and it must evolve over

the course of the reaction in order to generate the final stable phase. This is because the compositions of the ion-rich and ion-poor liquids are defined by a phase line that spans a range of compositions rather than by a set of line compounds. Therefore, for crystallization to proceed, ions must be rejected from or drawn into the solidifying regions of the ion-rich liquid. This adds a level of complexity to other previously investigated nonclassical systems, in which the intermediate phases are all line compounds, which can either be identical for each phase, for example, as in the case of $CaCO_3$ (ignoring waters of hydration), or they can be distinct and require chemical transformation, as documented for the calcium phosphate system.[283] For the latter, charged calcium triphosphate species undergo aggregation accompanied by Ca^{2+} binding and deprotonation to create the amorphous phase, and then undergo a second step of Ca^{2+} binding and deprotonation to create the first crystalline phase. In a DLP-mediated pathway, on the other hand, ions may exchange more dynamically rather than via specific transformations to these discrete line compounds. The added complexity in these two-step pathways is further emphasized when the final compound has a ternary or more complex stoichiometry, which increases the difficulty of the required ionic reorganization. Given the common occurrence of the formation of DLPs in highly supersaturated solutions and the preponderance of ternary and more complex compounds in natural and synthetic systems, the further study of the chemical evolution of intermediate phases in these systems is therefore necessary.

Here we investigate this multi-step crystal growth pathway using a model system based on ternary sodium-yttrium-fluoride (NaYF) materials. This is an ideal system for exploring the role of chemical evolution during crystallization because the stoichiometry of NaYF materials has been shown[95] to change based on a combination of NaF and YF_3 that varies continuously with a final stoichiometry in the cubic phase of $Na_{0.5-x}Y_{0.5+x}F_{2+2x}$, or (0.5-x)NaF • (0.5+x)YF_3, with $0<x<0.5$. As x approaches zero, the stoichiometry approaches $NaYF_4$, which is used frequently as shorthand for this material. Due to the importance of the variable stoichiometry of this system to our paper, we instead use the shorthand NaYF when referring to this material as-synthesized, reserving the $NaYF_4$ notation for the hypothetical perfectly

stoichiometric structure. The majority of aqueous syntheses of NaYF use either microemulsion solvent systems[1] or organic capping ligands[284] for the purpose of controlling both the size and shape of discrete nanocrystals[285]. In contrast, we here synthesized ligand-free NaYF materials to provide a clear understanding of the role of solvated aqueous ion dynamics by eliminating the effects of ion chelation and surface passivation by organic species. Our results demonstrate the formation of a previously uncharacterized DLP in the NaYF system as would be expected in a typical two- or three-step mechanism, but also incorporating a distinct additional step of solid-state diffusion which determines the final stoichiometry of the material. This change in stoichiometry has not previously been studied in systems that proceed by spinodal decomposition. Further investigation of this mechanism may facilitate new designs for many functional materials using multi-step nucleation and growth with nonstoichiometry in the design of materials for a diverse range of applications including solid-state laser refrigeration,[114], optical thermometry[286], nanoscale lasing[287], night vision[288], and electrochemical energy storage.[289]

3.2 Results and Discussion

In order to probe the nucleation and growth of NaYF materials in the absence of organic species we first prepared aqueous electrolyte solutions of both NaF and YCl_3, and then combined them at standard conditions with relative concentrations stoichiometric to $NaYF_4$ (Figure 3.1A). Immediately upon mixing the starting solutions, we observed the apparent formation of a gel-like material (Figure 3.1B), which can be filtered to a translucent solid. This gel is temporarily stable over the course of hours, but eventually condenses into a nanocrystalline white powder over the course of hours (Figure S1 in Appendix C). TEM imaging of the gel shows an interconnected, porous structure (Figure 3.1C). Scanning TEM (STEM) tomography (Figures3.1D-F) reveals not only the interconnected three-dimensional morphology (Figure 3.1F) but also the open-cell structure that can't be seen in conventional STEM (Figure 3.1E). Brunauer-Emmett-Teller (BET) surface area measurements show a surface area of the gel phase on the order of 100 m^2/g, consistent with an open-cell gel

morphology, and powder X-ray diffraction (XRD) data show very broad peaks consistent with α-NaYF or a similar cubic material (Figure S2 in Appendix C). Assuming the initial separation from solution occurs via spinodal decomposition, we can estimate the time of separation using the Cahn-Morral equation, which is a multicomponent analogue to the Cahn-Hilliard equation describing spinodal phase separation.[275,290] By modifying a previously-reported model to solve the Cahn-Morral equation for a simplified version of the NaYF system,[291] we were able to estimate that the initial separation should be largely complete within 250 μs (Figure 3.1G-I). We caluclated the potentials of mean force for interactions between two YF_3 molecules or a YF_3 molecule and a YF_4 ion in vacuum (figure S3 in Appendix C), which indicate that the dense liquid phase is likely able to form due to attractive interactions, and that spinodal decomposition is therefore a plausible explanation for the initial separation of the fluoride phase from solution. To the best of our knowledge there has been one previous passive observation of interconnected particle morphology during the aqueous synthesis of NaYF materials.[292] However, to date there has been neither discussion of the unusual multi-step gel formation mechanism nor detailed nanostructural characterization of the recovered gel material reported in the literature.

While the XRD data were consistent with nanocrystalline α-NaYF (Figure S2 in Appendix C), the peaks were not sufficiently resolved to be able to definitively conclude that the gel is purely α-NaYF, and TEM data suggest that there are some amorphous, poorly crystalline, or otherwise disordered regions (Figure 3.2C). Furthermore, the observation of significant beam-induced crystallization in the TEM (Figure S4 in Appendix C) is consistent with the possibility that some of the crystalline regions observed in high resolution TEM (HRTEM) were likely amorphous in the as-synthesized material, meaning that TEM measurements would underestimate the distribution of amorphous and poorly crystalline regions. Using STEM-EDS, we observe that the composition varies smoothly between Na-rich and Na-poor regions (Figure 3.2D), showing a negative correlation of the net counts of Na and F relative to Y and Yb, suggesting composition that varies along the YF_3−$NaYF_4$ spectrum.

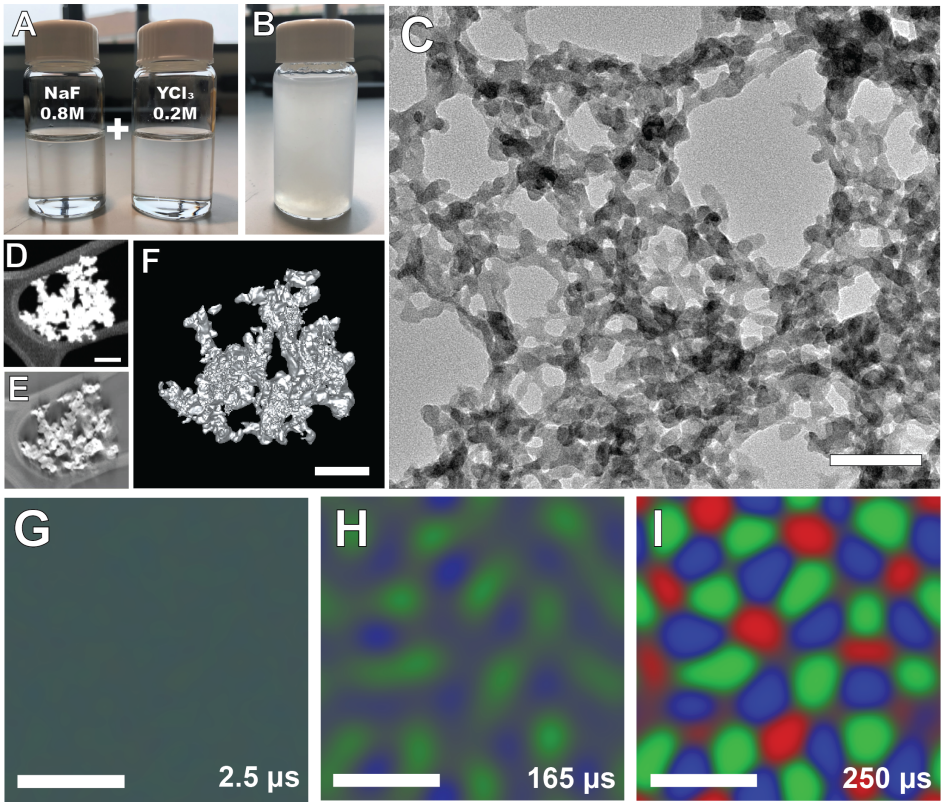

Figure 3.1: Synthesis of NaYF gel. (A) Starting solutions of 0.8M NaF and 0.2M YCl_3 combine to form (B) a gel, which shows (C) an interconnected structure in bright field TEM. Scale bar = 50 nm (D) STEM HAADF of a small piece of gel. Scale bar = 100 nm (E) Reconstructed tomographic slice through roughly the middle of the same particle showing interconnected, porous internal structure. (F) Reconstructed tomographic isosurface model of the same particle in D and E showing three-dimensional physical structure. Scale bar = 100 nm. (G-I) Cahn-Morral modeling of the phase separation shows the mixture separating fully from homogeneous solution in roughly 250 μs. Modeling performed by Lucien Brush.

EDS spectra extracted along the path of the line scan confirm the presence of a measurable sodium peak above the noise (Figure S5 in Appendix C). It should be noted that the thermodynamically stable orthorhombic structure of YF_3 was not observed in the gel with x-ray or electron diffraction, indicating that the cubic system is what initially crystallizes. Considering the crystal structures of the two cubic phases (NaYF and YF_3), it is notable that they share a nearly identical lattice of fluoride ions. This similarity in crystal structure allows for local variations in stoichiometry without significantly affecting stability within reason, consistent with much of the literature regarding cubic $NaF{\cdot}YF_3$ structures grown

from melt, which suggest that the bulk material can be thought of as a solid solution of NaF and YF_3.[93,95] However, to our knowledge, this has not been thoroughly characterized on the nanoscale. Based on these findings, we hypothesize that the gel initially forms via a dense liquid phase that condenses to an amorphous solid with a composition resembling YF_3, while the excess NaF in solution slowly incorporates into the matrix to seed and stabilize cubic crystals of NaYF with initially variable composition.

To investigate the gradual transition in stoichiometry from a sodium-poor to a sodium-rich phase, we attempted a cation substitution experiment on the gel using potassium. By removing the gel from its native solution as shown previously, it is possible to temporarily suspend the process of NaF incorporation. After submerging the recovered NaYF gel in a concentrated (1M) KF solution, we observed that the remaining sodium-poor regions incorporated KF to form KY_3F_{10} (KYF) (Figure 3.3A), which was distinguishable in XRD after the gel is allowed to fully collapse into single crystals (Figure 3.3B). While KYF can form in multiple stoichiometries and structures, the cubic KY_3F_{10} phase likely forms in this case because it is isostructural with the cubic YF_3 and $NaYF_4$ structures.[293] We quantified this process by incubating the gel in its native solution for a set period of time (t_{inc}) before filtering and transferring it to the KF solution for long enough for it to fully crystallize (typically overnight). We could then observe how much sodium had incorporated into the gel at t_{inc} and how much sodium-poor amorphous material remained, with the amorphous sodium-poor fraction subsequently incorporating the free K^+ from the solution, and which we would later measure as a KYF peak in the XRD. As t_{inc} increases from 15 minutes to two hours, we observe that the proportion of the sodium phase increases linearly and is accompanied by a corresponding linear decrease in the relative amount of material that incorporates potassium (Figure 3.3C). This shows that the incorporation of sodium into the gel occurs as the result of solid-state diffusion and is thus unambiguously a separate step from the initial formation of the yttrium-rich gel phase.

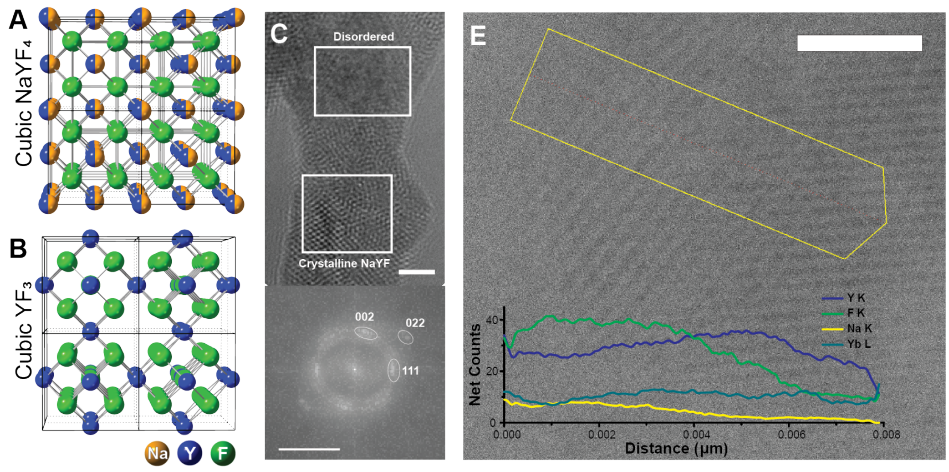

Figure 3.2: Microstructural characterization of the gel. (A-B) Crystal structures of (A) cubic (α) NaYF and (B) cubic YF_3. Yellow = Na, blue = Y, green = F. Each structure shows 2x2 unit cells (C) Bright field HRTEM of the gel showing both ordered and disordered regions, with an FFT of the labeled ordered region showing it to be consistent with cubic NAYF preferentially aligned along the [110] zone axis, with slight misalignment. Scale bar = 5 nm for the TEM and 5 nm^{-1} for the FFT. (D) STEM image of the NaYF gel with EDS plotted along the yellow arrow, integrated across the width of the arrow, showing a transition from a sodium-rich region to a sodium-poor region, showing a correlation between the Na and F counts relative to Y and Yb. Scale bar = 1.5 nm. Spectra can be found in figure S5 in Appendix C.

To characterize the local chemical environment of the ions without inducing crystallinity as we did with the TEM studies, we used solid-state ^{19}F nuclear magnetic resonance spectroscopy (SSNMR) to characterize the gel product compared to its eventual fully crystallized α-NaYF product (Figure 3.4A) as well as orthorhombic YF_3 (Figure 3.4B). We used orthorhombic YF_3 rather than the previously discussed cubic phase because the cubic phase, with one possible exception,[294] has not been isolated without considerable incorporation of the countercation from the fluoride precursor,[295,296], a challenge which we will address computationally later in this manuscript. As shown in ^{19}F spin-echo magic angle spinning (MAS) NMR (Figure 3.4C) the gel exhibits a broad resonance centered at -61 ppm with a peak width of 30 ppm. As reported by Bessada, et al.,[297] the ^{19}F chemical shift is highly sensitive to its coordination environment in molten fluoride mixtures, displaying a nonlinear and monotonic increase from -225 ppm to -28 ppm by increasing the concentration of YF_3 from 0 to 100% in the NaF-YF_3 mixture. Compared to orthorhombic YF_3, characterized by a relatively sharper peak at -58

ppm with a width of 12 ppm, and α-NaYF, which has a similarly broad resonance at -77 ppm with a width of 28 ppm, these data are again consistent with a gel that consists of some regions that are more similar to YF_3 and others that are closer to $NaYF_4$. Because the broadness of the NaYF ^{19}F spectrum can be attributed to a large distribution of isotropic chemical shifts due to the random arrangement of Na^+ and Y^{3+} around F^-,[227,298] we show that the ^{19}F rotor-synchronized Hahn-echo spectra (Figure 3.4D) reduce the signals from faster-relaxing components and thereby allow for finer resolution of the remaining signal. The respective deconvolution of the resonances reveals that the gel does have some components similar to those in α-NaYF and YF_3 (-81 ppm and -69 ppm, respectively). However, the main peaks in the region that is expected to indicate YF_3 are not consistent with the major peak of orthorhombic YF_3 at -58 ppm, due to the variation in the coordination geometries of bridging fluoride ions between the cubic and orthorhombic polymorphs of YF_3 as well as amorphous regions. This result emphasizes that the YF_3 product in the gel is not the

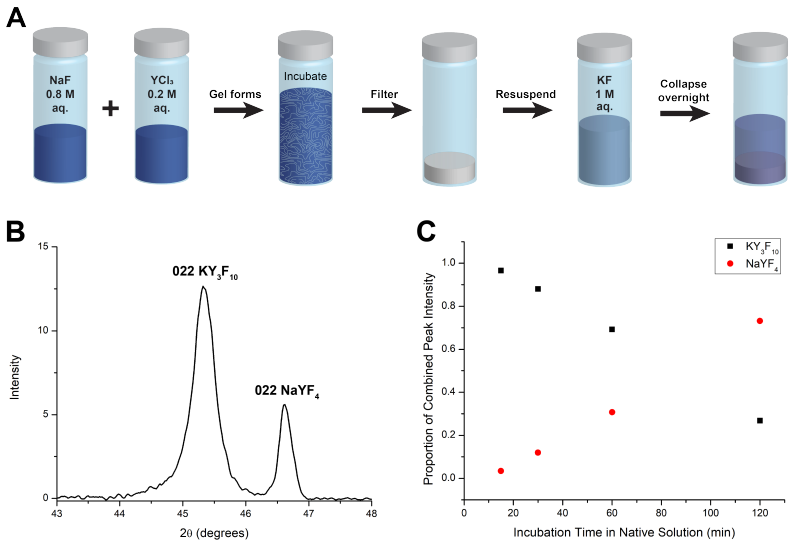

Figure 3.3: Ion replacement experiment. (A) Schematic for the cation replacement experiment (B) Representative XRD at t_{inc} = 60 minutes zoomed in to show 022 peaks (C) Peak height of the 022 peaks corresponding to either KY_3F_{10} or $NaYF_4$ normalized to the sum of the 022 peak heights for both phases as a function of t_{inc}. This plot shows clearly that the longer the gel is allowed to develop in its native solution prior to filtration, the more sodium is retained by the final product, and the less potassium is incorporated.

orthorhombic phase but rather amorphous YF_3 and sodium-poor cubic NaYF. Furthermore, Figure 3.4E shows that the ^{19}F spin-lattice relaxation time constant T_1 drops significantly from 19 s for α-NaYF and 9.2 s for orthorhombic YF_3 to 3.2 s for the gel, which indicates that the major fluoride species are more mobile and less ordered in the gel phase. This is consistent with our observation that there are significant amorphous, poorly crystalline, and disordered regions in the gel and also emphasizes the propensity for this gel (but not the final NaYF crystals) to undergo solid-state diffusion, as we have observed, which may facilitate potential applications in electrochemical energy storage as discussed in more detail below. Single-pulse ^{23}Na NMR spectra of the gel and the α-NaYF samples, respectively (Figure S6 in Appendix C), both contain major resonances centered at -18 ppm and -9.5 ppm, which were assigned respectively to Na^+ sites in the bulk nanoparticles, and to Na^+ sites at the surface or near defects, as originally reported by de Queiroz, et al.[298] The fraction of the -9.5 ppm peak changes from 35% in α-NaYF to 75% in the gel sample, suggesting that the gel has over twice as many surface or defective Na^+ sites as compared to the final crystalline product.

Thus far, we have shown that this reaction proceeds via a two-step crystallization mechanism and furthermore in our ion replacement experiment that sodium incorporates into the matrix relatively slowly after the gel has formed. However, these results do not address when or how that sodium incorporation occurs, except that it is after the liquid-liquid phase separation. Specifically, the sodium ions could incorporate into the dense liquid or amorphous solid phase before it crystallizes, or the gel could form a cubic YF_3 intermediate that then accepts sodium and fluoride ions (or sodium fluoride molecules) into gaps in the crystal structure. To answer this question, we turned to atomistic modeling methods. The first question to consider is whether it is even reasonable to expect a cubic YF_3 phase to form in the first place. While there are some reports of cubic YF_3 in the literature,[294,299–301] some of those have since been disproven[295] and others may have other complicating factors such as the incorporation of additional ions. We used molecular dynamics simulations to model both cubic YF_3 (Figure 3.5A) and cubic $NaYF_4$ (Figure 3.5B). After allowing the lattice to

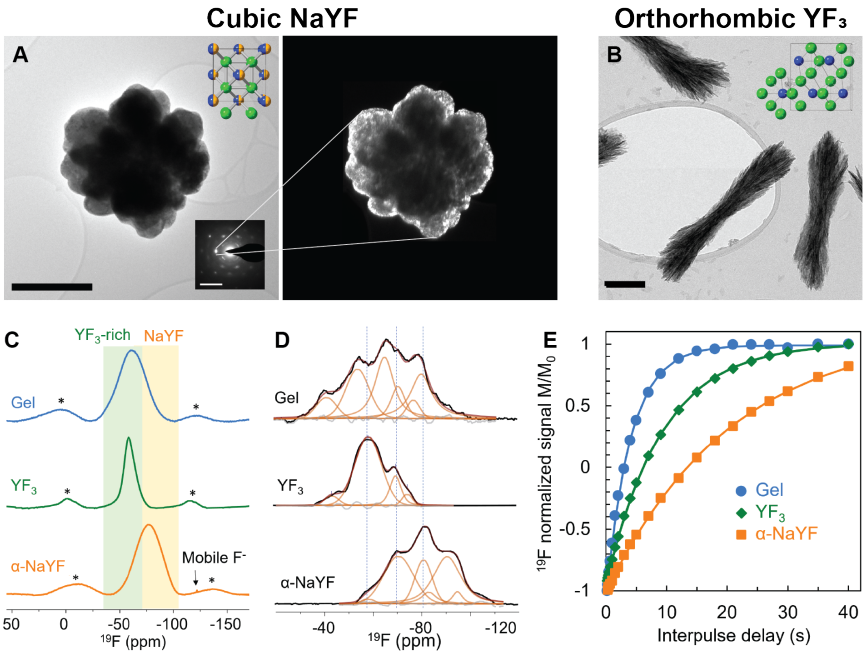

Figure 3.4: NMR experiments. ^{19}F solid state NMR comparing the gel with α-NaYF and orthorhombic YF_3 standards at 55C. (A) TEM (left), SAED (bottom inset) and dark field TEM (right) of single-crystalline α-NaYF grown from the gel. The dark field TEM indicates that the whole particle is single crystalline. Top inset shows the α-NaYF crystal structure. Scale bar = 400 nm for the TEM and 5 nm^{-1} for the SAED. (B) TEM of orthorhombic YF_3 synthesized in a similar, organic-free method. Inset shows orthorhombic YF_3 crystal structure. Scale Bar = 100 nm (C) ^{19}F spin-echo MAS NMR spectra of the gel, YF_3, and α-NaYF at a spinning speed of 32 kHz and an interpulse delay of 31.25 µs (one rotor cycle). The asterisks indicate the spinning sidebands. (D) ^{19}F Hahn-echo NMR spectra of the gel, YF_3, and α-NaYF after eight π-pulses with an interpulse delay of 65.2 µs (two rotor cycles). (E) ^{19}F inverse-recovery normalized signal intensity (markers) vs. interpulse delay of gel, YF_3, and α-NaYF as well as the fits (lines) for obtaining the spin-lattice relaxation time constant T_1. NMR performed by Ying Chen.

relax for 10,000 cycles of 0.5 fs each, the cubic YF_3 lattice became highly distorted whereas the cubic $NaYF_4$ lattice remained highly ordered, indicating that cubic YF_3 is not a stable intermediate and we would not expect it to form initially. To quantify this disorder, we calculated the average root-mean-square displacement (RMSD) of each ion in each lattice (eq. 3.1). The cubic YF_3 structure showed an average RMSD of 0.44 Å for Y^{3+} and 0.59 Å for F^- (Figure 3.5A). This is over double the RMSD calculated for cubic $NaYF_4$ of 0.19 Å and 0.26 Å, respectively (also showing an RMSD value of 0.22 Å for Na^+), again indicating that the $NaYF_4$ structure is far more stable than the cubic YF_3. In fact, this analysis

likely underestimates the actual stability of NaYF due to approximations made about the stoichiometry and the structure in the model that was used. To verify our methods, we performed the exact same MD analysis on the known stable structure of orthorhombic YF_3 (Figure S7 in Appendix C), and found RMSD values of 0.18 Å for Y^{3+} and 0.22 Å for F^-, comparable to the values calculated for $NaYF_4$. This again demonstrates that the cubic YF_3 would degrade within picoseconds and is thus not a stable product or intermediate. We would hypothesize that previously reported syntheses of cubic YF_3 were likely stabilized by the incorporation of what were assumed to be spectator cations. Even so, due to the existence of these literature reports and our TEM observations of sodium-poor crystalline regions, we also investigated whether a hypothetical cubic YF_3 structure would be able to incorporate Na^+ ions if it were stable. To do this, we performed minimum energy path (MEP) calculations using density functional theory (DFT) of ions passing through the voids in a stable cubic YF_3 crystal lattice with periodic boundary conditions. These calculations showed large energy barriers of approximately 27 kcal/mol for sodium (Figure 3.5C), 14 kcal/mol for fluoride (Figure S8A in Appendix C), and 76 kcal/mol for NaF (Figure S8B in Appendix C). This indicates that even if the cubic YF_3 phase was able to form as a transient intermediate, this would not a feasible mechanism for ion incorporation. Thus, we can conclude that the ions incorporate into the solid before it crystallizes, and any crystallization of YF_3 observed in TEM was indeed induced by the beam. This process is not simply a scientific curiosity, but can also be exploited to efficiently select between different final products in the synthesis by varying the molar ratio of NaF to Y^{3+} (Figure S9 in Appendix C). At all tested ratios, the gel initially forms due to the kinetic favorability of an initial spinodal decomposition, however at molar ratios below the stoichiometry of YF_3 (excess Y^{3+}), the gel then appears to redissolve into homogeneous solution within several minutes, and then over the course of hours colloidally stable particles begin to nucleate, which were identified crystallographically as pure orthorhombic YF_3 (to be discussed further in Chapter 4). At ratios corresponding to the $NaYF_4$ stoichiometry or higher, we observe the same multi-step process as previously described in which larger NaYF crystals nucleate directly from the gel. At the precise 3:1

(YF_3) ratio, the gel seems to remain largely stable over the course of days, with some possible nucleation occurring in the solution alongside the gel. This ability to select the crystal phase and whether or not it incorporates sodium likely exploits a "failed" two-step nucleation in the low-ratio system: one in which the amorphous YF_3 phase is initially produced but the barrier to nucleation in the orthorhombic phase is too high in the gel, so it has to redissolve and undergo a classical nucleation mechanism in order to crystallize, whereas if there is excess NaF in solution, it can incorporate into the gel and induce the crystallization of the amorphous phase into a stable cubic structure. The mechanism that allows this dissolution is discussed in more detail in Chapter 4, and is likely the result of the subsequent formation of molecular species which are metastable in solution. Thus, this crystallization pathway can act as a "switch," which determines the final chemistry and structure of the product, and which elegantly illustrates the importance of understanding mechanisms of crystallization.

$$RMSD_\alpha = \frac{1}{N_\alpha}\sum_{i=1}^{N_\alpha}\sqrt{\frac{1}{t_{MAX}}\sum_{t=0}^{t_{MAX}}|\mathbf{r}(t)-\overline{\mathbf{r}}|^2} \tag{3.1}$$

The multi-step crystal growth mechanism reported here is not only interesting in its own right, but it also motivates the study of further applications of NaYF and similar materials that take advantage of its high surface area. For example, NaYF gel materials could be useful for future energy storage applications.[289] To this end, we have demonstrated the reversible cycling of this material as an anode for sodium and lithium ion batteries (Figure S10-11 in Appendix C). This may be possible due to the capability of active ion exchange prior to crystallization. We also view this as a promising candidate for fluoride-ion batteries and plan to investigate these further in future work.[302] This material may also have promise as an anti-reflective coating,[303] which would be a particularly interesting application because of the possibility of employing the optical refrigeration properties of NaYF to actively cool the surface.[114] In preliminary experiments, we observe optical refrigeration of the NaYF gel when doped with 10% ytterbium. We find that it can be laser cooled by approximately 0.55°C and that it does not heat under 1020 nm laser irradiation (Figure S12 in Appendix C), indicating

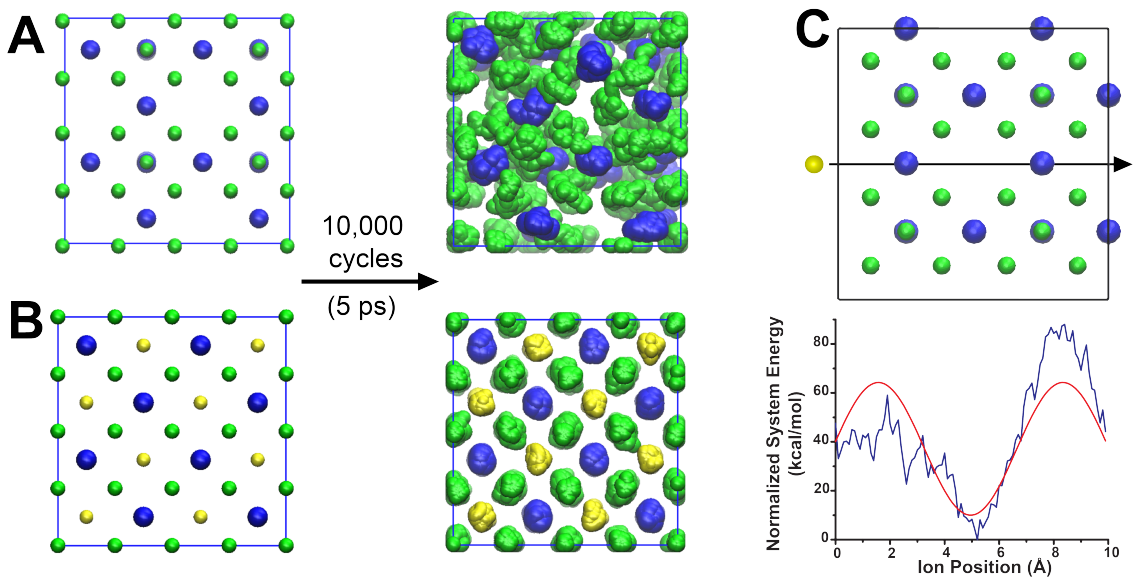

Figure 3.5: (A) Cubic YF_3 and (B) cubic $NaYF_4$ before and after performing a molecular dynamics time lapse of 10,000 steps pf 0.5 fs each, for a total elapsed time of 5 ps. The YF_3 exhibits much lower stability, indicating that cubic YF_3 is not a stable intermediate and it requires the incorporation of residual NaF from the supernatant in order to retain the cubic structure. (C) Minimum energy path of sodium traveling through the hypothetical cubic YF_3 lattice fit with a sinusoid showing an energy barrier of approximately 27 kcal/mol for a sodium ion to enter the lattice. Similar plots for fluoride and the NaF molecule can be found in Appendix C with energy barriers of approximately 14 and 76 kcal/mol, respectively. This indicates that the Na and F ions are absorbed into an amorphous or dense liquid phase rather than incorporating into a transient YF_3 lattice. Simulations performed by Michael LaCount, Chris Mundy, and Greg Schenter.

that it may be a good candidate for, for example, actively-cooled anti-reflective coatings, especially due to its lack of organic ligands on the surface, as the effective cooling efficiency of a nanocrystal is reduced by the heating of organic species on the surface.[88] It is worth pursuing the study of the nucleation mechanisms of other similar materials, as they may also have unique properties (like those of NaYF) that would benefit from a similar gel-like structure that can easily be produced by this type of mechanism.

3.3 Conclusions

Crystal nucleation and growth are often described based on the simple addition of monomer units from solution. The concept of nonclassical crystal growth adds further nuance to this

view, allowing for the possibility of growth via different pathways and subsequent structural changes. We add to this view the observation of profound compositional changes that occur as an essential part of a nonclassical crystal growth process. We have shown that upon the mixture of NaF and YCl_3 in water, a gel separates from solution which then undergoes crystallization, similar to many other two- or three-step crystallization systems, and then undergoes a process of solid-state diffusion, where the product initially resembles amorphous YF_3 but then undergoes a gradual change of chemical stoichiometry, which directly induces the crystallization of cubic NaYF over the course of several hours, and which can be "switched off" by eliminating the NaF excess. It is rational to expect that this multi-step mechanism is not limited to NaYF in particular, and as such more research is needed into other chemical systems, and particularly those which exhibit nonstoichiometry, as to the inherent role of solid-state compositional changes in their crystal nucleation and growth pathways. This also motivates further research into the atomistic detail of these reactions, for example considering surface reconstructions[304] or studying the atomic-scale physics of the incorporation of sodium ions into the amorphous intermediate.

3.4 Materials and Methods

Synthesis of NaYF gel

The gel is synthesized by mixing a 0.2 M YCl_3 solution with a 0.8 M NaF solution in nanopure water. The mixture is then inverted to fully blend. The gel is then poured into a Büchner funnel with filter paper over vacuum either immediately after mixing or after waiting a specified amount of time (as in the ion replacement experiment), rinsed with water and ethanol, respectively, and allowed to fully dry.

Ion Replacement in Gel

The gel is synthesized as described above and allowed to incubate in its original solution for a period of time, t_{inc}. After t_{inc} has passed, the sample is filtered as described above and rinsed

with nanopure water, and the product is resuspended in a solution of 1M KF. This mixture is vortexed until it appears uniform and is allowed to settle overnight. After fully settling, the product is centrifuged and washed with water and ethanol respectively and oven-dried.

Powder X-Ray Diffraction

Powder X-Ray Diffraction (XRD) samples were prepared by dropcasting a concentrated slurry of the sample onto $\langle 100 \rangle$ silicon wafers. XRD spectra were taken on a Bruker D8 Discover Microfocus diffractometer with a Dectris Pilatus3 R 100K-A 2D detector and a Cu Kα X-ray source with a 0.5 mm collimator. A Coupled $2\theta/\theta$ scan was performed from 16° to 93° with a 5.5° increment to create overlap, with a scan time of 30 seconds per θ. During the scans, the sample was oscillated in the x, y, and ϕ directions to remove the effects of texture and improve statistics. An air scatter screen was used to reduce background. Scans were integrated, indexed, processed, and analyzed using Bruker Diffrac.Eva software.

TEM

TEM images were taken on FEI G^2 TECNAI F20 S/TEM instruments at 200 kV with either a Gatan Ultrascan CCD or an FEI Eagle CCD camera. Images were processed using Gatan Digital Micrograph (DM) and Tecnai Imaging and Analysis (TIA) software. STEM Tomographic reconstructions were compiled using FEI Inspect3D software, using a simultaneous iterative reconstruction technique (SIRT) with 50 iterations. These reconstructions were then visualized using IMOD.[167] Scanning transmission electron microscopy (STEM) bright field (BF) imaging and STEM-energy dispersive x-ray spectroscopy (EDS) were performed in a JEOL GrandARM 300CF AC-STEM operated at 300 kV. EDS data were collected using dual JEOL Centurio EDS spectrometers with a 1.63 sr solid angle, and analyzed using Thermo Fisher Pathfinder software. The NaYF samples were dispersed in ethanol and dropcast onto Cu TEM grids with lacey carbon films.

Computational methods

Data processing: The TEM spatial FFT analysis was performed using a homebuilt Python script. To determine the scale, the code optically detected the scale bar printed on the image by the TEM software (Tecnai Imaging and Analysis) and a calibration factor of 22.800 pixels/nm was obtained. Points on the image were manually selected, and a region of 100 px x 100 px centered on that point was isolated. From this point the script was set up to perform automated calculations. 2D-FFT was performed for each region, followed by a Gaussian background subtraction to enhance the peaks in the reciprocal space. Several filters and masks were applied on the intensity to obtain the peak locations, which was used to determine d-spacing in the inverse space. All detected peaks were organized into a histogram based on measured d-spacing, and the region corresponding to the 111 peak for both α-NaYF and cubic YF_3 was isolated (3.00-3.16 Å), with all other measured peaks discarded. A weighted average was performed on the remaining peaks with their peak intensity as respective weights. This resulted in a single d-spacing value associated with each region. This value was then mapped onto a gradient and displayed as a circle at the center of each region on the TEM image.

Modeling: SD was simulated with a Matlab code modified from the original written by Tavakoli.[291] All codes are available for public use upon reasonable request.

Ab initio calculations were performed using version 9.1 of the CP2K quantum chemistry and solid state physics software package.[305] These DFT-based calculations used the revPBE functional plus D3 dispersion exchange correlation functional.[306,307] CP2K uses a combination of Gaussian and planewaves to construct the basis set. The Gaussian component of our basis set consisted of a double-zeta valence polarized molecular optimized basis (DZVP-MOLOPT) developed by VandeVondele et al.[308] The planewave portion of our basis set was given a cutoff of 800 Ry. Pseudopotentials developed by Goedecker, Teter and Hutter (GTH) specific to the RevPBE functional were used for all atoms.[309–311]

Our calculations can be broken up into two types: bulk crystal molecular dynamics (MD)

and ionic diffusion barrier height. The MD calculations were of the $NaYF_4$, YF_3 cubic and YF_3 orthorhombic cells. Each cell was modeled in a 2x2x2 supercell configuration. The calculations were performed in an NVT ensemble with the unit cell set to the experimental parameters. A system temperature of 300K was implemented with a Nose-Hoover thermostat with a thermostat frequency of 1,000 $c*cm^{-1}$, where c is the speed of light.[312–314] The simulations were performed for a total of 10,000 steps of 0.5 fs each. To prevent the center of the cell from drifting we applied a restraint on a single ion (Na^+ for $NaYF_4$ and Y^{3+} for YF_3), with a harmonic restraint with a strength of 100 kcal/mol/Å^2. The root mean squared displacement (RMSD) was calculated from the mean coordinate of each individual ion throughout the 10,000-step run using equation 3.1, in which each ion is denoted as α. These were then averaged for all ions of the same type to calculate the reported values.

The second set of calculations were of the diffusion barrier height of an ion traveling through the YF_3 cubic cell. Initial the YF_3 cubic cell had an additional ion placed at a fixed position at relative coordinates (0.5,0.5,0), the rest of the atoms in the cell were given a center of mass harmonic restraint with a strength of 100 kcal/mol/Å^2. In the initial configuration for 4,800 steps using the same MD parameters as the previous set of calculations, except in an NPT ensemble. The calculations were performed at a constant 1 bar of pressure, and the barostat had a time constant of 300 fs. After the initial 4,800 steps, 20,000 more steps were calculated except the z-coordinate was shifted +0.1Å every 200 steps in the z-axis, starting at 0.0Å and ending at 9.9Å. The potential energy was averaged throughout the 200 steps, and then plotted against the z-position of the ion. We estimate the diffusion energy barrier to be the difference between the minimum and maximum of the resulting plot.

NMR

^{19}F and ^{23}Na magic angle spinning (MAS) NMR spectra were collected on a Bruker Avance III spectrometer with a field strength of 600 MHz (14.1 T, corresponding to 564.71 MHz for ^{19}F and 158.75 MHz for ^{23}Na) using 2.5 mm Bruker rotors at a spinning speed of 32 kHz. The regular 90° pulse width was 3.1 µs for ^{19}F and 2.9 µs for ^{23}Na. ^{19}F spin-lattice relaxation

times (T_1) were measured using the inversion-recovery method (180° - τ_{delay} - 90°- acquisition), and spin-spin relaxation times (T_2) using the Carr-Purcell-Meiboom-Gill (CPMG) method (90°- τ_{delay} - [180°- $\tau_{delay}]_n$ - acquisition) after 2 – 96 π-pulses with an interpulse delay time τ_{delay} = 62.5 µs, which was synchronized to the spinning speed of 32 kHz. The spin-echo ^{19}F spectra were acquired after two rotor cycles with an interpulse delay of 31.25 µs. Single-pulse ^{23}Na spectra were acquired with a hard RF pulse with a π/20 flip angle of 0.58 µs, while soft RF pulses (90° pulse width at 15 µs) was used for preferentially exciting central transitions in the inverse-recovery experiments. Relaxation delays of 5 × T_1 (60 – 200 s for ^{19}F and 1 – 2 s for ^{23}Na) were used in all experiments to ensure the full relaxation of all samples. The ^{19}F chemical shift references were CF_3CH_2OH at -76.55 ppm and solid NaF at -224 ppm as a second reference. ^{23}Na chemical shifts were referenced to 1 M NaCl aqueous solution at 0 ppm.

Chapter 4

CONCENTRATION-SELECTIVE NUCLEATION "SWITCH" IN THE YF_3-$NAYF_4$ SYSTEM

One thing that we have found about the NaYF nucleation system is that with every new thing we learn about it, it also provides us with even more new questions and intricacies waiting to be solved. It seems that this area of study is one which we may never need to give up for lack of interesting new directions.[315] For example, in Chapter 3, we discussed the multi-step nucleation of NaYF in water. We found that the process begins via a liquid-liquid phase separation of, likely, a YF_3 species from the solution, which then requires the further diffusion of excess NaF from solution into the dense liquid phase in order to crystallize into NaYF. The natural next question to ask, then, is what happens if there isn't enough fluoride left in solution following the initial phase separation for it to crystallize? We briefly addressed this question in the previous work, specifically in Figure S9 in Appendix C, in which we observe that when mixing NaF and YX_3, where X = Cl or NO_3, a gel forms regardless of initial concentration, but the previously-described multi-step crystallization process only occurs at F:Y ratios greater than 3. If the F:Y ratio is less than three, however, we observe a very different mechanism in which the gel forms and then appears to dissolve away and renucleate from solution. Not only is the mechanism different, but the product is also different. In the excess-Fluoride regime, we collect cubic NaYF as a product. However, in the excess-Yttrium regime, we collect orthorhombic YF_3. What this means is that the crystal growth mechanism itself allows the concentration of the initial reactants to behave as an on-off switch to determine the final product, revealing a mechanism that truly intertwines crystal growth and chemistry. While this work is still in progress, I view it as the ultimate culmination of all of the discussion so far of NaYF and a true realization of the concept that

crystal growth and chemistry are not separate processes, which is the most important point in this dissertation.

4.1 Introduction

It is ubiquitous in the scientific literature to find detailed descriptions of chemical mechanisms of solution-based reactions, meticulously describing the formation and breaking of bonds, the movement of electrons, and the interactions of the species of interest with their surroundings.[316–318] It is also ubiquitous in the scientific literature to find detailed descriptions of crystallization mechanisms from solution-based syntheses, looking very precisely at the classical and non-classical ways that monomer units of a particular material arrange themselves into useful solid structures.[1,319,320] However, there is often an implicit assumption that these are separate processes—that molecules form in solution and then arrange to form solids. But this assumption is based on an antiquated view of crystallization in which crystals must be built directly from monomer units, and we now know that that is far from the only way that crystals can be built.[6,30,263,321,322] As such, it is worth revisiting when, during a crystallization process, chemical reaction can occur and when, during a chemical reaction mechanism, crystallization (or steps toward crystallization) can occur. While we are certainly not the first to consider the possibility that crystal growth and chemistry could affect each other,[323–325] we observe a very stark example of this interplay that fundamentally involves both the chemical mechanism and the crystal growth pathway in determining the product.

As in the preceding chapters, this was studied in the synthesis of NaYF. In particular, we return to a question that we originally posed (and attempted to address) in Chapter 3 regarding the relationship between NaYF and YF_3. In the literature, we find reports of both cubic and hexagonal NaYF, and we also find reports of both cubic and orthorhombic YF_3. In Chapter 3, we were able to show through modeling and experimentation that the often-reported cubic YF_3 structure is not stable. We also demonstrated in that chapter that an amorphous (or dense liquid) phase is formed during this aqueous synthesis that likely has an initial composition resembling YF_3, into which residual Na^+ and F^- can diffuse, allowing

for the two-step nucleation of cubic NaYF. This led to the question of what would happen if there was not enough NaF left in solution to continue the crystallization process past the initial phase that separates from solution. If the initial phase is YF_3, as we concluded previously, then surely we should still expect it to separate from solution, as its solubility has not fundamentally changed. But without NaF to stabilize the crystal lattice, and with the knowledge that cubic YF_3 is not stable, it is challenging to predict what might occur. One may reasonably predict that orthorhombic YF_3 would form, and that prediction turns out to be correct, but prior experimental data have shown that reactions that produce cubic NaYF can simply be heated to convert the product to either hexagonal NaYF[1,326] or orthorhombic YF_3.[215] This indicates that the cubic phase is a kinetic product, and thus it forms as a result of Ostwald's step rule. What this means is that it is necessarily harder to form these thermodynamic products in these reaction conditions than it is to form cubic NaYF. As such, the system has to "figure out" how to make YF_3 without being able to go through cubic NaYF, and that pathway is the focus of this study.

Here we present this "switch" mechanism that determines the composition and crystalline phase of the product via the chemically-forced crossover of the crystallization pathway. We present experimental and computational data that provide insights into what is happening, and we also discuss some future work that will help us to fully grasp the process that occurs and what it can tell us about not just the NaYF-YF_3 system but also how it informs the questions we should be asking about any chemical reaction that produces a solid, and and crystal growth process that arises from a chemical reaction.

4.2 Results and discussion

Upon mixing NaF and YX_3 (where X = Cl or NO_3) at any ratio, a gel immediately forms, as we observed in Chapter 3 (Figure 4.1A and B). At F:Y ratios of 3:1 and greater,* this gel remains relatively stable for the first hour or so. However, at ratios below 3:1, the gel

*For the sake of simplicity, all ratios given in this chapter can be assumed to refer to the F:Y ratio unless otherwise specified.

appears to dissolve back into solution. After allowing the crystallization process to continue overnight, the mixtures above the 3:1 ratio (in the excess-F regime) undergo the coalescence process described in Chapter 3 to form cubic NaYF single crystals (Figure 4.1D). In contrast, the mixtures below a 3:1 ratio (in the excess-Y regime) form a stable colloid containing orthorhombic YF_3 particles, as confirmed by powder X-ray diffraction (Figure S1 in Appendix D) that adopt a distinct morphology that has been variously described as nano-bundles or dog bones (Figure 4.1C) that are approximately 400 nm in length and 100 nm in diameter. The mixture at exactly a 3:1 ratio is not currently well-characterized but initial observations possibly suggest a mixture of the two products. Further research is also needed to characterize the region between a 3:1 ratio, which is stoichiometric to YF_3 and a 4:1 ratio, which is theoretically stoichiometric to $NaYF_4$.

One of the most striking observations of the mixtures in the excess-Y regime is the formation and subsequent apparent dissolution of the gel phase. To understand the dissolution itself, we plan to use cryo-TEM to halt the dissolution process at various points so that we can microscopically study the microstructure as it evolves. However, if there is indeed dissolution occurring, TEM will not be able to provide insight into the dissolved molecular species. To understand these species, we used solution-phase ^{19}F NMR to study the local environment of solvated fluorides (Figure 4.2). For a 1:1 mixture, with t=0 referring to the moment that the gel dissolves, we observed a sharp peak at -49.3 ppm that likely corresponds to YF_3,[327] which persists for the duration of the experiment, as well as six other broad peaks ranging from approximately -36 to -89 ppm, which decrease to baseline over the course of five minutes. These peaks may correspond to solvated YF_n species that transiently form and interact to form the solid YF_3. These species may also coordinate OH^- and OH_2 from the solvent, leading to a potentially more complex structure.* This agrees with some preliminary molecular dynamics simulations we have run that suggest that multiple YF_n species are

*Both YCl_3 and $Y(NO_3)_3$ form acidic solutions in water, indicating that Y^{3+} spontaneously coordinates OH- ions. A detailed *in situ* pH study of the YF_3 nucleation may help us to understand what is happening with these OH- ions over time.

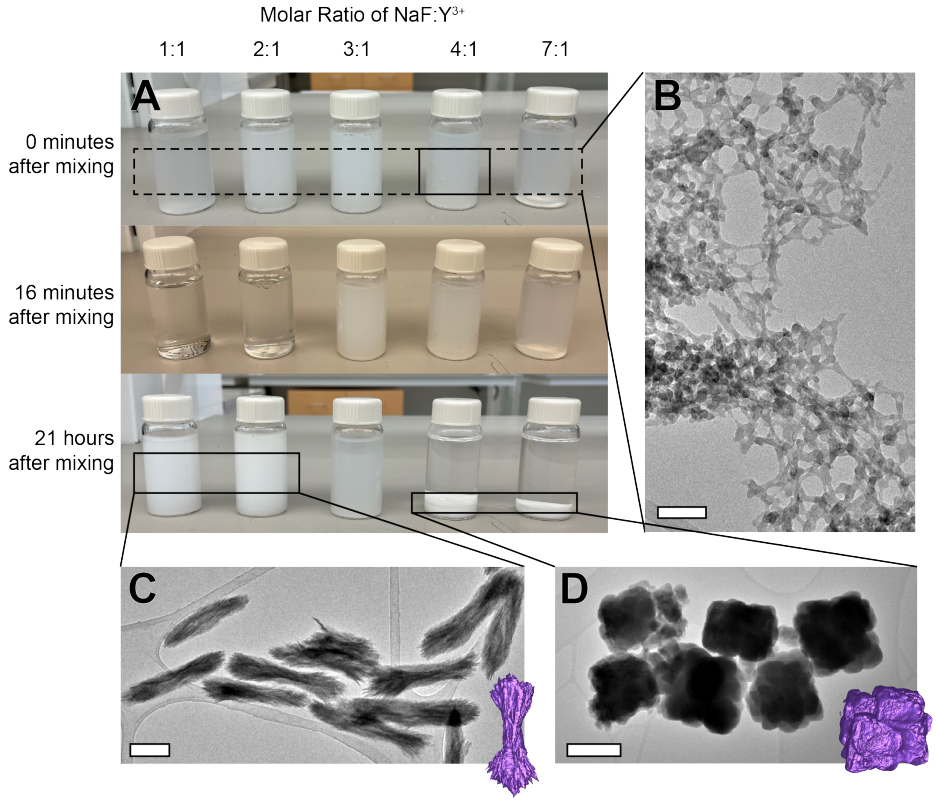

Figure 4.1: The result of mixing $Y(NO_3)_3$ and NaF at different ratios over time. (A) Time lapse showing immediate gel formation followed by the dissolution of the gel phase at the ratios below 3:1 after 16 minutes and then the nucleation of colloidally stable YF_3 and the collapse and settlement of NaYF after 21 hours. (B) Example TEM image showing the gel phase (TEM of 4:1 ratio, other gels assumed to be similar based on experimental observations with experiments ongoing to confirm morphology). Scale bar = 50 nm (C) Example TEM image showing the YF_3 phase with inset tomographic isosurface. Scale bar = 200 nm. (D) Example TEM showing the cubic NaYF phase with inset tomographic isosurface. Scale bar = 200 nm.

initially stable in solution, for example those shown in Appendix C Figure S3. Furthermore, these simulations have shown that they can form bridging fluorides, potentially suggesting the possibility of the formation of oligomeric clusters. These computational efforts are ongoing and we plan to use the computational results to inform future experiments. In contrast to the YF_3 system, the *in situ* NMR for the 4:1 mixture that produces NaYF is quite boring, with no visible speciation and the only discernible signal appearing as a sharp peak around -121 ppm, which likely corresponds to excess NaF.[328] A likely explanation for this is that

all of the chemistry in the NaYF system happens in the solid phase. We have thoroughly described the initial liquid-liquid phase separation, which leads to an amorphous phase that slowly crystallizes as NaF is incorporated into the structure. Because all of the Y-F bonds exist in the solid phase, we do not observe their signal with liquid phase NMR, whereas in the YF_3 system, the gel redissolves into these YF_n species that then renucleate YF_3, possibly through cluster intermediates. This serves to emphasize that subtle changes in the chemical environment can lead to profound changes in the crystallization mechanism, which can in turn lead to profoundly different products.

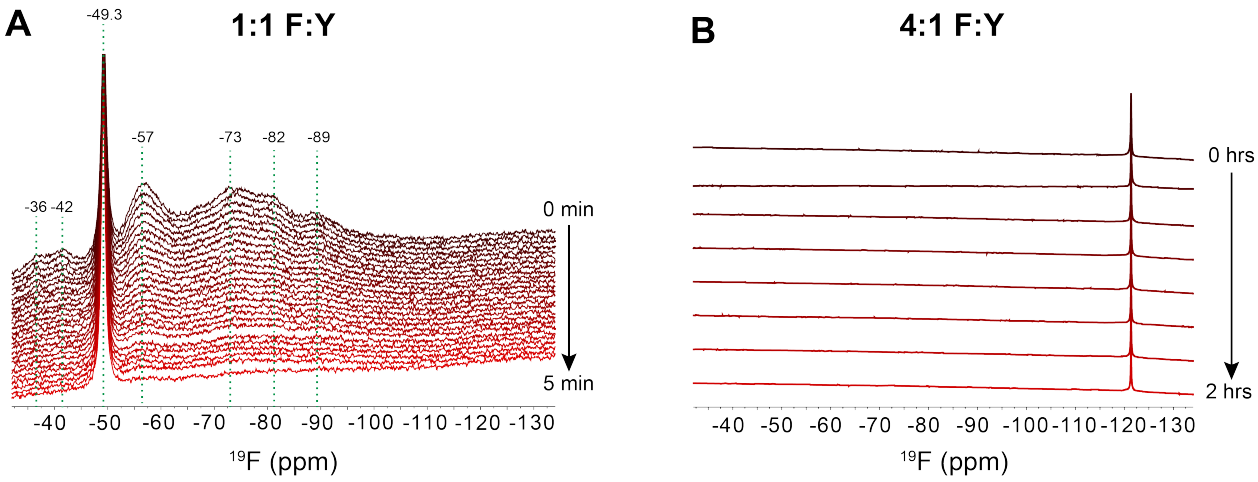

Figure 4.2: *In situ* ^{19}F NMR of the mixing of $Y(NO_3)_3$ and NaF at (A) a 1:1 F:Y ratio and (B) a 4:1 F:Y ratio. Time point 0 in (A) corresponds to the dissolution of the initial gel phase, showing the formation of various solvated species that likely correspond to different values of n for YF_n in the earliest stages of formation of the YF_3 species that corresponds to the peak at -49.3 ppm. (B) shows no such formation of solvated species in the formation of NaYF, with the peak at -121 ppm likely corresponding to residual NaF. NMR performed by Ying Chen.

With the understanding that this system involves complex interplay between chemistry and crystallization, we need to fully characterize both processes. NMR gives us insight into the chemical environment, and we may also be able to use solid-state NMR to learn more about the solid phase, but we can also use other methods to study the crystal growth process. Ideally, we could take a cryo-TEM (or even ex-situ TEM) series with samples taken at various points in the growth process. However, given that the YF_3 takes approximately 20

hours to fully develop, this would necessitate a very laborious, likely multi-person sample collection process, which we have not yet had time to attempt, however which is also I believe crucial to fully understand this system. Until we are able to collect that TEM data, however, we can use dynamic light scattering (DLS) to help us to begin to understand the process. DLS works by measuring the light from a laser that is backscattered by particles moving in Brownian motion in solution, and then performing an autocorrelation function to determine how fast they move in Brownian motion, which is in turn a function of the average hydrodynamic radius of the particle (i.e. the particle and its hydration sphere). As such, DLS is a quite indirect method of measuring particle size, but what it lacks in directness can be made up for in ease of measurement. Scattering can be measured nearly instantly and all of the post-processing can be performed in real time. This makes DLS an extremely versatile first-line method for estimating the size of particles in solution. Furthermore, if a reaction can be run inside a cuvette, then the particle size can be estimated *in situ*. For the 1:1 YF_3 system at a 0.2M concentration of each species, we observed a very distinct DLS signal (Figure 4.3) where there seems to be a bimodal distribution of particle sizes for the first ∼10 hours of growth that both grow in a nearly linear trend. At ∼10 hours, this abruptly shifts to a single phase that initially appears to decrease in size but then grow at a higher rate order than previously.* After approximately 24 hours, there is another abrupt change in trend to a roughly linear decrease, which could be attributable to larger particles settling below the laser beam. While it is difficult to claim anything definitive about the growth process from these data, it would be reasonable to hypothesize that the abrupt change around 10 hours and the apparent disappearance of the small particles is a result of a change in the crystal growth mechanism. Especially because the YF_3 particles are known to be polycrystalline with some ordering (Figure 4.1C), it is certainly reasonable to hypothesize that its growth mechanism includes assembly to some degree, as has been observed in other studies of similar

*We observe a concentration dependence for this trend such that at higher concentrations, the growth occurs faster and the observed decrease in radius occurs sooner and is more pronounced, but these data are at this time still being collected and analyzed.

nano-bundle/dog bone-shaped particles.[329–331] One possible mechanism could involve the classical growth of monomers and loose assemblies during the first ten hours transitioning to an oriented assembly-based growth mechanism. The initial contraction could be attributable to the initially disordered aggregates (Figure 4.3 inset A) adopting a more efficient packing (Figure 4.3 inset B), with the ensuing growth being attributable to further pseudo-oriented growth. This hypothesis could be tested with further time-resolved TEM measurements. DLS is not sufficient to confirm any particular mechanism, however it does show us that the crystals are not growing and that something happens at 10 hours, which helps us to narrow down the most important time points to study further with other methods. Due to DLS being an indirect measurement technique, we have to consider that the autocorrelation function tends to obscure the difference between signal and noise, that the hydrodynamic radius can change, for example, due to changes in the ionic strength of the solution (rather than changes in particle size), that the morphology of the particles can affect the hydrodynamic radius, and that larger particles tend to settle. With that in mind, our data are clearly consistent with a complex, multistep crystal growth mechanism that deserves further study.

While we know that the aqueous YF_3-NaYF system proceeds via a mechanism that includes a chemically-driven crystallization "switch," at the present time more research is needed to fully understand the growth of the YF_3 particles following the switch. NMR and DLS data are consistent with a mechanism that may initially involve the formation of multiple YF_n species that then begin to form a YF_3 lattice, which then undergoes a multistep growth mechanism that may involve the formation of loose aggregate that then transform to the ordered aggregates that we observe *ex situ*. In order to increase the degree of precision in which we can describe this mechanism, we need to consider a few more experiments on this system. To further understand the early-stage speciation that we observe with NMR, we can use atomistic simulations to understand the stability of these species and to help elucidate the hydration sphere. Preliminary simulations show that multiple YF_n species can form in solution and form bridging oligomers. If we can simulate NMR patterns for these which are consistent with our data, that would confirm that we are observing that

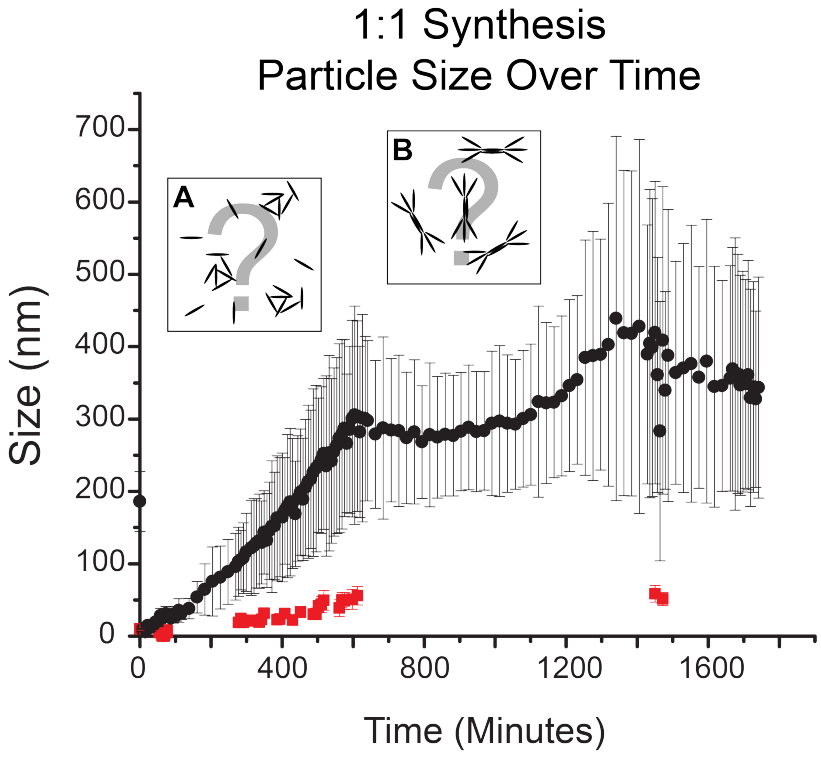

Figure 4.3: *In situ* DLS measurement of the 1:1 mixing of YCl_3 and NaF (0.2M each), with t=0 corresponding to the moment that the gel redissolves. The apparent decrease in diameter around 24 hours likely can be attributed to larger particles settling out of the laser beam. The apparent decrease in size at 10 hours is a subject on ongoing research but could be attributable to a transition between modes of crystal growth, for example transitioning between loose aggregates (inset A) and pseudo-oriented aggregates (inset B). DLS measurements performed by Ivan Liu.

speciation. Measuring the pH as a function of time after mixing may also help to understand the attachment and detachment of OH- ions. Finally, cryo-TEM would allow us to observe the early-stage nucleation of solids during those first five minutes, as well as prior to the full dissolution of the gel. For the later stage growth as described by the DLS data, TEM would immediately tell us whether or not we have disordered aggregates becoming ordered at 10 hours. Cryo-TEM would best preserve delicate structures, however ex-situ TEM would most likely tell us what we need to know with much less labor. Small-angle X-ray scattering (SAXS) would also help us to understand the size and shape evolution in the bulk with a

much greater degree of precision than DLS. SAXS is a realization of Bragg's law that allows for sizes and shapes of particles to be accurately modeled in the nanometer scale based on how the particles scatter X-rays. In a similar vein, *in situ* X-ray diffraction (XRD) could allow us to measure the size of crystalline domains from different directions using a Scherrer analysis, allowing us to understand the morphology of the individual crystallites and the degree to which they may or may not undergo oriented attachment as opposed to oriented aggregation.

4.3 Conclusion

Here we demonstrate a "switch" mechanism in the YF_3-NaYF system in which we can direct both the composition and the crystal phase of the product simply by making a small adjustment to the ratio of the reactants that is consistent with the redissolution and speciation of YF_n molecules that then reorganize into orthorhombic YF_3 rather than settling into an unstable cubic phase. This emphasizes that crystal growth is fundamentally a chemical process and that it should be viewed as a part of a chemical reaction rather than a separate step. This also further emphasizes the intertwined relationship between NaYF and YF_3, and suggests that, just as cubic and hexagonal NaYF are polymorphs of the same compound with variable stoichiometry that form under different conditions, orthorhombic YF_3 belongs in the same family. Aside from the fundamental questions of science that these results lead us to consider, we could also consider the engineering of microstructures within inclusions of varying concentration, perhaps using more complex solvent systems or chelating ligands. With further regards to chelating ligands, this may help to elucidate their usefulness in various hydrothermal rare earth fluoride systems and inform how their modification may affect the product. One could even imagine the use of this system as a very slow and inefficient logic gate! We can see already that this is a complex and interesting system, and in order to fully do it justice we still need to study the YF_3 growth process in detail using techniques such as time-resolved TEM and SAXS in order to unveil the various steps in the growth process and whether they can also be modified to further tune the end product.

Chapter 5

MICROFABRICATION FROM BULK AND MEASUREMENT OF NANOSCALE DIAMOND TIPS FOR ATOM PROBE TOMOGRAPHY

Aside from the NaYF work, I also spent a considerable time working on APT projects. As described in Section 1.3.2, APT allows us to measure atoms in a solid in three spatial dimensions and determine their identity. This technique can help us to understand the local structure of materials, which can help us to understand, for example, the homogeneity of a dopant. In the NaYF system, this could potentially allow us to look at the gel immediately after it forms to study the sodium incorporation, which would give us a far better understanding of that solid-state diffusion process than what we currently have. However, due to the physics of how APT works, there is a need for the sample to be roughly needle-shaped, and the only way to do that with the gel would be to freeze it, lift out tips of the gel within the ice matrix, and run cryo-APT experiments on that. This is entirely possible,[332–334] and I would like to see these experiments happen in the future, however the sample preparation process for cryo-APT specimens is considerably more involved and as such we wanted to start with something a little bit more straightforward.

We decided to use diamond for this purpose because it is widely used in quantum applications in which very low-concentration point defects can have profound impacts on its spectroscopic properties. Additionally, while the process may not be quite as technically difficult as a NaYF cryo-APT experiment would be, the experimental details are not necessarily straightforward and present some interesting challenges to overcome, mainly stemming from diamond's natural hardness. Sample preparation is difficult because of diamond's resistance to milling, and once the sample is made, it is difficult to measure due to diamond's resistance

to field evaporation combined with its low conductivity. We work to overcome these challenges by replacing much of the milling that would traditionally be done with a focused ion beam with a reactive ion etching process, and we show that we can collect quantitative APT data by increasing the laser pulse energy, which is enabled by diamond's extremely high thermal conductivity. We find that, while these properties do present challenges, they can be overcome, and furthermore that they may actually be beneficial for certain applications, such as in the manufacture of APT sample mounts, which ideally should have a lower evaporation field and a higher thermal conductivity than the sample that is mounted on it.

5.1 Introduction

Diamond has been heavily studied in recent years for many applications related to the inclusion of point defects.[335–340] Diamond is a particularly good host lattice for these defects (often referred to as color centers) due to the extreme strength and stability of its crystal lattice.[341,342] Additionally, due to the fact that diamond is nontoxic, diamond color centers are attractive options for *in vivo* applications in medicine and life science.[343–345] However, these color centers begin to interfere with each other if the concentration is too high, therefore limiting the practical concentration of point defects to roughly the ppm order or magnitude.[346,347] This can present a problem for standard nanoscale elemental analysis techniques such as energy dispersive X-ray spectroscopy (EDS) and electron energy loss spectroscopy (EELS), which typically have detection limits no higher than roughly parts per thousand.[348] Thus, it is challenging to achieve any degree of spatial resolution in determining the local concentrations of color centers.

For this reason, atom probe tomography (APT) has emerged as an attractive option to study color center concentrations in bulk diamond.[349,350] APT relies on the field evaporation of a sample that has been milled to a fine point, which can release ions at a controlled rate toward a 2D time of flight mass spectrometer.[184] This results in detection limits closer to the ppm range while preserving spatial resolution, which is ideal for studying the local concentrations of point defects.[351] Furthermore, APT is capable of detecting hydrogen, which

is not possible with X-ray fluorescence-based methods.[352–354] However, diamond inherently poses unique challenges for APT due to the nature of how APT works. The field evaporation process in APT is controlled by the application of a local electric field near the tip somewhat below the level required to induce spontaneous field evaporation, and in order to control the timing of ion release, either the electric field itself or an external UV laser is pulsed (typically the laser-assisted option is used for nonconductive samples to minimize strain) to release ions at a known time point.[184] Diamond, however, is a material that is renowned for its extreme hardness, and that property is preserved at the nanoscopic level as well, leading to it having the highest known evaporation field of any elemental material in excess of 150 V/nm.[350,355,356] By comparison, silicon (which is commonly used for mounting APT specimens) has an evaporation field closer to 33 V/nm.[357] This means that diamond requires much more energy in order to induce field evaporation. Besides any instrumental limitations that may exist, this is theoretically not a problem for conducting samples that can distribute charge to the surface and concentrate at the tip. This is another area in which diamond does not excel, as diamond natively has extremely low conductivity,[358] which leads to a buildup of internal charge that can cause the sample to rupture.[184] This can be mitigated to an extent by using boron-doped diamond in order to make it more conductive,[350] but we would like to be able to study any diamond sample in its native state without additional dopants. Thus, we need to focus on the methods used to prepare and measure samples in order to ensure the best possible result.

The preparation of APT tips of diamond can be a challenge in and of itself. Most APT samples are prepared by a focused ion beam (FIB) bulk liftout method in which a bar is lifted out of a bulk sample, sectioned onto tips, and subsequently sharpened.[359] This is a very versatile method, and one that has been used for bulk diamond samples before,[349,350] but bulk liftouts that remove large amounts of material can be problematic for diamond. Due to the extreme hardness of diamond, the FIB milling requires a substantially higher ion dose than similar liftouts of other materials, which has the effect of increasing milling time, decreasing precision, and introducing more defects both by disrupting the lattice and implanting gallium

ions.[360–362] As such, any interaction with the ion beam that can be eliminated will have the effect of speeding up processing time and reducing opportunities for sample damage.

Once a sample is prepared, APT measurement can be a challenge as well. As mentioned previously, diamond has an extremely high evaporation field combined with an extremely low conductivity and high brittleness. What this means is that the field evaporation requires a higher-than-normal amount of energy to occur, but too high of a voltage will cause the tip to rupture. Luckily, laser-assisted atom probe technologies allow for lower voltages to be used by thermally exciting atoms over the barrier to evaporation.[363] Normally, the energy contribution from the laser pulse is chosen to be relatively small compared to that of the applied voltage.[364] This is both to prevent sample damage from overheating the tip and to prevent thermal tailing of the mass spectrum.[365] Thermal tailing occurs because the timing of the laser pulse sets the zero-point for the time-of-flight mass spectrometer, and so ions are assumed to be ejected at the exact moment of the laser pulse, but for samples with a finite heat capacity, ions may be released at any point while the sample remains above the critical temperature for field evaporation, leading to peak broadening.[187] This is an area, however, where we can use the properties of diamond to our advantage. Diamond has an extremely high thermal conductivity which allows it to readily disperse heat throughout the lattice.[366] As such, we would not expect thermal tailing to be as much of a problem, and therefore higher laser pulse energies can be used to assist in field evaporation. This is not only useful in the collection of data on diamond directly, but also potentially in the engineering of APT sample mounts that can reduce background and even wick away heat, which may be especially useful for "extreme" atom probe techniques that use much more powerful lasers.[367,368]

In this manuscript, we discuss the preparation and APT measurement of diamond tips using a novel reactive ion etching method to produce a large number of tips that can be directly lifted out and mounted with far less FIB processing required than a typical diamond liftout procedure. This method has allowed us to rapidly collect APT data on diamond with information on defects including hydrogen, while avoiding many of the pitfalls associated with a direct FIB liftout. We also show heat transfer models to quantify our observations

demonstrating the ability of diamond to survive high energy laser pulses without significant thermal tailing.

5.2 Results and discussion

In order to minimize the interaction of the diamond sample with the FIB, we produced an array of pillars on a wafer consisting of 10 μm of chemical vapor deposition (CVD) diamond on a sapphire substrate using reactive ion etching (Figure S1). These pillars were roughly conical with a base of 2 μm and a height of 10 μm. This is an ideal size because the mounting posts on a standard APT sample chip have a diameter of 2 μm, however the process could easily be adapted for a mounting post of any size. To mount these tips on a sample chip (Figure 5.1) the pillars were first coated with a thin protective layer of platinum using the electron beam and then a thicker ($\sim$0.5 μm) layer of platinum was deposited with the ion beam. The stage was then tilted back to vertical (52° to the ion beam) and a probe was attached, and the pillar was then cut near the base. The detached pillar was then brought to the mounting post and platinum was deposited to fill the gap underneath the cut. The sample was then rotated 180° and a thin layer of platinum was deposited to fill any gaps on the backside. The tip was then sharpened using a standard sequential annular milling technique (Figure 5.1E),[359] however due to the existing shape of the tips, far less milling is required for the sharpening step than what is typical for a standard liftout. Furthermore, it would also be feasible to use lower voltages to sharpen the tips to further reduce ion implantation, whereas that would be prohibitively time-consuming for a standard liftout, and that is an area of current study.

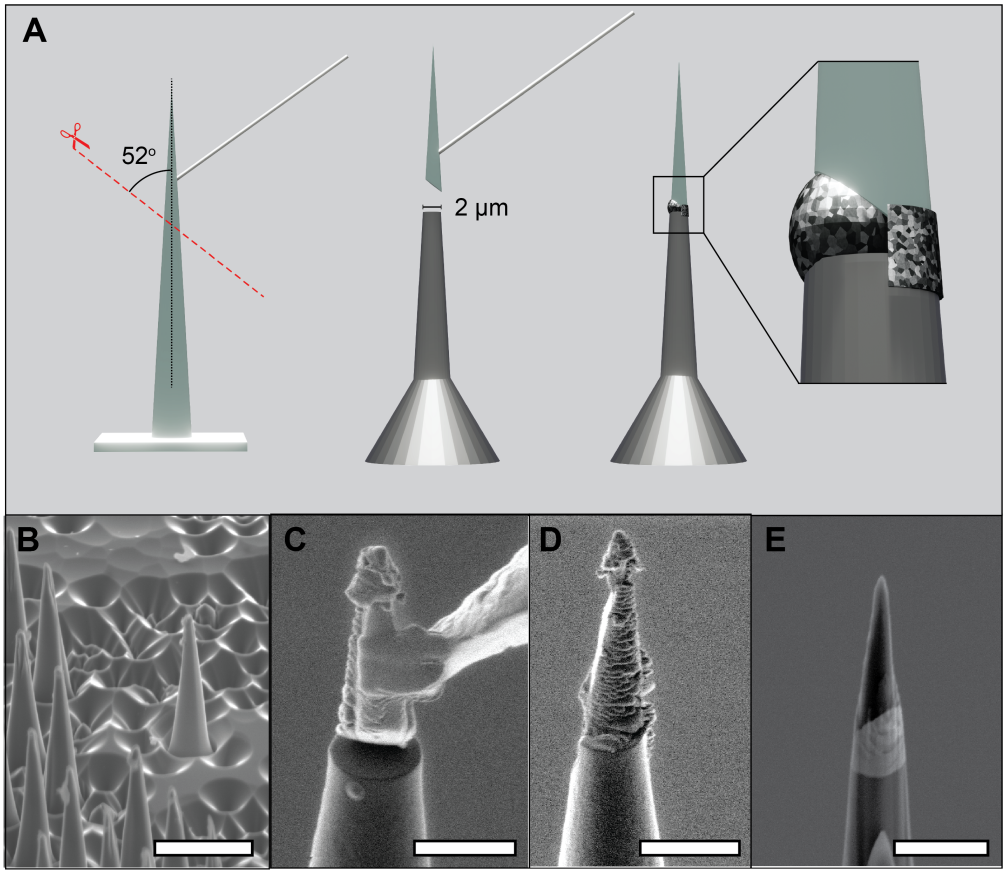

Figure 5.1: Mounting of the diamond tips on the silicon micropost arrays. (A) Schematic of the mounting process showing the initial cutting of the diamond posts at an angle of 52° from vertical, then the placement and platinum weld of the diamond on the post. Inset highlights the asymmetric weld. (B-E) SEM images showing the same mounting and sharpening process. Scale bars for B=5 μm, C=2 μm, D=3 μm, E=2 μm. Reactive ion etching of diamond pillars done by Rainer Stöhr.

We were able to successfully collect APT data on these tips at laser pulse energies of 200, 250, and 500 pJ. All of the tips eventually fractured, however we were able to collect significant data prior to the fracture. A typical one of these runs is shown in Figure 5.2, at 200 pJ of laser pulse energy, we were able to measure a mass spectrum that showed many peaks, including carbon clusters up to C_7 as well as various organic species, hydroxides, water, and hydrogen. There was also significant gallium implantation throughout the measured tip.

A concentration profile along the z axis (Figure 5.2A), decomposing complex ions to their respective elements, showed a relative increase of Ga, O, and H near the tip, indicating a higher degree of damage. The hydrogen and oxygen appear correlated due to the relatively high concentration of OH and OH_2 ions measured near the tip. Nitrogen counts are low but measurable, and do not show any strong compositional trends along the z direction, however low overall nitrogen counts may obscure some trends. This is nonetheless notable because this sample was not intentionally doped with nitrogen, though we did observe photoluminescence from nitrogen, indicating that intentionally-doped nitrogen should be readily measurable with these techniques. It is also notable that we did not observe an increase of nitrogen near the tip correlated with the increase in oxygen and hydrogen, given that the samples were stored in air. This indicates that nitrogen observed in diamond samples is likely to be native to the sample and contamination from atmospheric nitrogen is not a major concern.

Reconstructions showing the individual species of interest (Figure 5.3) further illustrates the previous observation from the depth profile. By looking at a cylindrical region of interest internal to the tip, we can eliminate surface effects, showing even more clearly that hydrogen and gallium decrease as the distance from the tip increases. Hydrogen is worth particularly careful examination due to the multiple sources of hydrogen that may be present. CVD diamond natively contains abundant hydrogen impurities,[369] and as such we would expect a relatively homogeneous hydrogen concentration throughout the bulk. We also established in Figure 5.2 that hydrogen and oxygen are correlated due to OH and OH_2, which is more abundant near the surface. Finally, APT typically has a significant hydrogen background due to the challenge of building vacuum systems that are impermeable to hydrogen.[370] It is challenging to deconvolute these signals, however it is nonetheless promising to be able to use a technique that can measure hydrogen directly, especially for samples that have a non-homogeneous hydrogen distribution, as can be seen at the tip of our reconstruction, likely from hydroxides. Nitrogen and gallium are more straightforward to interpret, however due to the low overall counts of nitrogen, there is necessarily a greater contribution of noise to its reconstruction. Additionally, we also have to consider that undercounting of nitrogen is a

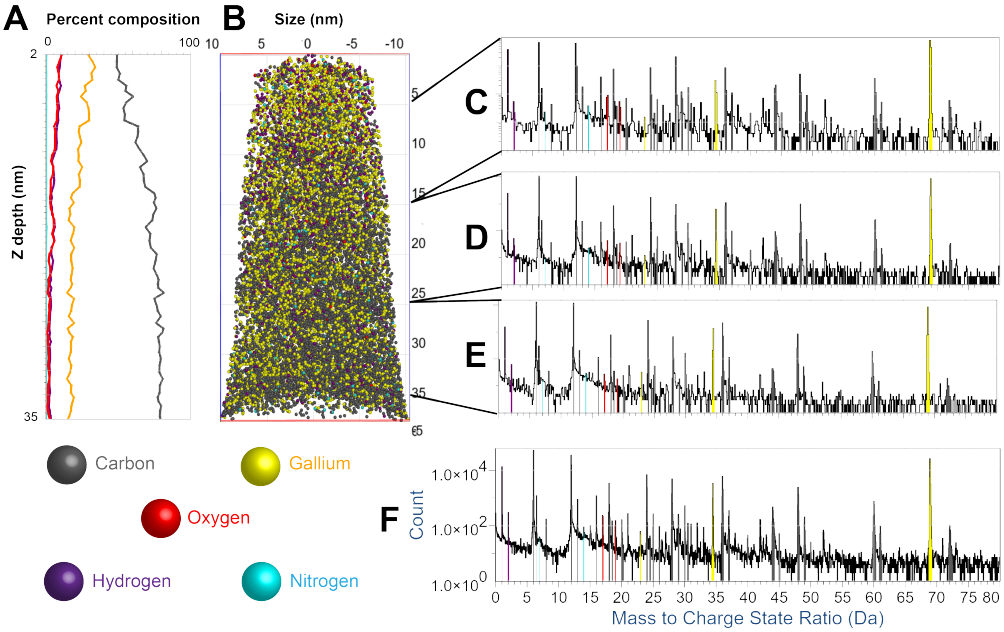

Figure 5.2: Mass spectrometry analysis of diamond tip. (A) Percent composition of each element as a function of z-height, with complex ions decomposed to their atomic species. Note that the line for nitrogen is near zero and the line for hydrogen is partially obscured by the line for oxygen. (B) Top level reconstruction showing distribution of ions within the diamond tip. All ions shown as spheres at 10% of the total number of counts. Note that some carbon counts include multiple carbon atoms. Tip diameter was arbitrarily selected to improve resolution in z and thus units of distance are arbitrary. (C-E) Regional mass spectra of 10 unit sections of the tip including the entire width of of the tip, at lengths of (C) 5-15 units from the tip, (D) 15-25 units, and (E) 25-35 units. The top 5 units were skipped to avoid surface species. (F) Full mass spectrum of the top-level reconstruction.

known issue in APT, attributable at least in part to the formation of neutral N_2 species.[371] However, due to the low overall concentration of nitrogen in this diamond sample, we do not anticipate that dimerization is likely to occur significantly among nitrogen point defects during APT analysis.

As previously discussed, one benefit to this method of sample preparation is the lower overall interaction the tips have with the ion beam during sample preparation. This should have the effect of reducing the damage that the tip suffers prior to APT measurement. To study this with APT, we reconstructed a cross section (Figure 5.4A) to view the internal structuring of the tip.

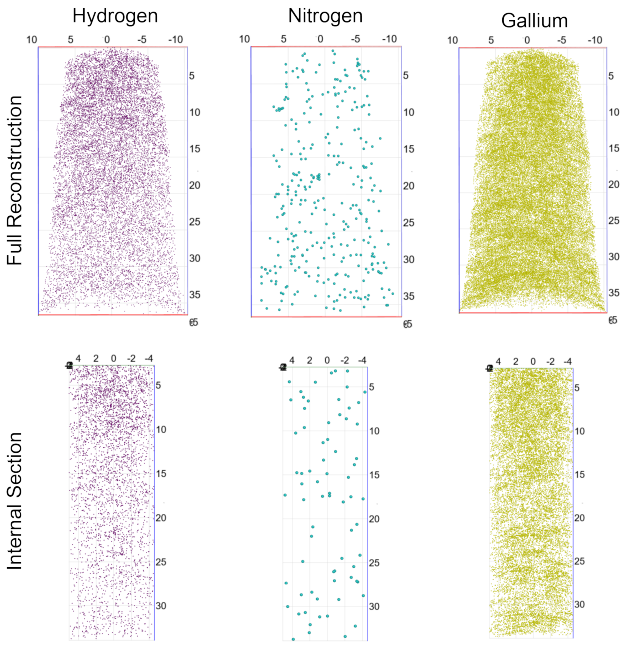

Figure 5.3: Distribution of hydrogen, nitrogen, and gallium ions within the tip. The distribution is shown both in the full reconstruction and in an internal section to show the effect of surface defects.

We did observe gallium implantation (Figure 5.4B) throughout the measured portion of the tip, signifying damage, however this was concentrated near the surface and decreased substantially toward the bulk diamond. By mapping the carbon, we were able to observe a greater degree of ordering away from the tip, signifying considerable damage at the tip but less as the run continues. This was correlated to TEM images of a similarly-prepared tip (figures 5.4D and E), which show a layer of about 10 nm of amorphized carbon atop a relatively crystalline tip, which correlates well to our APT data. Finally, we measured the distribution of all detected C_n counts, and found that for larger values of n, the ions were concentrated near the tip. This could be attributable to greater sample damage near the tip disrupting the diamond lattice and making it easier for larger molecular ions to break off.

One of the unique properties of diamond as a material is its superior thermal conductivity.[366] This allows for us to use much greater laser pulse energies than what would normally be tolerated in APT. The typical complication of overly high pulse energies in APT is thermal tailing of the mass spectrum, arising from the tip remaining above the critical temperature for field evaporation for a finite amount of time, resulting in an apparently longer time of flight.[187,365] Our experimental results show that, of all the challenges that do exist in APT of diamond, thermal tailing is not one of them. By considering the raw time of flight (TOF) data that corresponds to the $^{12}C^{1+}$ peak (i.e. the total amount of time in nanoseconds that $^{12}C^{1+}$ ions take to be measured) for a tip irradiated at 200 pJ, we can measure a full width at half maximum (FWHM) of 3.6 nanoseconds (Figure 5.5A). We can then use

the methods established in Roder et al.[187] to model the heat profile of the tip over time (Figure 5.5B) to determine how quickly the tip cools down following the laser pulse (using a base temperature of 41 K), and we found that in just 36 picoseconds (1% of the FWHM of the TOF), even tips irradiated at 500 pJ will have already cooled below liquid nitrogen temperatures, indicating that thermal effects will not significantly broaden the TOF spectrum. By comparison, the silicon tips modeled by Roder et al. took on the order of nanoseconds to hundreds of nanoseconds to cool to the same temperatures at pulse energies an order of magnitude lower than what we used.[187] Furthermore, it's worth noting that we calculate the temperature at the tip to only reach about 200K when irradiated at 500 pJ, which is nearly an order of magnitude below the temperatures at which we would be concerned about the graphitization of diamond.[372] The results of this modeling are confirmed with experimental data showing the normalized $^{12}C^{1+}$ peaks of tips irradiated at 200 and 500 pJ, respectively (Figure 5.5C). The peak profiles for both are functionally identical with no evidence of thermal tailing. This serves to emphasize some potential areas where diamond may be particularly suited for APT applications. Firstly, "extreme" APT is a technique that uses laser pulses in the extreme UV region (29.6 nm), which is far more efficient at thermally exciting materials.[373] This technique seems particularly well-suited to the measurement of diamond, as a material that requires a high proportion of thermal excitation for APT measurement and one that is

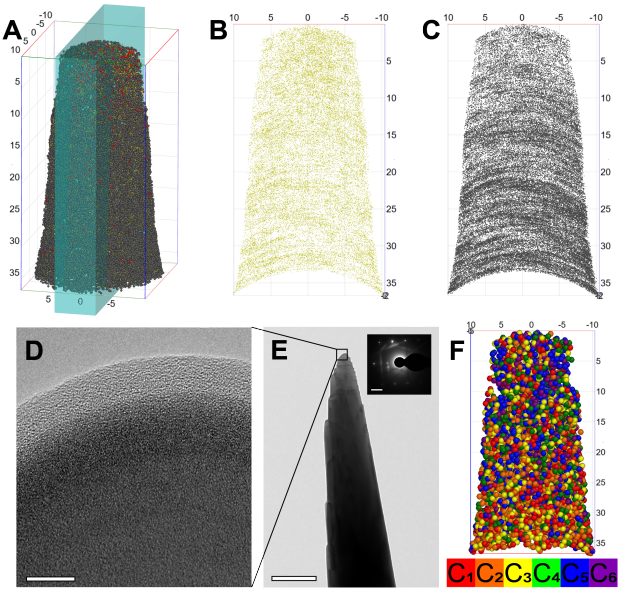

Figure 5.4: FIB damage of the diamond tip. (A) Visualization of cross section in (B) and (C). (B) Gallium reconstruction showing implantation throughout the lattice, concentrated near the tip. (C) Carbon reconstruction showing a decrease in order near the tip. (D) TEM of a diamond tip showing amorphous layer of ~10 nm (scale bar = 10 nm). (E) Image of the same tip (scale bar = 500 nm) inset diffraction of bulk tip (scale bar = 5 nm^{-1}). (F) Reconstruction showing 1000 counts of each carbon cluster (438 counts of C_6) showing a higher concentration of larger clusters near the tip

not significantly affected by thermal tailing. This also suggests the potential use of diamond as a material for APT sample mounts. The best sample mount is one that doesn't interfere with the measurement of the sample, and thus it can be concluded that a mount should ideally have a higher evaporation field than the sample so that it doesn't create background evaporation, and it should have a higher thermal conductivity so that it doesn't overheat and instead can act as a heat sink for the tip. In fact, some of the tips measured here may have failed due to the overheating and subsequent melting of the silicon sample mounts (as shown in the introduction in Figure 1.13), and this could have been mitigated by using a more thermally conductive sample mount, such as diamond. Of course the electrical nonconductivity of diamond would present a problem, but this is easily resolved by using boron-doped diamond, which is conductive.

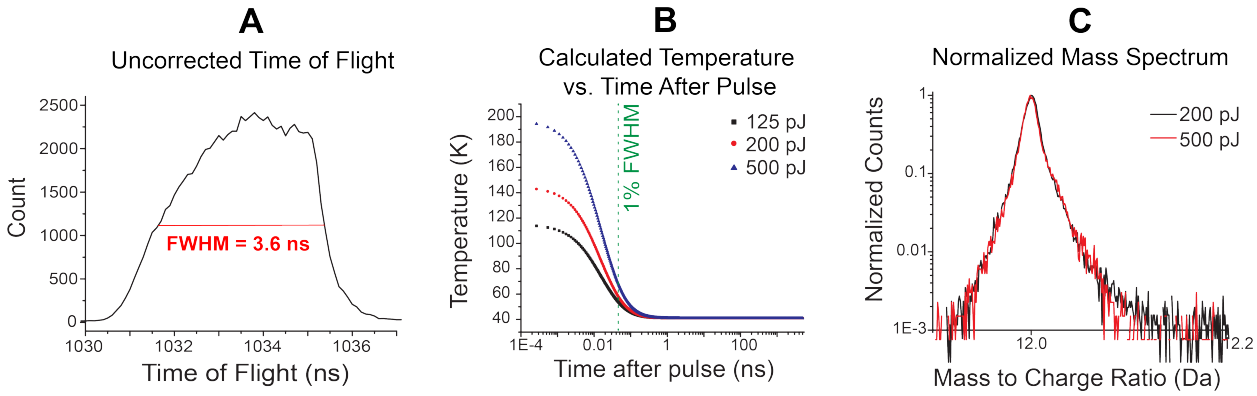

Figure 5.5: (A) Raw time of flight spectrum centered on the $^{12}C^{1+}$ peak, showing a full width at half maximum of 3.6 ns. (B) Heat transfer calculations showing the cooling of a diamond tip with a base temperature of 41 K that has been irradiated at various laser pulse energies. At 1% of the FWHM of the TOF spectrum of $^{12}C^{1+}$, the tip will have cooled to 57.5 K if irradiated at 125 pJ, 63.4 K if irradiated at 200 pJ, and 75.8 K if irradiated at 500 pJ, suggesting that the thermal broadening effect for diamond is negligible at operating laser pulse energies. (C) Normalized mass spectra for diamond tips irradiated at 200 and 500 pJ, showing no observable thermal broadening effect. Heat transfer calculations performed by Greg Felsted.

5.3 Conclusion

Here we show a hybrid method for producing APT tips of diamond using a combination of reactive ion etching and FIB. This significantly reduces the interaction of the sample with the ion beam, theoretically reducing damage. It also allows for more flexibility in terms of methods for tip sharpening that may in the future be able to reduce damage even further. We were able to collect APT data on these tips, detecting significant hydrogen and nitrogen, showing APT to be a useful method for detecting and mapping out these point defects in diamond. We were also able to characterize the damage from the FIB and both show that the damage is reduced past the tip and we were able to highlight some areas in which to improve future tip fabrication. Finally, we were able to show both computationally and experimentally that the the thermal conductivity of diamond allows for very high laser pulse energies to be used to thermally excite the tips in APT, thus reducing the operating voltage, without negatively affecting the mass spectrum, which suggests that diamond would be a good candidate for "extreme" APT measurements, and further suggests that diamond would be a near-optimal material for APT sample mounting posts.

Chapter 6

CONCLUSION

Perhaps the most frustrating but also the most rewarding aspect of science is that most of the time, when you answer one question, the process of doing so nucleates many new questions that need to be answered. The more you know, the more you realize that you don't know. This has certainly been exemplified in the research presented in this dissertation. One paper about NaYF crystal growth became three with even more in earlier stages of development, aiming to answer questions we never would have thought to ask at the beginning of this process. What was meant to be a simple APT measurement of diamond created many new questions about how best to address APT measurements of diamond in general, and what uses diamond may have within the APT community. This particular property of science also makes it deviously difficult to conclude such a dissertation, because I leave with the knowledge that there is so much left to learn about the topics that I have spent so long studying. Along those lines, I would like to use this space to summarize not just the questions that we've answered, but also the questions that we've created in the process. It is my hope that some time in the future somebody can read this dissertation and then go and try to answer these lingering questions, and a little further in the future I can read this dissertation and find that these questions have been answered and even more questions have been generated in the process.

The majority of my work here focused on the NaYF project. When I started working on NaYF, we viewed it predominantly as a means to an end and, while we had some interest in adjusting the morphology of the particles to suit our needs, we had not given much thought to how they form in solution. Our first foray into that topic revealed in Chapter 2 a phase conversion mechanism in the hydrothermal synthesis that was mediated by the formation

of mesocrystals of the initial cubic phase that then undergo oriented attachment to form a particle large enough to be thermodynamically driven to undergo a phase conversion to the hexagonal phase. Studying this process led us to wonder how the cubic particles initially form, which we studied in depth in Chapter 3. We found that an initial amorphous YF_3 phase separates from solution via spinodal decomposition into a gel phase, and then solid state diffusion of the remaining NaF in solution allows crystals to nucleate within that gel. The study of this question led us to confirm our suspicions that the often-reported cubic phase of YF_3 is not stable and that it likely has been reported in error in most if not all cases. Given this realization that we cannot make cubic YF_3, this led us to ask what happens if there isn't enough NaF in solution to nucleate NaYF crystals. We address this question in Chapter 4, where we find that in those cases, the gel will initially form but then will redissolve into various YF_n species in solution, which eventually nucleate orthorhombic YF_3. Initially we assumed that the YF_3 nucleation was more or less a classical process, but DLS data suggest that this YF_3 nucleation and growth may occur at least partially via particle assembly. Perhaps the most consequential conclusion we have from this study is the understanding that the aqueous NaYF-YF_3 system relies on a "switch" based on the initial concentration that determines the composition and crystal phase of the final particles via a mechanism that fundamentally intertwines chemistry and crystal growth and which can only be understood by viewing them both as dynamic processes that affect and are affected by each other.

All these results, of course, leave us with even more questions. Starting in Chapter 2, one question which has long plagued us is to what degree the mesocrystal intermediate is preserved in the final hexagonal particle. By using heterogeneously-doped particles, we have shown some degree of concentration fluctuation in the final particle indicating that there may be some preservation of the structure of the mesocrystals, but a detailed tomographic study would help us to understand the degree to which that structure is preserved, which could have applications, for example, in nano-barcoding, in which fine structure is a requirement. Another question that remains from that study is the degree to which the microemulsion solvent system affects the initial nucleation. We do not anticipate that YF_3 is any more

soluble in that system than it is in water, and we have shown that the same liquid-liquid phase separation occurs in a mixture of water and ethanol, so we would expect that it would also occur in this microemulsion (which itself forms from a liquid-liquid phase separation), however it may be constrained by the microemulsion itself, perhaps with the inclusions in the microemulsion acting as a sort of "nano-reactor." We have done some preliminary cryo-TEM on that system, however we did not appreciate the intricacy of the nucleation mechanism at that time, and it would be useful to revisit those experiments in light of what we now know to see if we can observe the initial stages of nucleation in that more complex system. Regarding the nucleation itself that we described in Chapter 3, we have some preliminary computational data showing the ion pairing that may underlie the liquid-liquid phase separation process, and this could be developed into a full computational model that demonstrates the entire process from the initial separation of YF_3 to the eventual nucleation of NaYF. We also showed computationally that the often-reported cubic YF_3 structure is not stable, however we have yet to determine whether or not there is some other cubic phase that may be stable, and if there is, whether we can produce it experimentally. There are also remaining questions regarding the incorporation of sodium into the solid phase, initiating the nucleation. This is begging to be studied with cryo-APT. Cryo-APT would allow us to set a time point in the reaction very precisely and measure the amount of sodium not only in the solid phase but also remaining in the supernatant, thus directly showing the diffusion process. I can think of no other technique that is better suited to answer this question, and I truly hope that somebody tries that someday. Finally, with respect to Chapter 4, by the nature of this paper being a work in progress, this has the most remaining questions, most of which have been addressed in the chapter itself, but briefly, we still need conventional and cryo-TEM data to characterize the growth process of YF_3. Cryo-TEM is needed in the early stages to understand the dissolution of the gel, and TEM is needed at later time points to understand the perhaps non-classical elements of the YF_3 growth process, as suggested by our DLS data. Additionally, with regards to the "switch" mechanism, we need to consider the ratios between 3:1 (stoichiometric to YF_3) and 4:1 (stoichiometric to $NaYF_4$) to understand whether the

crossover occurs at a specific point or whether there is a region in which both phases can form, or perhaps some other phase that we hadn't thought of. Altogether, we see that as we have learned about the NaYF-YF_3 system, we have found that it is far more complicated than anyone ever would have imagined, and I am optimistic that the trove of possibilities within that system will motivate research for many years after I have moved on.

Not to be forgotten, the diamond APT paper in Chapter 5 allowed us to examine diamond on the near-atomic scale and potentially map out nitrogen color centers as well as residual hydrogen from the CVD process, which is difficult with other techniques. We also found that by using reactive ion etching we can drastically reduce the time and beam interaction required for the final sample mounting before APT, potentially reducing sample damage. Finally, we found that with laser pulse energies even an order of magnitude higher than what are typically used in APT, the thermal tailing effect is negligible due to diamond's excellent thermal conductivity, suggesting that the key to successful APT measurement of diamond is to drastically increase the thermal contribution in the field evaporation process. This suggests that diamond may be particularly well-suited for use as an APT mount due to its low evaporation field and high thermal conductivity, allowing it to behave as a heat sink for the tip and produce virtually no background. The remaining questions regarding diamond APT follow from this. The technique of "extreme APT" uses a laser pulse in the extreme UV to increase the proportion of the laser pulse that is converted to heat, which will in turn allow for a much higher proportion of the field evaporation to come from thermal contributions. This technique is particularly useful for materials that have a high evaporation field and low thermal tailing, and diamond exceeds in both of those properties. As a result, extreme APT is liable to vastly improve the quality of APT data that we can collect on diamond. We also would like to further develop this idea of diamond sample mounts for APT. Sample mounts that have a lower evaporation field than the sample are liable to produce background, and mounts that have a lower thermal conductivity than the sample are liable to store heat and potentially suffer thermal damage, as what likely occurred with some of the sample mounts we used with diamond, for example as shown in Figure 1.13 in the introduction.

Using diamond as a sample mount would virtually eliminate both of these problems. As such, the further study of these sample mounts is needed, and in doing so we may identify some further strengths as well as unforeseen challenges that need to be addressed.

One philosophy that has guided me as a scientist is the concept that we study these systems because they are interesting, not because they are easy to study with any particular technique. This attitude has surely meant that we have had to work harder to get answers and that the systems we work with are often messy and difficult to parse. But in my view, the most interesting questions are often found by unraveling these messy systems and banging our heads against difficult experiments to figure out how to get them to work. My hope in writing this dissertation is that it conveys not only the duty we have as scientists to try to tackle these challenges but also the great insights we can gain from trying to crack them. In the famous words of John F. Kennedy, "Why climb the highest mountain? ... Why does Rice play Texas?* ... We choose to go to the moon in this decade and do these other things not because they are easy, but because they are hard."[374]

*At the time of Kennedy's 1962 speech, Rice football had a record of 19-29 against Texas. Since then, they have a record of 2-46-1 as of September 2023. Hook 'em!

"But I am very poorly today & very stupid & hate everybody & everything. One lives only to make blunders. I am going to write a little Book for Murray on orchids & today I hate them worse than everything so farewell & in a sweet frame of mind, I am"

-C. Darwin, Oct. 1861

Letter to C. Lyell[375]

BIBLIOGRAPHY

(1) Bard, A. B.; Zhou, X.; Xia, X.; Zhu, G.; Lim, M. B.; Kim, S. M.; Johnson, M. C.; Kollman, J. M.; Marcus, M. A.; Spurgeon, S. R.; Perea, D. E.; Devaraj, A.; Chun, J.; De Yoreo, J. J.; Pauzauskie, P. J. A Mechanistic Understanding of Nonclassical Crystal Growth in Hydrothermally Synthesized Sodium Yttrium Fluoride Nanowires. *Chemistry of Materials* **2020**, *32*, 2753–2763, DOI: 10.1021/acs.chemmater.9b04076.

(2) Bard, A. B. et al. Chemically-Driven Multi-Step Crystallization in the Synthesis of Sodium Yttrium Fluoride Via a Porous, Electrochemically-Active Intermediate. *In Submission* **2023**.

(3) Bard, A. B.; Chen, Y.; LaCount, M. D.; Mundy, C. J.; Schenter, G. K.; Liu, J. I.; De Yoreo, J. J.; Pauzauskie, P. J. Concentration-Selective Nucleation "Switch" in the YF_3-$NaYF_4$ System. *In Preparation* **2023**.

(4) Bard, A. B.; Felsted, R. G.; Stöhr, R.; Wrachtrup, J.; Spurgeon, S. R.; Perea, D. E.; Pauzauskie, P. J. Microfabrication from Bulk and Measurement of Nanoscale Diamond Tips for Atom Probe Tomography. *In Preparation* **2023**.

(5) Oxtoby, D. W.; Kashchiev, D. A general relation between the nucleation work and the size of the nucleus in multicomponent nucleation. *The Journal of Chemical Physics* **1994**, *100*, 7665–7671, DOI: 10.1063/1.466859.

(6) Kashchiev, D. Multicomponent nucleation: Thermodynamically consistent description of the nucleation work. *The Journal of Chemical Physics* **2004**, *120*, 3749–3758, DOI: 10.1063/1.1643711.

(7) Kennedy, G. M.; Kenyon, S. J. Planet Formation around Stars of Various Masses: The Snow Line and the Frequency of Giant Planets. *The Astrophysical Journal* **2008**, *673*, 502–512, DOI: 10.1086/524130.

(8) Bonucci, E. Bone mineralization. *Frontiers in Bioscience* **2012**, *17*, 100, DOI: 10.2741/3918.

(9) Fox, P. F.; McSweeney, P. L. H.; Cogan, T. M.; Guinee, T. P., *Cheese: Chemistry, Physics and Microbiology*; Elsevier: 2004; Vol. 1.

(10) Schenk, H.; Peschar, R. Understanding the structure of chocolate. *Radiation Physics and Chemistry* **2004**, *71*, 829–835, DOI: 10.1016/J.RADPHYSCHEM.2004.04.105.

(11) Goodenough, C. Immaterials and Methods: Reagents for the Total Laboratory Synthesis of the Chocolate Chip Cookie. *Journal of Immaterial Science* **2022**, *2*, 67–68.

(12) Kepler, J., *A New Year's Gift or On the Six-Cornered Snowflake*; Godfrey Tampach: 1611.

(13) Khan, S. R.; Pearle, M. S.; Robertson, W. G.; Gambaro, G.; Canales, B. K.; Doizi, S.; Traxer, O.; Tiselius, H.-G. Kidney stones. *Nature Reviews Disease Primers* **2016**, *2*, 16008, DOI: 10.1038/nrdp.2016.8.

(14) Xiao, H.; Jia, X.; Ma, H.; Li, S.; Li, Y.; Zhao, M. Synthesis of high quality type-Ib diamond crystals in carats grade. *Chinese Science Bulletin* **2010**, *55*, 1372–1375, DOI: 10.1007/s11434-010-0108-4.

(15) Prozorov, T. Magnetic microbes: Bacterial magnetite biomineralization. *Seminars in Cell & Developmental Biology* **2015**, *46*, 36–43, DOI: 10.1016/J.SEMCDB.2015.09.003.

(16) Hartel, R. W.; von Elbe, J. H.; Hofberger, R. In; Springer International Publishing: 2018, pp 211–244, DOI: 10.1007/978-3-319-61742-8_8.

(17) Schmelzer, J. W. P.; Boltachev, G. S.; Baidakov, V. G. Classical and generalized Gibbs' approaches and the work of critical cluster formation in nucleation theory. *The Journal of Chemical Physics* **2006**, *124*, 194503, DOI: 10.1063/1.2196412.

(18) Oxtoby, D. W. Homogeneous nucleation: theory and experiment. *Journal of Physics: Condensed Matter* **1992**, *4*, 7627–7650, DOI: 10.1088/0953-8984/4/38/001.

(19) De Yoreo, J. J.; Vekilov, P. G. In; De Gruyter: 2003, pp 57–94, DOI: 10.1515/9781501509346-008.

(20) Voorhees, P. W. The theory of Ostwald ripening. *Journal of Statistical Physics* **1985**, *38*, 231–252, DOI: 10.1007/BF01017860.

(21) Ostwald, W. Studien über die Bildung und Umwandlung fester Körper. 1. Abhandlung: Übersättigung und Überkaltung. *Zeitschrift für Physikalische Chemie* **1897**, *22*, 289–330.

(22) Jin, B.; Liu, Z.; Tang, R. Recent experimental explorations of non-classical nucleation. *CrystEngComm* **2020**, *22*, 4057–4073, DOI: 10.1039/D0CE00480D.

(23) Hodgson, A. W. Homogeneous nucleation. *Advances in Colloid and Interface Science* **1984**, *21*, 303–327, DOI: 10.1016/0001-8686(84)85003-4.

(24) Gebauer, D.; Kellermeier, M.; Gale, J. D.; Bergström, L.; Cölfen, H. Pre-nucleation clusters as solute precursors in crystallisation. *Chem. Soc. Rev.* **2014**, *43*, 2348–2371, DOI: 10.1039/C3CS60451A.

(25) Jin, B.; Chen, Y.; Tao, J.; Lachowski, K. J.; Bowden, M. E.; Zhang, Z.; Pozzo, L. D.; Washton, N. M.; Mueller, K. T.; De Yoreo, J. J. Multi-Step Nucleation of a Crystalline Silicate Framework via a Structurally Precise Prenucleation Cluster. *Angewandte Chemie International Edition* **2023**, *62*, e202303770, DOI: https://doi.org/10.1002/anie.202303770.

(26) Gebauer, D.; Völkel, A.; Cölfen, H. Stable Prenucleation Calcium Carbonate Clusters. *Science* **2008**, *322*, 1819–1822, DOI: 10.1126/science.1164271.

(27) Dey, A.; Bomans, P. H. H.; Müller, F. A.; Will, J.; Frederik, P. M.; de With, G.; Sommerdijk, N. A. J. M. The role of prenucleation clusters in surface-induced calcium phosphate crystallization. *Nature Materials* **2010**, *9*, 1010–1014, DOI: 10.1038/nmat2900.

(28) Cossairt, B. M.; Owen, J. S. CdSe Clusters: At the Interface of Small Molecules and Quantum Dots. *Chemistry of Materials* **2011**, *23*, 3114–3119, DOI: 10.1021/cm2008686.

(29) Gary, D. C.; Terban, M. W.; Billinge, S. J. L.; Cossairt, B. M. Two-Step Nucleation and Growth of InP Quantum Dots via Magic-Sized Cluster Intermediates. *Chemistry of Materials* **2015**, *27*, 1432–1441, DOI: 10.1021/acs.chemmater.5b00286.

(30) Vekilov, P. G. The two-step mechanism of nucleation of crystals in solution. *Nanoscale* **2010**, *2*, 2346, DOI: 10.1039/c0nr00628a.

(31) Vorontsova, M. A.; Maes, D.; Vekilov, P. G. Recent advances in the understanding of two-step nucleation of protein crystals. *Faraday Discussions* **2015**, *179*, 27–40, DOI: 10.1039/C4FD00217B.

(32) Sauter, A.; Roosen-Runge, F.; Zhang, F.; Lotze, G.; Feoktystov, A.; Jacobs, R. M. J.; Schreiber, F. On the question of two-step nucleation in protein crystallization. *Faraday Discussions* **2015**, *179*, 41–58, DOI: 10.1039/C4FD00225C.

(33) Krautwurst, N.; Nicoleau, L.; Dietzsch, M.; Lieberwirth, I.; Labbez, C.; Fernandez-Martinez, A.; Driessche, A. E. S. V.; Barton, B.; Leukel, S.; Tremel, W. Two-Step Nucleation Process of Calcium Silicate Hydrate, the Nanobrick of Cement. *Chemistry of Materials* **2018**, *30*, 2895–2904, DOI: 10.1021/acs.chemmater.7b04245.

(34) Bruno, M. A two-step nucleation model based on diffuse interface theory (DIT) to explain the non-classical view of calcium carbonate polymorph formation. *CrystEngComm* **2019**, *21*, 4918–4924, DOI: 10.1039/C9CE00610A.

(35) Myerson, A. S.; Trout, B. L. Nucleation from Solution.*Science* **2013**, *341*, 855–856, DOI: 10.1126/science.1243022.

(36) Fei, L.; Gan, X.; Ng, S. M.; Wang, H.; Xu, M.; Lu, W.; Zhou, Y.; Leung, C. W.; Mak, C.-L.; Wang, Y. Observable Two-Step Nucleation Mechanism in Solid-State Formation of Tungsten Carbide.*ACS Nano* **2019**, *13*, 681–688, DOI: 10.1021/acsnano.8b07864.

(37) Yang, S.; Guo, Z.; Bian, B.; Du, J.; Hu, Y. Dynamic Observation of Anisotropic Chainlike Structures during Nonclassical Two-Step Nucleation in Solid-State Iron Oxide Crystallization.*The Journal of Physical Chemistry Letters* **2022**, *13*, 8352–8358, DOI: 10.1021/acs.jpclett.2c00855.

(38) Jiang, H.; Debenedetti, P. G.; Panagiotopoulos, A. Z. Nucleation in Aqueous NaCl Solutions Shifts from 1-step to 2-step Mechanism on Crossing the Spinodal.*The Journal of Chemical Physics* **2019**, *150*, 124502, DOI: 10.1063/1.5084248.

(39) Chang, Y. C.; Myerson, A. S. The diffusivity of potassium chloride and sodium chloride in concentrated, saturated, and supersaturated aqueous solutions.*AIChE Journal* **1985**, *31*, 890–894, DOI: 10.1002/aic.690310603.

(40) De Yoreo, J. J.; Gilbert, P. U. P. A.; Sommerdijk, N. A. J. M.; Penn, R. L.; Whitelam, S.; Joester, D.; Zhang, H.; Rimer, J. D.; Navrotsky, A.; Banfield, J. F.; Wallace, A. F.; Michel, F. M.; Meldrum, F. C.; Cölfen, H.; Dove, P. M. Crystallization by particle attachment in synthetic, biogenic, and geologic environments.*Science* **2015**, *349*, DOI: 10.1126/science.aaa6760.

(41) Han, T. Y.-J.; Aizenberg, J. Calcium Carbonate Storage in Amorphous Form and Its Template-Induced Crystallization.*Chemistry of Materials* **2008**, *20*, 1064–1068, DOI: 10.1021/cm702032v.

(42) Henzler, K.; Fetisov, E. O.; Galib, M.; Baer, M. D.; Legg, B. A.; Borca, C.; Xto, J. M.; Pin, S.; Fulton, J. L.; Schenter, G. K.; Govind, N.; Siepmann, J. I.; Mundy,

C. J.; Huthwelker, T.; Yoreo, J. J. D. Supersaturated calcium carbonate solutions are classical.*Science Advances* **2018**, *4*, eaao6283, DOI: 10.1126/sciadv.aao6283.

(43) Cahn, J. W.; Hilliard, J. E. Free Energy of a Nonuniform System. I. Interfacial Free Energy.*The Journal of Chemical Physics* **1958**, *28*, 258–267, DOI: 10.1063/1.1744102.

(44) Binder, K.; Fratzl, P. In; Wiley-VCH Verlag GmbH & Co. KGaA: 2005, pp 409–480, DOI: 10.1002/352760264X.ch6.

(45) Mitra, M. K.; Muthukumar, M. Theory of spinodal decomposition assisted crystallization in binary mixtures.*The Journal of Chemical Physics* **2010**, *132*, 184908, DOI: 10.1063/1.3425774.

(46) Ivanov, V. K.; Fedorov, P. P.; Ye Baranchikov, A.; Osiko, V. V. Oriented Attachment of Particles: 100 Years of Investigations of Non-Classical Crystal Growth.*Russian Chemical Reviews* **2014**, *83*, 1204–1222, DOI: 10.1070/RCR4453.

(47) Niederberger, M.; Cölfen, H. Oriented Attachment and Mesocrystals: Non-Classical Crystallization Mechanisms Based on Nanoparticle Assembly, 2006, DOI: 10.1039/b604589h.

(48) Bahrig, L.; Hickey, S. G.; Eychmüller, A. Mesocrystalline materials and the involvement of oriented attachment – a review.*CrystEngComm* **2014**, *16*, 9408–9424, DOI: 10.1039/C4CE00882K.

(49) Penn, J. M.; Banfield, A.; Perrotta, A. J.; Navrotsky, A.; Penn, R. L. Imperfect Oriented Attachment: Dislocation Generation in Defect-Free Nanocrystals.*Science (New York, N.Y.)* **1998**, *281*, 969–71, DOI: 10.1126/science.281.5379.969.

(50) Penn, R. L.; Tanaka, K.; Erbs, J. Size dependent kinetics of oriented aggregation.*Journal of Crystal Growth* **2007**, *309*, 97–102, DOI: 10.1016/j.jcrysgro.2007.09.011.

(51) Xue, X.; Penn, R. L.; Leite, E. R.; Huang, F.; Lin, Z. Crystal growth by oriented attachment: kinetic models and control factors. *CrystEngComm* **2014**, *16*, 1419, DOI: 10.1039/c3ce42129e.

(52) Sturm, E. V.; Cölfen, H. Mesocrystals: structural and morphogenetic aspects. *Chemical Society Reviews* **2016**, *45*, 5821–5833, DOI: 10.1039/C6CS00208K.

(53) Li, D.; Nielsen, M. H.; Lee, J. R. I.; Frandsen, C.; Banfield, J. F.; De Yoreo, J. J. Direction-Specific Interactions Control Crystal Growth by Oriented Attachment. *Science* **2012**, *336*, 1014–1018, DOI: 10.1126/science.1219643.

(54) Zhu, G.; Reiner, H.; Cölfen, H.; De Yoreo, J. J. Addressing some of the technical challenges associated with liquid phase S/TEM studies of particle nucleation, growth and assembly. *Micron* **2019**, *118*, 35–42, DOI: 10.1016/j.micron.2018.12.001.

(55) Sturm, E. V.; Colfen, H. Mesocrystals: Past, Presence, Future. *Crystals* **2017**, *7*, 207, DOI: 10.3390/cryst7070207.

(56) Zhou, L.; Smyth-Boyle, D.; O'Brien, P. A Facile Synthesis of Uniform NH_4TiOF_3 Mesocrystals and Their Conversion to TiO_2 Mesocrystals. *Journal of the American Chemical Society* **2008**, *130*, 1309–1320, DOI: 10.1021/ja076187c.

(57) Cölfen, H.; Mann, S. Higher-Order Organization by Mesoscale Self-Assembly and Transformation of Hybrid Nanostructures. *Angewandte Chemie International Edition* **2003**, *42*, 2350–2365, DOI: 10.1002/anie.200200562.

(58) Da Silva, R. O.; Gonçalves, R. H.; Stroppa, D. G.; Ramirez, A. J.; Leite, E. R. Synthesis of recrystallized anatase TiO_2 mesocrystals with Wulff shape assisted by oriented attachment. *Nanoscale* **2011**, *3*, 1910, DOI: 10.1039/c0nr01016b.

(59) Liu, Y.; Bai, J.; Ma, X.; Li, J.; Xiong, S. Formation of quasi-mesocrystal $ZnMn_2O_4$ twin microspheres via an oriented attachment for lithium-ion batteries. *J. Mater. Chem. A* **2014**, *2*, 14236–14244, DOI: 10.1039/C4TA02950J.

(60) Embrechts, H. E.; Zhang, S.; Hock, R.; Peukert, W.; Distaso, M. Observing Oriented Attachment during Mesocrystal Growth with *in Situ* Dynamic Light Scattering (DLS).*Crystal Growth & Design* **2020**, *20*, 1266–1275, DOI: 10.1021/acs.cgd.9b01523.

(61) Hong, Z.; Wei, M.; Lan, T.; Jiang, L.; Cao, G. Additive-free synthesis of unique TiO_2 mesocrystals with enhanced lithium-ion intercalation properties.*Energy Environ. Sci.* **2012**, *5*, 5408–5413, DOI: 10.1039/C1EE02551A.

(62) Driessche, A. E. S. V.; Gerven, N. V.; Joosten, R. R. M.; Ling, W. L.; Bacia, M.; Sommerdijk, N.; Sleutel, M. Nucleation of protein mesocrystals via oriented attachment.*Nature Communications* **2021**, *12*, 3902, DOI: 10.1038/s41467-021-24171-z.

(63) Zhou, G.-T.; Yao, Q.-Z.; Ni, J.; Jin, G. Formation of aragonite mesocrystals and implication for biomineralization.*American Mineralogist* **2009**, *94*, 293–302, DOI: 10.2138/am.2009.2957.

(64) Rao, A.; Roncal-Herrero, T.; Schmid, E.; Drechsler, M.; Scheffner, M.; Gebauer, D.; Kröger, R.; Cölfen, H. On Biomineralization: Enzymes Switch on Mesocrystal Assembly.*ACS Central Science* **2019**, *5*, 357–364, DOI: 10.1021/acscentsci.8b00853.

(65) Wang, T. et al. Mesocrystalline Ordering and Phase Transformation of Iron Oxide Biominerals in the Ultrahard Teeth of *Cryptochiton stelleri*.*Small Structures* **2022**, *3*, 2100202, DOI: 10.1002/sstr.202100202.

(66) Rao, A.; Cölfen, H. In; Springer International Publishing: 2017, pp 155–183, DOI: 10.1007/978-3-319-45669-0_8.

(67) Zhong, Y.; Allen, V. R.; Chen, J.; Wang, Y.; Ye, X. Multistep Crystallization of Dynamic Nanoparticle Superlattices in Nonaqueous Solutions.*Journal of the American Chemical Society* **2022**, *144*, 14915–14922, DOI: 10.1021/jacs.2c06535.

(68) Wang, Y.; Chen, J.; Zhu, C.; Zhu, B.; Jeong, S.; Yi, Y.; Liu, Y.; Fiadorwu, J.; He, P.; Ye, X. Kinetically Controlled Self-Assembly of Binary Polymer-Grafted Nanocrystals into Ordered Superstructures via Solvent Vapor Annealing.*Nano Letters* **2021**, *21*, 5053–5059, DOI: 10.1021/acs.nanolett.1c00890.

(69) Haase, M.; Schäfer, H. Upconverting Nanoparticles.*Angewandte Chemie International Edition* **2011**, *50*, 5808–5829, DOI: 10.1002/anie.201005159.

(70) DaCosta, M. V.; Doughan, S.; Han, Y.; Krull, U. J. Lanthanide upconversion nanoparticles and applications in bioassays and bioimaging: A review.*Analytica Chimica Acta* **2014**, *832*, 1–33, DOI: 10.1016/j.aca.2014.04.030.

(71) Wang, X.; Chou, I.-M.; Hu, W.; Burruss, R. C. In situ observations of liquid–liquid phase separation in aqueous $MgSO_4$ solutions: Geological and geochemical implications.*Geochimica et Cosmochimica Acta* **2013**, *103*, 1–10, DOI: 10.1016/j.gca.2012.10.044.

(72) Zhong, Y.; Rostami, I.; Wang, Z.; Dai, H.; Hu, Z. Energy Migration Engineering of Bright Rare-Earth Upconversion Nanoparticles for Excitation by Light-Emitting Diodes.*Advanced Materials* **2015**, *27*, 6418–6422, DOI: 10.1002/adma.201502272.

(73) Ma, X.; Ni, X. Using upconversion nanoparticles to improve photovoltaic properties of poly(3-hexylthiophene)-TiO2 heterojunction solar cell.*Journal of Nanoparticle Research* **2013**, *15*, DOI: 10.1007/s11051-013-1547-z.

(74) Yu, J.; Yang, Y.; Fan, R.; Wang, P.; Dong, Y. Enhanced photovoltaic performance of dye-sensitized solar cells using a new photoelectrode material: Upconversion YbF_3-Ho/TiO_2 nanoheterostructures.*Nanoscale* **2016**, *8*, 4173–4180, DOI: 10.1039/c5nr08319b.

(75) Ma, X.; Ni, X. Fabrication of polythiophene–TiO_2 heterojunction solar cells coupled with upconversion nanoparticles.*Journal of Materials Science: Materials in Electronics* **2014**, *26*, 1129–1135, DOI: 10.1007/s10854-014-2516-8.

(76) You, M.; Lin, M.; Wang, S.; Wang, X.; Zhang, G.; Hong, Y.; Dong, Y.; Jin, G.; Xu, F. Three-dimensional quick response code based on inkjet printing of upconversion fluorescent nanoparticles for drug anti-counterfeiting.*Nanoscale* **2016**, *8*, 10096–10104, DOI: 10.1039/c6nr01353h.

(77) Kumar, P.; Singh, S.; Gupta, B. K. Future prospects of luminescent nanomaterial based security inks: From synthesis to anti-counterfeiting applications.**2016**, *8*, 14297–14340, DOI: 10.1039/c5nr06965c.

(78) Tan, H.; Gong, G.; Xie, S.; Song, Y.; Zhang, C.; Li, N.; Zhang, D.; Xu, L.; Xu, J.; Zheng, J. Upconversion Nanoparticles@Carbon Dots@Meso-SiO_2 Sandwiched Core–Shell Nanohybrids with Tunable Dual-Mode Luminescence for 3D Anti-Counterfeiting Barcodes.*Langmuir* **2019**, *35*, 11503–11511, DOI: 10.1021/acs.langmuir.9b01919.

(79) Qiao, B.; Pang, Q.; Yuan, P.; Luo, Y.; Ma, L. Smart wound dressing for infection monitoring and NIR-triggered antibacterial treatment.*Biomaterials Science* **2020**, *8*, 1649–1657, DOI: 10.1039/C9BM02060H.

(80) Rebelo, C.; Reis, T.; Guedes, J.; Saraiva, C.; Rodrigues, A. F.; Simões, S.; Bernardino, L.; Peça, J.; Pinho, S. L. C.; Ferreira, L. Efficient spatially targeted gene editing using a near-infrared activatable protein-conjugated nanoparticle for brain applications.*Nature Communications* **2022**, *13*, 4135, DOI: 10.1038/s41467-022-31791-6.

(81) Chen, S.; Wu, J.; Cai, A.; Gonzalez, N.; Yin, R. Towards minimally invasive deep brain stimulation and imaging: A near-infrared upconversion approach.*Neuroscience Research* **2020**, *152*, 59–65, DOI: 10.1016/j.neures.2020.01.005.

(82) Wang, M.; Li, M.; Yang, M.; Zhang, X.; Yu, A.; Zhu, Y.; Qiu, P.; Mao, C. NIR-induced highly sensitive detection of latent fingermarks by $NaYF_4$:Yb,Er upconversion nanoparticles in a dry powder state.*Nano Research* **2015**, *8*, 1800–1810, DOI: 10.1007/s12274-014-0686-6.

(83) Zhang, Y.; Zhang, L.; Deng, R.; Tian, J.; Zong, Y.; Jin, D.; Liu, X. Multicolor Barcoding in a Single Upconversion Crystal. *Journal of the American Chemical Society* **2014**, *136*, 4893–4896, DOI: 10.1021/ja5013646.

(84) Ma, Y.; Bao, J.; Zhang, Y.; Li, Z.; Zhou, X.; Wan, C.; Huang, L.; Zhao, Y.; Han, G.; Xue, T. Mammalian Near-Infrared Image Vision Through Injectable and Self-Powered Retinal Nanoantennae. *Cell* **2019**, *177*, DOI: 10.1016/j.cell.2019.01.038.

(85) Xu, E. Z.; Lee, C.; Pritzl, S. D.; Chen, A. S.; Lohmueller, T.; Cohen, B. E.; Chan, E. M.; Schuck, P. J. Infrared-to-ultraviolet upconverting nanoparticles for COVID-19-related disinfection applications. *Optical Materials: X* **2021**, *12*, 100099, DOI: 10.1016/j.omx.2021.100099.

(86) Roder, P. B.; Smith, B. E.; Zhou, X.; Crane, M. J.; Pauzauskie, P. J. Laser Refrigeration of Hydrothermal Nanocrystals in Physiological Media. *Proceedings of the National Academy of Sciences* **2015**, *112*, 15024–15029, DOI: 10.1073/pnas.1510418112.

(87) Zhong, B.; Luo, H.; Chen, L.; Shi, Y.; Yin, J. In *Proceedings of SPIE*, ed. by Epstein, R. I.; Seletskiy, D. V.; Sheik-Bahae, M., International Society for Optics and Photonics: 2016; Vol. 9765, p 976506, DOI: 10.1117/12.2213900.

(88) Luntz-Martin, D. R.; Felsted, R. G.; Dadras, S.; Pauzauskie, P. J.; Vamivakas, A. N. Laser refrigeration of optically levitated sodium yttrium fluoride nanocrystals. *Optics Letters* **2021**, *46*, 3797, DOI: 10.1364/OL.426334.

(89) Felsted, G.; Pant, A.; Bard, A. B.; Xia, X.; Luntz-Martin, D. R.; Dadras, S.; Zhang, S.; Vamivakas, N.; Pauzauskie, P. J. In *Photonic Heat Engines: Science and Applications IV*, ed. by Kuno, M. K.; Seletskiy, D. V., SPIE: 2022, p 18, DOI: 10.1117/12.2611615.

(90) Menyuk, N.; Dwight, K.; Pierce, J. $NaYF_4$:Yb,Er—an efficient upconversion phosphor. *Applied Physics Letters* **1972**, *21*, 159–161, DOI: 10.1063/1.1654325.

(91) Joubert, M.; Linarès, C.; Jacquier, B.; Cassanho, A.; Jenssen, H. A spectroscopic study of $NaYF_4$:Nd^{3+}.*Journal of Luminescence* **1992**, *51*, 175–187, DOI: 10.1016/0022-2313(92)90052-B.

(92) Thoma, R. E.; Insley, H.; Hebert, G. M. The Sodium Fluoride-Lanthanide Trifluoride Systems.*Inorganic Chemistry* **1966**, *5*, 1222–1229, DOI: 10.1021/ic50041a032.

(93) Thoma, R. E.; Hebert, G. M.; Insley, H.; Weaver, C. F. Equilibria in the System Sodium Fluoride-Yttrium Fluoride.*Inorganic Chemistry* **1963**, *2*, 1005–1012, DOI: 10.1021/ic50009a030.

(94) Roy, D. M.; Roy, R. Controlled Massively Defective Crystalline Solutions With the Fluorite Structure.*Journal of The Electrochemical Society* **1964**, *111*, 421, DOI: 10.1149/1.2426145.

(95) Fedorov, P. P. Systems of Alkali and Rare-Earth Metal Fluorides.*Russian Journal of Inorganic Chemistry* **1999**, *44*, 1792–1818.

(96) Fedorov, P.; Kuznetsov, S.; Osiko, V. In *Photonic and Electronic Properties of Fluoride Materials*; Elsevier: 2016, pp 7–31, DOI: 10.1016/B978-0-12-801639-8.00002-7.

(97) Grzechnik, A.; Bouvier, P.; Mezouar, M.; Mathews, M.; Tyagi, A.; Köhler, J. Hexagonal $Na_{1.5}Y_{1.5}F_6$ at High Pressures.*Journal of Solid State Chemistry* **2002**, *165*, 159–164, DOI: 10.1006/jssc.2001.9525.

(98) Tkachuk, A. M.; Ivanova, S. É.; Joubert, M. F.; Guyot, Y. Spectroscopic Study of Double Sodium-Yttrium Fluoride Crystals Doped with Erbium $Na_{0.4}Y_{0.6}F_{2.2}$:Er^{3+}: I. Intensities of Luminescence Spectra and Kinetics of Luminescence.*Optics and Spectroscopy* **2004**, *97*, 251–269, DOI: 10.1134/1.1790643.

(99) Fedorov, P. P. Comment on the paper A.B. Bard, X. Zue, G. Zhu, et al. "A Mechanistic Inderstanding of Non-Classical Crystal Growth in Hydrothermally Synthezied Sodium Yttrium Fluoride Nanowires".*Chemistry of Materials* **2020**.

(100) Ayers, M. A Nanoreview of Nanoscience.*Science & Technology Libraries* **2022**, *41*, 113–122, DOI: 10.1080/0194262X.2021.1965943.

(101) Li, C.; Yang, J.; Quan, Z.; Yang, P.; Kong, D.; Lin, J. Different Microstructures of β-$NaYF_4$ Fabricated by Hydrothermal Process: Effects of pH Values and Fluoride Sources.*Chemistry of Materials* **2007**, *19*, 4933–4942, DOI: 10.1021/cm071668g.

(102) Wang, X.; Zhuang, J.; Peng, Q.; Li, Y.; V, T. U. Hydrothermal Synthesis of Rare-Earth Fluoride Nanocrystals.*Inorganic Chemistry* **2006**, *45*, 6661–6665, DOI: 10.1021/ic051683s.

(103) Shan, J.; Qin, X.; Yao, N.; Ju, Y. Synthesis of monodisperse hexagonal $NaYF_4$:Yb, Ln (Ln = Er, Ho and Tm) upconversion nanocrystals in TOPO.*Nanotechnology* **2007**, *18*, 445607, DOI: 10.1088/0957-4484/18/44/445607.

(104) Fedorov, P. P.; Luginina, A. A.; Kuznetsov, S. V.; Osiko, V. V. Nanofluorides.*Journal of Fluorine Chemistry* **2011**, *132*, 1012–1039, DOI: 10.1016/j.jfluchem.2011.06.025.

(105) Shan, J.; Ju, Y. A single-step synthesis and the kinetic mechanism for monodisperse and hexagonal-phase $NaYF_4$:Yb, Er upconversion nanophosphors.*Nanotechnology* **2009**, *20*, 275603, DOI: 10.1088/0957-4484/20/27/275603.

(106) Yan, C.; Zhao, H.; Perepichka, D. F.; Rosei, F. Lanthanide Ion Doped Upconverting Nanoparticles: Synthesis, Structure and Properties.*Small* **2016**, *12*, 3888–3907, DOI: 10.1002/smll.201601565.

(107) Epstein, R. I.; Buchwald, M. I.; Edwards, B. C.; Gosnell, T. R.; Mungan, C. E. Observation of Laser-Induced fluorescent Cooling of a Solid.*Nature* **1995**, *377*, 500–503.

(108) Nemova, G.; Kashyap, R. Laser cooling of solids.*Reports on Progress in Physics* **2010**, *73*, 086501, DOI: 10.1088/0034-4885/73/8/086501.

(109) Bigotta, S.; Lieto, A. D.; Parisi, D.; Toncelli, A.; Tonelli, M. In, ed. by Epstein, R. I.; Sheik-Bahae, M., 2007, 64610E, DOI: 10.1117/12.701989.

(110) Hehlen, 2. P. In, ed. by Epstein, R. I.; Sheik-Bahae, M., 2010, p 761404, DOI: 10.1117/12.845626.

(111) Zhong, B.; Jia, Y.; Chen, L.; Deng, Y.; Chen, Y.; Yin, J. Cavity-enhanced laser cooling for Yb^{3+}-doped fluoride crystal using a low-power diode laser. *Journal of the Optical Society of America B* **2014**, *31*, 2116, DOI: 10.1364/JOSAB.31.002116.

(112) Bigotta, S.; Tonelli, M. In; Wiley-VCH Verlag GmbH & Co. KGaA, pp 75–95, DOI: 10.1002/9783527628049.ch3.

(113) Seletskiy, D. V.; Epstein, R.; Sheik-Bahae, M. Laser cooling in solids: advances and prospects. *Reports on Progress in Physics* **2016**, *79*, 096401, DOI: 10.1088/0034-4885/79/9/096401.

(114) Zhou, X.; Smith, B. E.; Roder, P. B.; Pauzauskie, P. J. Laser Refrigeration of Ytterbium-Doped Sodium-Yttrium-Fluoride Nanowires. *Advanced Materials* **2016**, *28*, 8658–8662, DOI: 10.1002/adma.201600406.

(115) Thomas, J.; Maia, L.; Ledemi, Y.; Messaddeq, Y.; Kashyap, R. In; Wiley: 2021, pp 353–396, DOI: 10.1002/9781119529538.ch10.

(116) Edwards, B. C.; Anderson, J. E.; Epstein, R. I.; Mills, G. L.; Mord, A. J. Demonstration of a solid-state optical cooler: An approach to cryogenic refrigeration. *Journal of Applied Physics* **1999**, *86*, 6489–6493, DOI: 10.1063/1.371713.

(117) Nemova, G. Laser Cooling and Trapping of Rare-Earth-Doped Particles. *Applied Sciences* **2022**, *12*, 3777, DOI: 10.3390/app12083777.

(118) Mi, C.; Zhou, J.; Wang, F.; Jin, D. Thermally enhanced NIR–NIR anti-Stokes emission in rare earth doped nanocrystals. *Nanoscale* **2019**, *11*, 12547–12552, DOI: 10.1039/C9NR03041G.

(119) Rahman, A. T. M. A.; Barker, P. F. Laser refrigeration, alignment and rotation of levitated Yb^{3+}:YLF nanocrystals. *Nature Photonics* **2017**, *11*, 634–638, DOI: 10.1038/s41566-017-0005-3.

(120) Fedorov, P. P.; Kuznetsov, S. V.; Voronov, V. V.; Yarotskaya, I. V.; Arbenina, V. V. Soft chemical synthesis of $NaYF_4$ nanopowders. *Russian Journal of Inorganic Chemistry* **2008**, *53*, 1681–1685, DOI: 10.1134/S0036023608110028.

(121) Silverman, J. 'Pics or it didn't happen' – the mantra of the Instagram era. *The Guardian* **2015**.

(122) Müller, E. W. Field Desorption. *Physical Review* **1956**, *102*, 618–624, DOI: 10.1103/PhysRev.102.618.

(123) Jacobsson, D.; Panciera, F.; Tersoff, J.; Reuter, M. C.; Lehmann, S.; Hofmann, S.; Dick, K. A.; Ross, F. M. Interface dynamics and crystal phase switching in GaAs nanowires. *Nature* **2016**, *531*, 317–322, DOI: 10.1038/nature17148.

(124) Ross, F. M. Controlling nanowire structures through real time growth studies. *Reports on Progress in Physics* **2010**, *73*, 114501, DOI: 10.1088/0034-4885/73/11/114501.

(125) De Jonge, N.; Ross, F. M. Electron microscopy of specimens in liquid. *Nature Nanotechnology* **2011**, *6*, 695–704, DOI: 10.1038/nnano.2011.161.

(126) Radisic, A.; Vereecken, P. M.; Hannon, J. B.; Searson, P. C.; Ross, F. M. Quantifying Electrochemical Nucleation and Growth of Nanoscale Clusters Using Real-Time Kinetic Data. *Nano Letters* **2006**, *6*, 238–242, DOI: 10.1021/nl052175i.

(127) Kodambaka, S.; Hannon, J. B.; Tromp, R. M.; Ross, F. M. Control of Si Nanowire Growth by Oxygen. *Nano Letters* **2006**, *6*, 1292–1296, DOI: 10.1021/nl060059p.

(128) Song, M.; Zhou, G.; Lu, N.; Lee, J.; Nakouzi, E.; Wang, H.; Li, D. Oriented attachment induces fivefold twins by forming and decomposing high-energy grain boundaries. *Science* **2020**, *367*, 40–45, DOI: 10.1126/science.aax6511.

(129) Anderson, D. 'Your most humble servant': the letters of Antony van Leeuwenhoek. *FEMS Microbiology Letters* **2022**, *369*, DOI: 10.1093/femsle/fnac007.

(130) Bard, A. J.; Fan, F. R. F.; Kwak, J.; Lev, O. Scanning electrochemical microscopy. Introduction and principles.*Analytical Chemistry* **1989**, *61*, 132–138, DOI: 10.1021/ac00177a011.

(131) Nakouzi, E.; Stack, A. G.; Kerisit, S.; Legg, B. A.; Mundy, C. J.; Schenter, G. K.; Chun, J.; De Yoreo, J. J. Moving beyond the Solvent-Tip Approximation to Determine Site-Specific Variations of Interfacial Water Structure through 3D Force Microscopy. *The Journal of Physical Chemistry C* **2021**, *125*, 1282–1291, DOI: 10.1021/acs.jpcc.0c07901.

(132) Tseng, A. A.; Notargiacomo, A.; Chen, T. P. Nanofabrication by scanning probe microscope lithography: A review.*Journal of Vacuum Science & Technology B: Microelectronics and Nanometer Structures* **2005**, *23*, 877, DOI: 10.1116/1.1926293.

(133) Legg, B. A.; Baer, M. D.; Chun, J.; Schenter, G. K.; Huang, S.; Zhang, Y.; Min, Y.; Mundy, C. J.; De Yoreo, J. J. Visualization of Aluminum Ions at the Mica Water Interface Links Hydrolysis State-to-Surface Potential and Particle Adhesion.*Journal of the American Chemical Society* **2020**, *142*, 6093–6102, DOI: 10.1021/jacs.9b12530.

(134) Ruska, E. The development of the electron microscope and of electron microscopy.*Reviews of Modern Physics* **1987**, *59*, 627–638, DOI: 10.1103/RevModPhys.59.627.

(135) von Borries, B.; Ruska, E. Die Abbildung durchstrahlter Folien im Elektronenmikroskop.*Zeitschrift für Physik* **1933**, *83*, 187–193, DOI: 10.1007/BF01331139.

(136) De Broglie, L. Waves and Quanta.*Nature* **1923**, *112*, 540–540, DOI: 10.1038/112540a0.

(137) Williams, D. B.; Carter, C. B. In *Transmission Electron Microscopy: A Textbook for Materials Science*, 2009, pp 11–14.

(138) Einstein, A. Ist die Trägheit eines Körpers von seinem Energieinhalt abhängig?*Annalen der Physik* **1905**, *323*, 639–641, DOI: 10.1002/andp.19053231314.

(139) Brooks, M. Spaceballs, 1987.

(140) Hetherington, C. Aberration correction for TEM. *Materials Today* **2004**, *7*, 50–55, DOI: 10.1016/S1369-7021(04)00571-1.

(141) Scherzer, O. Über einige Fehler von Elektronenlinsen. *Zeitschrift für Physik* **1936**, *101*, 593–603, DOI: 10.1007/BF01349606.

(142) Scherzer, O. The Theoretical Resolution Limit of the Electron Microscope. *Journal of Applied Physics* **1949**, *20*, 20–29, DOI: 10.1063/1.1698233.

(143) Rose, H. H. Historical aspects of aberration correction. *Journal of Electron Microscopy* **2009**, *58*, 77–85, DOI: 10.1093/jmicro/dfp012.

(144) Haider, M.; Rose, H.; Uhlemann, S.; Kabius, B.; Urban, K. Towards 0.1 nm resolution with the first spherically corrected transmission electron microscope. *Journal of Electron Microscopy* **1998**, *47*, 395–405, DOI: 10.1093/oxfordjournals.jmicro.a023610.

(145) Eckert, M. Max von Laue and the discovery of X-ray diffraction in 1912. *Annalen der Physik* **2012**, *524*, A83–A85, DOI: 10.1002/andp.201200724.

(146) Bragg, W. H.; Bragg, W. L. The reflection of X-rays by crystals. *Proceedings of the Royal Society of London. Series A, Containing Papers of a Mathematical and Physical Character* **1913**, *88*, 428–438, DOI: 10.1098/rspa.1913.0040.

(147) Glaeser, R. M. Review: Electron Crystallography: Present Excitement, a Nod to the Past, Anticipating the Future. *Journal of Structural Biology* **1999**, *128*, 3–14, DOI: 10.1006/jsbi.1999.4172.

(148) Shi, D.; Nannenga, B. L.; Iadanza, M. G.; Gonen, T. Three-dimensional electron crystallography of protein microcrystals. *eLife* **2013**, *2*, DOI: 10.7554/eLife.01345.

(149) Nannenga, B. L.; Gonen, T. The cryo-EM method microcrystal electron diffraction (MicroED). *Nature Methods* **2019**, *16*, 369–379, DOI: 10.1038/s41592-019-0395-x.

(150) Martynowycz, M. W.; Shiriaeva, A.; Ge, X.; Hattne, J.; Nannenga, B. L.; Cherezov, V.; Gonen, T. MicroED structure of the human adenosine receptor determined from a single nanocrystal in LCP.*Proceedings of the National Academy of Sciences* **2021**, *118*, DOI: 10.1073/pnas.2106041118.

(151) Egerton, R. F. Electron energy-loss spectroscopy in the TEM.*Reports on Progress in Physics* **2009**, *72*, 016502, DOI: 10.1088/0034-4885/72/1/016502.

(152) Shindo, D.; Oikawa, T. Energy Dispersive X-ray Spectroscopy.*Analytical Electron Microscopy for Materials Science* **2002**, 81–102, DOI: 10.1007/978-4-431-66988-3_4.

(153) Tizro, P.; Choi, C.; Khanlou, N. Sample Preparation for Transmission Electron Microscopy.**2019**, 417–424, DOI: 10.1007/978-1-4939-8935-5_33.

(154) Taylor, K. A.; Glaeser, R. M. Electron Diffraction of Frozen, Hydrated Protein Crystals.*Science* **1974**, *186*, 1036–1037, DOI: 10.1126/science.186.4168.1036.

(155) Cressey, D.; Callaway, E. Cryo-electron microscopy wins chemistry Nobel.*Nature* **2017**, *550*, 167–167, DOI: 10.1038/nature.2017.22738.

(156) Oostergetel, G. T.; Esselink, F. J.; Hadziioannou, G. Cryo-Electron Microscopy of Block Copolymers in an Organic Solvent.*Langmuir* **1995**, *11*, 3721–3724, DOI: 10.1021/la00010a022.

(157) Ercius, P.; Hachtel, J. A.; Klie, R. F. Chemical and bonding analysis of liquids using liquid cell electron microscopy.*MRS Bulletin* **2020**, *45*, 761–768, DOI: 10.1557/mrs.2020.230.

(158) Tanase, M.; Winterstein, J.; Sharma, R.; Aksyuk, V.; Holland, G.; Liddle, J. A. High-Resolution Imaging and Spectroscopy at High Pressure: A Novel Liquid Cell for the Transmission Electron Microscope.*Microscopy and Microanalysis* **2015**, *21*, 1629–1638, DOI: 10.1017/S1431927615015482.

(159) Liao, H.-G.; Zheng, H. Liquid Cell Transmission Electron Microscopy. *Annual Review of Physical Chemistry* **2016**, *67*, 719–747, DOI: 10.1146/annurev-physchem-040215-112501.

(160) Marton, L. La microscopie electronique des objets biologiques. *Bull. Acad. Roy. Med. Belg* **1935**, *21*, 600–617.

(161) Williamson, M. J.; Tromp, R. M.; Vereecken, P. M.; Hull, R.; Ross, F. M. Dynamic microscopy of nanoscale cluster growth at the solid–liquid interface. *Nature Materials* **2003**, *2*, 532–536, DOI: 10.1038/nmat944.

(162) Leenheer, A. J.; Jungjohann, K. L.; Harris, C. T. Design of a Heated Liquid Cell for in-situ Transmission Electron Microscopy. *Microscopy and Microanalysis* **2015**, *21*, 1293–1294, DOI: 10.1017/S1431927615007254.

(163) Nielsen, M. H.; Aloni, S.; De Yoreo, J. J. In situ TEM Imaging of $CaCO_3$ Nucleation Reveals Coexistence of Direct and Indirect Pathways. *Science* **2014**, *345*, 1158–1162, DOI: 10.1126/science.1254051.

(164) Radon, J. On the determination of functions from their integrals along certain manifolds. *Mathematisch-Physische Klasse* **1917**, *69*, 262–277.

(165) Sanders, T. L. Image Processing and 3-D Reconstruction in Tomography, English, Ph.D. Thesis, 2015.

(166) Sanders, T. MATLAB Imaging Algorithms: Image Reconstruction, Restoration, and Alignment, With a Focus in Tomography, http://www.toby-sanders.com/software, https://doi.org/10.13140/RG.2.2.33492.60801, DOI: 10.13140/RG.2.2.33492.60801.

(167) Kremer, J. R.; Mastronarde, D. N.; McIntosh, J. R. Computer Visualization of Three-Dimensional Image Data using IMOD. *Journal of Structural Biology* **1996**, *116*, 71–76, DOI: 10.1006/jsbi.1996.0013.

(168) Miao, J.; Ercius, P.; Billinge, S. J. L. Atomic electron tomography: 3D structures without crystals.*Science* **2016**, *353*, aaf2157–aaf2157, DOI: 10.1126/science.aaf2157.

(169) Ritman, E. L. Current Status of Developments and Applications of Micro-CT.*Annual Review of Biomedical Engineering* **2011**, *13*, 531–552, DOI: 10.1146/annurev-bioeng-071910-124717.

(170) Munk, W.; Wunsch, C. Ocean acoustic tomography: Rays and modes.*Reviews of Geophysics* **1983**, *21*, 777, DOI: 10.1029/RG021i004p00777.

(171) Anderson, D. L.; Dziewonski, A. M. Seismic tomography.*Scientific American* **1984**, *251*, 60–71.

(172) Takahashi, K. Introduction to Faraday tomography and its future prospects.*Publications of the Astronomical Society of Japan* **2023**, DOI: 10.1093/pasj/psac111.

(173) Sonnenfeld, B. Men in Black, 1997.

(174) Zhou, J.; Yang, Y.; Ercius, P.; Miao, J. Atomic electron tomography in three and four dimensions.*MRS Bulletin* **2020**, *45*, 290–297, DOI: 10.1557/mrs.2020.88.

(175) Xu, R.; Chen, C.-C.; Wu, L.; Scott, M. C.; Theis, W.; Ophus, C.; Bartels, M.; Yang, Y.; Ramezani-Dakhel, H.; Sawaya, M. R.; Heinz, H.; Marks, L. D.; Ercius, P.; Miao, J. Three-dimensional coordinates of individual atoms in materials revealed by electron tomography.*Nature Materials* **2015**, *14*, 1099–1103, DOI: 10.1038/nmat4426.

(176) Scott, M. C.; Chen, C.-C.; Mecklenburg, M.; Zhu, C.; Xu, R.; Ercius, P.; Dahmen, U.; Regan, B. C.; Miao, J. Electron tomography at 2.4-ångström resolution.*Nature* **2012**, *483*, 444–447, DOI: 10.1038/nature10934.

(177) Pelz, P. M.; Groschner, C.; Bruefach, A.; Satariano, A.; Ophus, C.; Scott, M. C. Simultaneous Successive Twinning Captured by Atomic Electron Tomography.*ACS Nano* **2022**, *16*, 588–596, DOI: 10.1021/acsnano.1c07772.

(178) Collins, S. M.; Midgley, P. A. Progress and opportunities in EELS and EDS tomography.*Ultramicroscopy* **2017**, *180*, 133–141, DOI: 10.1016/j.ultramic.2017.01.003.

(179) Krivanek, O. L.; Chisholm, M. F.; Nicolosi, V.; Pennycook, T. J.; Corbin, G. J.; Dellby, N.; Murfitt, M. F.; Own, C. S.; Szilagyi, Z. S.; Oxley, M. P.; Pantelides, S. T.; Pennycook, S. J. Atom-by-atom structural and chemical analysis by annular dark-field electron microscopy.*Nature* **2010**, *464*, 571–574, DOI: 10.1038/nature08879.

(180) Cleese, J. And now for something completely different.*Management Review* **1991**, *80*, 50.

(181) Panitz, J. A. Field-ion microscopy-a review of basic principles and selected applications.*Journal of Physics E: Scientific Instruments* **1982**, *15*, 1281–1294, DOI: 10.1088/0022-3735/15/12/004.

(182) Müller, E. W.; Panitz, J. A.; McLane, S. B. The Atom-Probe Field Ion Microscope.*Review of Scientific Instruments* **1968**, *39*, 83–86, DOI: 10.1063/1.1683116.

(183) Blavette, D.; Bostel, A.; Sarrau, J. M.; Deconihout, B.; Menand, A. An atom probe for three-dimensional tomography.*Nature* **1993**, *363*, 432–435, DOI: 10.1038/363432a0.

(184) Gault, B.; Moody, M. P.; Cairney, J. M.; Ringer, S. P., *Atom Probe Microscopy*; Hull, R., Jagadish, C., Jr., R. M. O., Parisi, J., Wang, Z. M., Eds.; Springer: 2012.

(185) Kellogg, G. L.; Tsong, T. T. Pulsed-laser atom-probe field-ion microscopy.*Journal of Applied Physics* **1980**, *51*, 1184–1193, DOI: 10.1063/1.327686.

(186) Gault, B.; Chiaramonti, A.; Cojocaru-Mirédin, O.; Stender, P.; Dubosq, R.; Freysoldt, C.; Makineni, S. K.; Li, T.; Moody, M.; Cairney, J. M. Atom probe tomography.*Nature Reviews Methods Primers* **2021**, *1*, 51, DOI: 10.1038/s43586-021-00047-w.

(187) Roder, P. B.; Manandhar, S.; Devaraj, A.; Perea, D. E.; Davis, E. J.; Pauzauskie, P. J. Pulsed Photothermal Heating of One-Dimensional Nanostructures.*The Journal of Physical Chemistry C* **2016**, *120*, 21730–21739, DOI: 10.1021/acs.jpcc.6b04592.

(188) Da Silva, A. K.; Leyson, G.; Kuzmina, M.; Ponge, D.; Herbig, M.; Sandlöbes, S.; Gault, B.; Neugebauer, J.; Raabe, D. Confined chemical and structural states at dislocations in Fe-9wt%Mn steels: A correlative TEM-atom probe study combined with multiscale modelling.*Acta Materialia* **2017**, *124*, 305–315, DOI: 10.1016/j.actamat.2016.11.013.

(189) Zhang, L. Q.; Liu, X. H.; Perng, Y.-C.; Cho, J.; Chang, J. P.; Mao, S. X.; Ye, Z. Z.; Huang, J. Y. Direct observation of Sn crystal growth during the lithiation and delithiation processes of SnO2 nanowires.*Micron* **2012**, *43*, 1127–1133, DOI: 10.1016/j.micron.2012.01.016.

(190) Ghosh, I.; Bose, S.; Vippagunta, R.; Harmon, F. Nanosuspension for improving the bioavailability of a poorly soluble drug and screening of stabilizing agents to inhibit crystal growth.*International Journal of Pharmaceutics* **2011**, *409*, 260–268, DOI: 10.1016/j.ijpharm.2011.02.051.

(191) Hulliger, J. Chemistry and Crystal Growth.*Angewandte Chemie International Edition in English* **1994**, *33*, 143–162, DOI: 10.1002/anie.199401431.

(192) Krämer, K. W.; Biner, D.; Frei, G.; Güdel, H. U.; Hehlen, M. P.; Lüthi, S. R. Hexagonal Sodium Yttrium Fluoride Based Green and Blue Emitting Upconversion Phosphors.*Chemistry of Materials* **2004**, *16*, 1244–1251, DOI: 10.1021/cm031124o.

(193) Zhang, F.; Wan, Y.; Yu, T.; Zhang, F.; Shi, Y.; Xie, S.; Li, Y.; Xu, L.; Tu, B.; Zhao, D. Uniform Nanostructured Arrays of Sodium Rare-Earth Fluorides for Highly Efficient Multicolor Upconversion Luminescence.*Angewandte Chemie International Edition* **2007**, *46*, 7976–7979, DOI: 10.1002/anie.200702519.

(194) Kim, W. J.; Nyk, M.; Prasad, P. N. Color-Coded Multilayer Photopatterned Microstructures Using Lanthanide(III) Ion Co-Doped NaYF Nanoparticles With Upconversion Luminescence for Possible Applications in Security.*Nanotechnology* **2009**, *20*, 185301, DOI: 10.1088/0957-4484/20/18/185301.

(195) Wang, S.; Feng, J.; Song, S.; Zhang, H. Rare Earth Fluorides Upconversion Nanophosphors: From Synthesis to Applications in Bioimaging.*CrystEngComm* **2013**, 7142–7151, DOI: 10.1039/c3ce40679b.

(196) Guo, H.; Qian, H.; Idris, N. M.; Zhang, Y. Singlet Oxygen-Induced Apoptosis of Cancer Cells Using Upconversion Fluorescent Nanoparticles as a Carrier of Photosensitizer.*Nanomedicine: Nanotechnology, Biology and Medicine* **2010**, *6*, 486–495, DOI: 10.1016/j.nano.2009.11.004.

(197) Sojka, B.; Kuricova, M.; Liskova, A.; Bartusova, M.; Banski, M.; Misiewicz, J.; Dusinska, M.; Horvathova, M.; Jahnova, E.; Ilavska, S.; Szabova, M.; Rollerova, E.; Podhorodecki, A.; Tulinska, J. Hydrophobic Sodium Fluoride-Based Nanocrystals Doped with Lanthanide Ions: Assessment of *In Vitro* Toxicity to Human Blood Lymphocytes and Phagocytes.*Journal of Applied Toxicology* **2014**, *34*, 1220–1225, DOI: 10.1002/jat.3050.

(198) Chatterjee, D. K.; Yong, Z. Upconverting Nanoparticles as Nanotransducers for Photodynamic Therapy in Cancer Cells.*Nanomedicine* **2008**, *3*, 73–82, DOI: 10.2217/17435889.3.1.73.

(199) De Wild, J.; Meijerink, A.; Rath, J. K.; van Sark, W. G. J. H. M.; Schropp, R. E. I. Environmental Science Upconverter Solar Cells: Materials and Applications.*Energy and Environmental Science* **2011**, 4835–4848, DOI: 10.1039/c1ee01659h.

(200) Shalav, A.; Richards, B. S.; Trupke, T.; Krämer, K. W.; Güdel, H. U. Application of NaYF:Er^{3+} Up-Converting Phosphors for Enhanced Near-Infrared Silicon Solar Cell Response.*Applied Physics Letters* **2005**, *86*, 013505, DOI: 10.1063/1.1844592.

(201) Arnaoutakis, G. E.; Marques-Hueso, J.; Ivaturi, A.; Fischer, S.; Goldschmidt, J. C.; Krämer, K. W.; Richards, B. S. Enhanced Energy Conversion of Up-Conversion Solar Cells by the Integration of Compound Parabolic Concentrating Optics.*Solar Energy Materials and Solar Cells* **2015**, *140*, 217–223, DOI: 10.1016/j.solmat.2015.04.020.

(202) Zhang, X. D.; Jin, X.; Wang, D. F.; Xiong, S. Z.; Geng, X. H.; Zhao, Y. Synthesis of NaYF:Yb,Er Nanocrystals and Its Application in Silicon Thin Film Solar Cells.*physica status solidi (c)* **2010**, *7*, 1128–1131, DOI: 10.1002/pssc.200982762.

(203) Dejneka, M. J.; Streltsov, A.; Pal, S.; Frutos, A. G.; Powell, C. L.; Yost, K.; Yuen, P. K.; Muller, U.; Lahiri, J. Rare Earth-Doped Glass Microbarcodes.*Proceedings of the National Academy of Sciences* **2003**, *100*, 389–393, DOI: 10.1073/pnas.0236044100.

(204) Zhang, F.; Haushalter, R. C.; Haushalter, R. W.; Shi, Y.; Zhang, Y.; Ding, K.; Zhao, D.; Stucky, G. D. Rare-Earth Upconverting Nanobarcodes for Multiplexed Biological Detection.*Small* **2011**, *7*, 1972–1976, DOI: 10.1002/smll.201100629.

(205) Dong, G.-Z.; Zhang, X.-L.; Li, L. Energy Transfer Enhanced Laser Cooling in Ho^{3+} and Tm^{3+}-Codoped Lithium Yttrium Fluoride.*Journal of the Optical Society of America B* **2013**, *30*, 939, DOI: 10.1364/JOSAB.30.000939.

(206) Minnegaliev, M.; Dyakonov, I.; Gerasimov, K.; Kalinkin, A.; Kulik, S.; Moiseev, S.; Saygin, M. Y.; Urmancheev, R. Observation and Investigation of Narrow Optical Transitions of $^{167}Er^{3+}$ Ions in Femtosecond Laser Printed Waveguides in $^{7}LiYF_4$ Crystal.*Laser Physics Letters* **2018**, *15*, 045207.

(207) Ivanova, S. E.; Tkachuk, A. M.; Mirzaeva, A.; Pellé, F. Spectroscopic Study of Thulium-Activated Double Sodium Yttrium Fluoride $Na_{0.4}Y_{0.6}F_{2.2}$:Tm^{3+} Crystals: I. Intensity of Spectra and Luminescence Kinetics.*Optics and Spectroscopy* **2008**, *105*, 228–241, DOI: 10.1134/S0030400X08080110.

(208) Tkachuk, A. M.; Ivanova, S. É.; Joubert, M. .-.-F.; Guyot, Y. Spectroscopic Study of Double Sodium-Yttrium Fluoride Crystals Doped with Erbium $Na_{0.4}Y_{0.6}F_{2.2}$:Er^{3+}: II. Luminescence Self-Quenching and Microparameters and Macrorates of Energy Transfer.*Optics and Spectroscopy* **2005**, *99*, 932–949, DOI: 10.1134/1.2149418.

(209) Guyot, Y.; Collombet, A.; Somatri, T.; Tkachuk, A.; Joubert, M.-F. Spectral and Dynamic Study of the Broad Band UV $4f^25d \rightarrow 4f^3$ Emission in Nd-Doped Double

Sodium Yttrium Fluoride Crystals and Comparison with Nd:$LiYF_4$.*Journal of Alloys and Compounds* **2002**, *341*, 174–178, DOI: 10.1016/S0925-8388(02)00063-4.

(210) Huang, B.; Dong, H.; Wong, K.-L.; Sun, L.-D.; Yan, C.-H. Fundamental View of Electronic Structures of β-$NaYF_4$, β-$NaGdF_4$, and β-$NaLuF_4$.*The Journal of Physical Chemistry C* **2016**, *120*, 18858–18870, DOI: 10.1021/acs.jpcc.6b05261.

(211) Ghosh, P.; Patra, A. Influence of Crystal Phase and Excitation Wavelength on Luminescence Properties of Eu^{3+}-Doped Sodium Yttrium Fluoride Nanocrystals.*J. Phys. Chem. C* **2008**, *112*, 19283–19292.

(212) Knowles, D.; Cassanho, A.; Jenssen, H. In *Advanced Solid State Lasers*, OSA: Washington, D.C., 1989, p CC7, DOI: 10.1364/ASSL.1989.CC7.

(213) Feng, Z.; Yang, S.; Xia, H.; Wang, C.; Jiang, D.; Zhang, J.; Gu, X.; Zhang, Y.; Chen, B.; Jiang, H. Energy Transfer and 2.0 μm Emission in Tm^{3+}/Ho^{3+} Co-Doped α-$NaYF_4$ Single Crystals.*Materials Research Bulletin* **2016**, *76*, 279–283, DOI: 10.1016/j.materresbull.2015.11.063.

(214) Li, C.; Quan, Z.; Yang, P.; Huang, S.; Lian, H.; Lin, J. Shape-Controllable Synthesis and Upconversion Properties of Lutetium Fluoride (Doped with Yb^{3+}/Er^{3+}) Microcrystals by Hydrothermal Process.*The Journal of Physical Chemistry C* **2008**, *112*, 13395–13404, DOI: 10.1021/jp802826k.

(215) Qian, L.; Zai, J.; Chen, Z.; Zhu, J.; Yuan, Y.; Qian, X. Control of the Morphology and Composition of Yttrium Fluoridevia a Salt-Assisted Hydrothermal Method.*CrystEngComm* **2010**, *12*, 199–206, DOI: 10.1039/B911401G.

(216) Hehlen, M. P. In *Optical Refrigeration*; Wiley-VCH Verlag: 2009; Chapter 2, pp 33–74.

(217) Qin, X.; Wang, X.; Xiang, H.; Xie, J.; Li, J.; Zhou, Y. Mechanism for Hydrothermal Synthesis of $LiFePO_4$ Platelets as Cathode Material for Lithium-Ion Batteries.*The Journal of Physical Chemistry C* **2010**, *114*, 16806–16812, DOI: 10.1021/jp104466e.

(218) Yoshimura, M.; Sujaridworakun, P.; Koh, F.; Fujiwara, T.; Pongkao, D.; Ahniyaz, A. Hydrothermal Conversion of Calcite Crystals to Hydroxyapatite. *Materials Science and Engineering: C* **2004**, *24*, 521–525, DOI: 10.1016/j.msec.2004.01.005.

(219) Yu, X.; Li, M.; Xie, M.; Chen, L.; Li, Y.; Wang, Q. Dopant-Controlled Synthesis of Water-Soluble Hexagonal $NaYF_4$ Nanorods with Efficient Upconversion Fluorescence for Multicolor Bioimaging. *Nano Research* **2010**, *3*, 51–60, DOI: 10.1007/s12274-010-1008-2.

(220) Mai, H.-X.; Zhang, Y.-W.; Si, R.; Yan, Z.-G.; Sun, L.-d.; You, L.-P.; Yan, C.-H. High-Quality Sodium Rare-Earth Fluoride Nanocrystals: Controlled Synthesis and Optical Properties. *Journal of the American Chemical Society* **2006**, *128*, 6426–6436, DOI: 10.1021/ja060212h.

(221) Lin, Z.; Gilbert, B.; Liu, Q.; Ren, G.; Huang, F. A Thermodynamically Stable Nanophase Material. *Journal of the American Chemical Society* **2006**, *128*, 6126–6131, DOI: 10.1021/ja057121p.

(222) May, P. B.; Suter, J. D.; May, P. S.; Berry, M. T. The Dynamics of Nanoparticle Growth and Phase Change During Synthesis of β-$NaYF_4$. *The Journal of Physical Chemistry C* **2016**, *120*, 9482–9489, DOI: 10.1021/acs.jpcc.6b01365.

(223) Fifen, J. J.; Agmon, N. Ionic Radii of Hydrated Sodium Cation from QTAIM. *The Journal of Chemical Physics* **2019**, *150*, 034304, DOI: 10.1063/1.5020150.

(224) Szefczyk, B.; Roszak, R.; Roszak, S. Structure of the Hexagonal $NaYF_4$ Phase From First-Principles Molecular Dynamics. *RSC Advances* **2014**, *4*, 22526, DOI: 10.1039/c4ra00211c.

(225) Burns, J. H. Crystal Structure of Hexagonal Sodium Neodymium Fluoride and Related Compounds. *Inorganic Chemistry* **1965**, *4*, 881–886.

(226) Palo, E.; Kankare, J.; Harju, E.; Hyppänen, I.; Hölsä, J.; Kankare, J.; Lahtinen, M.; Lastusaari, M.; Pihlgren, L.; Soukka, T. Polymorphism of $NaYF_4$:Yb^{3+}, Er^{3+} Up-Conversion Luminescence Materials.**2011**, *1*, 381–387, DOI: 10.1524/zkpr.2011.

(227) Arnold, A. A.; Terskikh, V.; Li, Q. Y.; Naccache, R.; Marcotte, I.; Capobianco, J. A. Structure of $NaYF_4$ Upconverting Nanoparticles: A Multinuclear Solid-State NMR and DFT Computational Study.*The Journal of Physical Chemistry C* **2013**, *117*, 25733–25741, DOI: 10.1021/jp405813a.

(228) Hudry, D.; Abeykoon, A. M. M.; Dooryhee, E.; Nykypanchuk, D.; Dickerson, J. H. Probing the Crystal Structure and Formation Mechanism of Lanthanide-Doped Upconverting Nanocrystals.*Chemistry of Materials* **2016**, *28*, 8752–8763, DOI: 10.1021/acs.chemmater.6b04140.

(229) Perera, S. S.; Amarasinghe, D. K.; Dissanayake, K. T.; Rabuffetti, F. A. Average and Local Crystal Structure of β-Er:Yb:$NaYF_4$ Upconverting Nanocrystals Probed by X-Ray Total Scattering.*Chemistry of Materials* **2017**, *29*, 6289–6297, DOI: 10.1021/acs.chemmater.7b01495.

(230) Aebischer, A.; Hostettler, M.; Hauser, J.; Krämer, K.; Weber, T.; Güdel, H. U.; Bürgi, H.-B. Structural and Spectroscopic Characterization of Active Sites in a Family of Light-Emitting Sodium Lanthanide Tetrafluorides.*Angewandte Chemie International Edition* **2006**, *45*, 2802–2806, DOI: 10.1002/anie.200503966.

(231) Komban, R.; Klare, J. P.; Voss, B.; Nordmann, J.; Steinhoff, H.-J.; Haase, M. An Electron Paramagnetic Resonance Spectroscopic Investigation on the Growth Mechanism of $NaYF_4$:Gd Nanocrystals.*Angewandte Chemie International Edition* **2012**, *51*, 6506–6510, DOI: 10.1002/anie.201201025.

(232) Lee, J.; Yang, J.; Kwon, S. G.; Hyeon, T. Nonclassical Nucleation and Growth of Inorganic Nanoparticles.*Nature Reviews Materials* **2016**, *1*, 16034, DOI: 10.1038/natrevmats.2016.34.

(233) Li, D.; Soberanis, F.; Fu, J.; Hou, W.; Wu, J.; Kisailus, D. Growth Mechanism of Highly Branched Titanium Dioxide Nanowires via Oriented Attachment. *Crystal Growth & Design* **2013**, *13*, 422–428, DOI: 10.1021/cg301388e.

(234) Yuwono, V. M.; Burrows, N. D.; Soltis, J. A.; Penn, R. L. Oriented Aggregation: Formation and Transformation of Mesocrystal Intermediates Revealed. *Journal of the American Chemical Society* **2010**, *132*, 2163–2165, DOI: 10.1021/ja909769a.

(235) Yin, Y.; Alivisatos, A. P. Colloidal Nanocrystal Synthesis and the Organic-Inorganic Interface. *Nature* **2005**, *437*, 664–670, DOI: 10.1038/nature04165.

(236) Cho, K.-S.; Talapin, D. V.; Gaschler, W.; Murray, C. B. Designing PbSe Nanowires and Nanorings through Oriented Attachment of Nanoparticles. *Journal of the American Chemical Society* **2005**, *127*, 7140–7147, DOI: 10.1021/ja050107s.

(237) Zhang, X.; Shen, Z.; Liu, J.; Kerisit, S. N.; Bowden, M. E.; Sushko, M. L.; De Yoreo, J. J.; Rosso, K. M. Direction-Specific Interaction Forces Underlying Zinc Oxide Crystal Growth by Oriented Attachment. *Nature Communications* **2017**, *8*, 835, DOI: 10.1038/s41467-017-00844-6.

(238) Frandsen, C.; Legg, B. A.; Comolli, L. R.; Zhang, H.; Gilbert, B.; Johnson, E.; Banfield, J. F. Aggregation-Induced Growth and Transformation of β-FeOOH Nanorods to Micron-Sized α-Fe_2O_3 Spindles. *CrystEngComm* **2014**, *16*, 1451–1458, DOI: 10.1039/C3CE40983J.

(239) Nielsen, M. H.; Li, D.; Zhang, H.; Aloni, S.; Han, T. Y.-J.; Frandsen, C.; Seto, J.; Banfield, J. F.; Cölfen, H.; De Yoreo, J. J. Investigating Processes of Nanocrystal Formation and Transformation via Liquid Cell TEM. *Microscopy and Microanalysis* **2014**, *20*, 425–436, DOI: 10.1017/S1431927614000294.

(240) Cölfen, H.; Antonietti, M. Mesocrystals: Inorganic Superstructures Made by Highly Parallel Crystallization and Controlled Alignment. *Angewandte Chemie International Edition* **2005**, *44*, 5576–5591, DOI: 10.1002/anie.200500496.

(241) Wegner, G.; Baum, P.; Müller, M.; Norwig, J.; Landfester, K. Polymers designed to control nucleation and growth of inorganic crystals from aqueous media.*Macromolecular Symposia* **2001**, *175*, 349–356, DOI: 10.1002/1521-3900(200110)175:1<349::AID-MASY349>3.0.CO;2-9.

(242) Jongen, N.; Bowen, P.; Lemaître, J.; Valmalette, J. C.; Hofmann, H. Precipitation of Self-Organized Copper Oxalate Polycrystalline Particles in the Presence of Hydroxypropylmethylcellulose (HPMC): Control of Morphology.*Journal of Colloid and Interface Science* **2000**, *226*, 189–198, DOI: 10.1006/jcis.2000.6747.

(243) Lowenstam, H. A.; Weiner, S., *On Biomineralization*; Oxford University Press: New York, NY, 1989.

(244) Braga, D.; Grepioni, F., *Crystal Engineering: From Molecules and Crystals to Materials*; Springer Netherlands: 1999, pp 421–441, DOI: 10.1007/978-94-011-4505-3_24.

(245) Beniash, E.; Aizenberg, J.; Addadi, L.; Weiner, S. Amorphous Calcium Carbonate Transforms into Calcite During Sea Urchin Larval Spicule Growth.*Proceedings of the Royal Society B: Biological Sciences* **1997**, *264*, 461–465, DOI: 10.1098/rspb.1997.0066.

(246) Politi, Y.; Arad, T.; Klein, E.; Weiner, S.; Addadi, L. Sea Urchin Spine Calcite Forms via a Transient Amorphous Calcium Carbonate Phase.*Science* **2004**, *306*, 1161–1164, DOI: 10.1126/science.1102289.

(247) Politi, Y.; Metzler, R. A.; Abrecht, M.; Gilbert, B.; Wilt, F. H.; Sagi, I.; Addadi, L.; Weiner, S.; Gilbert, P. Transformation Mechanism of Amorphous Calcium Carbonate into Calcite in the Sea Urchin Larval Spicule.*Proceedings of the National Academy of Sciences of the United States of America* **2008**, *105*, 17362–17366, DOI: 10.1073/pnas.0806604105.

(248) Zhan, J.; Lin, H.-P.; Mou, C.-Y. Biomimetic Formation of Porous Single-Crystalline $CaCO_3$ via Nanocrystal Aggregation. *Advanced Materials* **2003**, *15*, 621–623, DOI: 10.1002/adma.200304600.

(249) Duan, X.; Mei, L.; Ma, J.; Li, Q.; Wang, T.; Zheng, W. Facet-Induced Formation of Hematite Mesocrystals with Improved Lithium Storage Properties. *Chemical Communications* **2012**, *48*, 12204–12206, DOI: 10.1039/c2cc36620g.

(250) Manceau, A.; Combes, J. M. Structure of Mn and Fe Oxides and Oxyhydroxides: A Topological Approach by EXAFS. *Physics and Chemistry of Minerals* **1988**, *15*, 283–295, DOI: 10.1007/BF00307518.

(251) Michalowicz, A.; Girerd, J. J.; Goulon, J. EXAFS Determination of the Copper Oxalate Structure. Relation Between Structure and Magnetic Properties. *Inorganic Chemistry* **1979**, *18*, 3004–3010.

(252) Ghosh, P.; Kar, A.; Patra, A. Energy Transfer Study Between Ce^{3+} and Tb^{3+} Ions in Doped and Core-Shell Sodium Yttrium Fluoride Nanocrystals. *Nanoscale* **2010**, *2*, 1196, DOI: 10.1039/c0nr00019a.

(253) Auzel, F.; Goldner, P. Towards Rare-Earth Clustering Control in Doped Glasses. *Optical Materials* **2001**, *16*, 93–103, DOI: 10.1016/S0925-3467(00)00064-1.

(254) Gao, G.; Wei, J.; Shen, Y.; Peng, M.; Wondraczek, L. Heavily Eu_2O_3-Doped Yttria-Aluminoborate Glasses for Red Photoconversion With a High Quantum Yield: Luminescence Quenching and Statistics of Cluster Formation. *J. Mater. Chem. C* **2014**, *2*, 8678–8682, DOI: 10.1039/C4TC01447B.

(255) Johnson, N. J. J.; He, S.; Diao, S.; Chan, E. M.; Dai, H.; Almutairi, A. Direct Evidence for Coupled Surface and Concentration Quenching Dynamics in Lanthanide-Doped Nanocrystals. *Journal of the American Chemical Society* **2017**, *139*, 3275–3282, DOI: 10.1021/jacs.7b00223.

(256) Scherrer, P. Bestimmung der Größe und der inneren Struktur von Kolloidteilchen mittels Röntgenstrahlen.*Nachrichten von der Gesellschaft der Wissenschaften zu Göttingen, Mathematisch-Physikalische Klasse* **1918**, *2*, 98–100.

(257) Cullity, B. D. In *Elements of X-Ray Diffraction, Second Edition*, 1978, pp 99–106.

(258) Dove, P. M.; Han, N.; De Yoreo, J. J. Mechanisms of Classical Crystal Growth Theory Explain Quartz and Silicate Dissolution Behavior.*Proceedings of the National Academy of Sciences* **2005**, *102*, 15357–15362, DOI: 10.1073/pnas.0507777102.

(259) De Yoreo, J. J.; Zepeda-Ruiz, L. A.; Friddle, R. W.; Qiu, S. R.; Wasylenki, L. E.; Chernov, A. A.; Gilmer, G. H.; Dove, P. M. Rethinking Classical Crystal Growth Models Through Molecular Scale Insights: Consequences of Kink-Limited Kinetics.*Crystal Growth & Design* **2009**, *9*, 5135–5144, DOI: 10.1021/cg900543g.

(260) Erdemir, D.; Lee, A. Y.; Myerson, A. S. Nucleation of Crystals From Solution: Classical and Two-Step Models.*Accounts of Chemical Research* **2009**, *42*, 621–629, DOI: 10.1021/ar800217x.

(261) Williams, D. B.; Carter, C. B. In *Transmission Electron Microscopy: A Textbook for Materials Science*, 2009, pp 389–405.

(262) Williams, D. B.; Carter, C. B. In *Transmission Electron Microscopy: A Textbook for Materials Science*, 2009, pp 211–219.

(263) Zhang, H.; De Yoreo, J. J.; Banfield, J. F. A Unified Description of Attachment-Based Crystal Growth.*ACS Nano* **2014**, *8*, 6526–6530, DOI: 10.1021/nn503145w.

(264) Sui, Y.; Tao, K.; Tian, Q.; Sun, K. Interaction Between Y^{3+} and Oleate Ions for the Cubic-to-Hexagonal Phase Transformation of $NaYF_4$ Nanocrystals.*The Journal of Physical Chemistry C* **2012**, *116*, 1732–1739, DOI: 10.1021/jp208780x.

(265) Reimer, L.; Rennekamp, R. Imaging and Recording of Multiple Scattering Effects by Angular-Resolved Electron Energy-Loss Spectroscopy.*Ultramicroscopy* **1989**, *28*, 258–265, DOI: 10.1016/0304-3991(89)90305-7.

(266) Nakouzi, E.; Soltis, J. A.; Legg, B. A.; Schenter, G. K.; Zhang, X.; Graham, T. R.; Rosso, K. M.; Anovitz, L. M.; De Yoreo, J. J.; Chun, J. Impact of Solution Chemistry and Particle Anisotropy on the Collective Dynamics of Oriented Aggregation. *ACS Nano* **2018**, *12*, 10114–10122, DOI: 10.1021/acsnano.8b04909.

(267) Kanhere, P. D.; Zheng, J.; Chen, Z. Site Specific Optical and Photocatalytic Properties of Bi-Doped $NaTaO_3$. *The Journal of Physical Chemistry C* **2011**, *115*, 11846–11853, DOI: 10.1021/jp2003936.

(268) Suloway, C.; Pulokas, J.; Fellmann, D.; Cheng, A.; Guerra, F.; Quispe, J.; Stagg, S.; Potter, C. S.; Carragher, B. Automated Molecular Microscopy: The New Leginon System. *Journal of Structural Biology* **2005**, *151*, 41–60, DOI: 10.1016/j.jsb.2005.03.010.

(269) Newville, M. IFEFFIT: Interactive XAFS Analysis and FEFF Fitting. *Journal of Synchrotron Radiation* **2001**, *8*, 322–324, DOI: 10.1107/S0909049500016964.

(270) Ravel, B.; Newville, M. ATHENA, ARTEMIS, HEPHAESTUS: Data Analysis for X-ray Absorption Spectroscopy Using IFEFFIT. *Journal of Synchrotron Radiation* **2005**, *12*, 537–541, DOI: 10.1107/S0909049505012719.

(271) Gibbs, J. W. On the Equilibrium of Heterogeneous Substances. *Transactions of the Connecticut Academy of Arts and Sciences* **1878**, *16*, 343–524.

(272) Cölfen, H.; Antonietti, M., *Mesocrystals and Nonclassical Crystallization*; John Wiley & Sons, Ltd: 2008, pp 1–276, DOI: 10.1002/9780470994603.

(273) Karthika, S.; Radhakrishnan, T. K.; Kalaichelvi, P. A Review of Classical and Nonclassical Nucleation Theories. *Crystal Growth and Design* **2016**, *16*, 6663–6681, DOI: 10.1021/acs.cgd.6b00794.

(274) Vekilov, P. G. In *Kinetics and Thermodynamics of Multistep Nucleation and Self-Assembly in Nanoscale Materials*; John Wiley & Sons, Ltd: Hoboken, NJ, 2012; Chapter 4, pp 79–110.

(275) Cahn, J. W. On spinodal decomposition.*Acta Metallurgica* **1961**, *9*, 795–801, DOI: 10.1016/0001-6160(61)90182-1.

(276) Loh, N. D.; Sen, S.; Bosman, M.; Tan, S. F.; Zhong, J.; Nijhuis, C. A.; Král, P.; Matsudaira, P.; Mirsaidov, U. Multistep nucleation of nanocrystals in aqueous solution.*Nature Chemistry* **2017**, *9*, 77–82, DOI: 10.1038/nchem.2618.

(277) Wang, F.; Yu, H.-C.; Chen, M.-H.; Wu, L.; Pereira, N.; Thornton, K.; Van der Ven, A.; Zhu, Y.; Amatucci, G. G.; Graetz, J. Tracking lithium transport and electrochemical reactions in nanoparticles.*Nature Communications* **2012**, *3*, 1201, DOI: 10.1038/ncomms2185.

(278) Wallace, A. F.; Hedges, L. O.; Fernandez-Martinez, A.; Raiteri, P.; Gale, J. D.; Waychunas, G. A.; Whitelam, S.; Banfield, J. F.; De Yoreo, J. J. Microscopic Evidence for Liquid-Liquid Separation in Supersaturated $CaCO_3$ Solutions.*Science* **2013**, *341*, 885–889, DOI: 10.1126/science.1230915.

(279) Zou, Z.; Habraken, W. J. E. M.; Bertinetti, L.; Politi, Y.; Gal, A.; Weiner, S.; Addadi, L.; Fratzl, P. On the Phase Diagram of Calcium Carbonate Solutions.*Advanced Materials Interfaces* **2017**, *4*, 1600076, DOI: 10.1002/admi.201600076.

(280) Lee, J.; Park, K.; Chang, T.; Jung, J. C. Polymer/probe interaction in probe diffusion through a polymer matrix: methyl red diffusion in poly(vinyl acetate)/toluene solutions.*Macromolecules* **1992**, *25*, 6977–6979, DOI: 10.1021/ma00051a039.

(281) Liu, X.; Chee, S. W.; Raj, S.; Sawczyk, M.; Král, P.; Mirsaidov, U. Three-step nucleation of metal–organic framework nanocrystals.*Proceedings of the National Academy of Sciences* **2021**, *118*, DOI: 10.1073/pnas.2008880118.

(282) Bohenek, M.; Myerson, A.; Sun, W. Thermodynamics, cluster formation and crystal growth in highly supersaturated solutions of KDP, ADP and TGS.*Journal of Crystal Growth* **1997**, *179*, 213–225, DOI: 10.1016/S0022-0248(97)00121-8.

(283) Habraken, W. J. E. M. et al. Ion-association complexes unite classical and non-classical theories for the biomimetic nucleation of calcium phosphate. *Nature Communications* **2013**, *4*, 1507, DOI: 10.1038/ncomms2490.

(284) Qiu, P.; Zhou, N.; Wang, Y.; Zhang, C.; Wang, Q.; Sun, R.; Gao, G.; Cui, D. Tuning lanthanide ion-doped upconversion nanocrystals with different shapes via a one-pot cationic surfactant-assisted hydrothermal strategy. *CrystEngComm* **2014**, *16*, 1859, DOI: 10.1039/c3ce42076k.

(285) Matijevic, E. Preparation and properties of uniform size colloids. *Chemistry of Materials* **1993**, *5*, 412–426, DOI: 10.1021/cm00028a004.

(286) Zhou, J.; Del Rosal, B.; Jaque, D.; Uchiyama, S.; Jin, D. Advances and challenges for fluorescence nanothermometry. *Nature methods* **2020**, *17*, 967–980.

(287) Fernandez-Bravo, A.; Wang, D.; Barnard, E. S.; Teitelboim, A.; Tajon, C.; Guan, J.; Schatz, G. C.; Cohen, B. E.; Chan, E. M.; Schuck, P. J.; Odom, T. W. Ultralow-threshold, continuous-wave upconverting lasing from subwavelength plasmons. *Nature Materials* **2019**, *18*, 1172–1176, DOI: 10.1038/s41563-019-0482-5.

(288) Ma, Y.; Bao, J.; Zhang, Y.; Li, Z.; Zhou, X.; Wan, C.; Huang, L.; Zhao, Y.; Han, G.; Xue, T. Mammalian Near-Infrared Image Vision through Injectable and Self-Powered Retinal Nanoantennae. *Cell* **2019**, *177*, 243–255.e15, DOI: 10.1016/j.cell.2019.01.038.

(289) Hua, X. et al. Revisiting metal fluorides as lithium-ion battery cathodes. *Nature Materials* **2021**, DOI: 10.1038/s41563-020-00893-1.

(290) Morral, J.; Cahn, J. Spinodal decomposition in ternary systems. *Acta Metallurgica* **1971**, *19*, 1037–1045, DOI: 10.1016/0001-6160(71)90036-8.

(291) Tavakoli, R. Unconditionally energy stable time stepping scheme for Cahn-Morral equation: Application to multi-component spinodal decomposition and optimal space

tiling.*Journal of Computational Physics* **2016**, *304*, 441–464, DOI: 10.1016/j.jcp.2015.10.018.

(292) Nuñez, N. O.; Míguez, H.; Quintanilla, M.; Cantelar, E.; Cussó, F.; Ocaña, M. Synthesis of Spherical Down- and Up-Conversion $NaYF_4$-Based Nanophosphors with Tunable Size in Ethylene Glycol without Surfactants or Capping Additives.*European Journal of Inorganic Chemistry* **2008**, *2008*, 4517–4524, DOI: 10.1002/ejic.200800363.

(293) Xia, X.; Pant, A.; Zhou, X.; Dobretsova, E. A.; Bard, A. B.; Lim, M. B.; Roh, J. Y. D.; Gamelin, D. R.; Pauzauskie, P. J. Hydrothermal Synthesis and Solid-State Laser Refrigeration of Ytterbium-Doped Potassium-Lutetium-Fluoride (KLF) Microcrystals.*Chemistry of Materials* **2021**, *33*, 4417–4424, DOI: 10.1021/acs.chemmater.1c00420.

(294) Zhong, H.-X.; Hong, J.-M.; Cao, X.-F.; Chen, X.-T.; Xue, Z.-L. Ionic-liquid-assisted synthesis of YF_3 with different crystalline phases and morphologies.*Materials Research Bulletin* **2009**, *44*, 623–628, DOI: 10.1016/j.materresbull.2008.06.028.

(295) Zalkin, A.; Templeton, D. H. The Crystal Structures of YF_3 and Related Compounds.*Journal of the American Chemical Society* **1953**, *75*, 2453–2458, DOI: 10.1021/ja01106a052.

(296) Zhao, M.; Li, L.; Li, G. Advances of solution chemistry in stabilizing different crystal phases of inorganic nano-compounds.*CrystEngComm* **2016**, *18*, 9209–9222, DOI: 10.1039/C6CE01844K.

(297) Bessada, C.; Rakhmatullin, A.; Rollet, A.-L.; Zanghi, D. High temperature NMR approach of mixtures of rare earth and alkali fluorides: An insight into the local structure.*Journal of Fluorine Chemistry* **2009**, *130*, 45–52, DOI: 10.1016/j.jfluchem.2008.07.010.

(298) De Queiroz, T. B.; Cabrera-Baez, M.; Menegasso, P.; Martinez, E. D.; García Flores, A. F.; Rettori, C.; Urbano, R. R. Probing Surface Effects on α-$NaYF_4$ Nanoparticles

by Nuclear Magnetic Resonance. *The Journal of Physical Chemistry C* **2020**, *124*, 9523–9535, DOI: 10.1021/acs.jpcc.0c00776.

(299) Nowacki, W. Die Kristallstruktur Von EuS. *Zeitschrift für Kristallographie* **1938**, *99*, 339–341.

(300) Ghebouli, M. A.; Ghebouli, B.; Chihi, T.; Fatmi, M.; Khenata, R.; Jappor, H. R.; Naqib, S. H. Electronic band structure, elastic, optical and thermodynamic characteristic of cubic YF_3: An ab initio study. *Optik* **2021**, *239*, 166680, DOI: 10.1016/j.ijleo.2021.166680.

(301) Sarkar, S.; Mahalingam, V. Tuning the crystalline phase and morphology of the YF_3:Eu^{3+} microcrystals through fluoride source. *CrystEngComm* **2013**, *15*, 5750, DOI: 10.1039/c3ce40554k.

(302) Xiao, A. W.; Galatolo, G.; Pasta, M. The case for fluoride-ion batteries. *Joule* **2021**, *5*, 2823–2844, DOI: 10.1016/j.joule.2021.09.016.

(303) Chi, F.; Yan, L.; Lv, H.; Yan, H.; Yuan, X.; Jiang, B. Sol–Gel Preparation of Ultralow Refractive Index Magnesium Fluoride Optical Films for Broadband Antireflective Coatings. *Nanoscience and Nanotechnology Letters* **2012**, *4*, 441–444, DOI: 10.1166/nnl.2012.1330.

(304) Fisicaro, G.; Sicher, M.; Amsler, M.; Saha, S.; Genovese, L.; Goedecker, S. Surface reconstruction of fluorites in vacuum and aqueous environment. *Physical Review Materials* **2017**, *1*, 033609, DOI: 10.1103/PhysRevMaterials.1.033609.

(305) Kühne, T. D. et al. CP2K: An electronic structure and molecular dynamics software package - Quickstep: Efficient and accurate electronic structure calculations. *The Journal of Chemical Physics* **2020**, *152*, 194103, DOI: 10.1063/5.0007045.

(306) Zhang, Y.; Yang, W. Comment on "Generalized Gradient Approximation Made Simple". *Physical Review Letters* **1998**, *80*, 890–890, DOI: 10.1103/PhysRevLett.80.890.

(307) Grimme, S.; Antony, J.; Ehrlich, S.; Krieg, H. A consistent and accurate *ab initio* parametrization of density functional dispersion correction (DFT-D) for the 94 elements H-Pu. *The Journal of Chemical Physics* **2010**, *132*, 154104, DOI: 10.1063/1.3382344.

(308) VandeVondele, J.; Hutter, J. Gaussian basis sets for accurate calculations on molecular systems in gas and condensed phases. *The Journal of Chemical Physics* **2007**, *127*, 114105, DOI: 10.1063/1.2770708.

(309) Goedecker, S.; Teter, M.; Hutter, J. Separable dual-space Gaussian pseudopotentials. *Physical Review B* **1996**, *54*, 1703–1710, DOI: 10.1103/PhysRevB.54.1703.

(310) Hartwigsen, C.; Goedecker, S.; Hutter, J. Relativistic separable dual-space Gaussian pseudopotentials from H to Rn. *Physical Review B* **1998**, *58*, 3641–3662, DOI: 10.1103/PhysRevB.58.3641.

(311) Krack, M. Pseudopotentials for H to Kr optimized for gradient-corrected exchange-correlation functionals. *Theoretical Chemistry Accounts* **2005**, *114*, 145–152, DOI: 10.1007/s00214-005-0655-y.

(312) Nosé, S. Constant Temperature Molecular Dynamics Methods. *Progress of Theoretical Physics Supplement* **1991**, *103*, 1–46, DOI: 10.1143/PTPS.103.1.

(313) Hoover, W. G. Canonical dynamics: Equilibrium phase-space distributions. *Physical Review A* **1985**, *31*, 1695–1697, DOI: 10.1103/PhysRevA.31.1695.

(314) Nosé, S. A unified formulation of the constant temperature molecular dynamics methods. *The Journal of Chemical Physics* **1984**, *81*, 511–519, DOI: 10.1063/1.447334.

(315) Astley, R., *Never Gonna Give You Up*; BMG-Ariola: 1987.

(316) Lloyd-Jones, G. C.; Muñoz, M. P. Isotopic labelling in the study of organic and organometallic mechanism and structure: an account. *Journal of Labelled Compounds and Radiopharmaceuticals* **2007**, *50*, 1072–1087, DOI: 10.1002/jlcr.1382.

(317) Scott, W. J.; McMurry, J. E. Olefin synthesis via organometallic coupling reactions of enol triflates. *Accounts of Chemical Research* **1988**, *21*, 47–54, DOI: 10.1021/ar00146a001.

(318) Steenackers, B.; Cooman, L. D.; Vos, D. D. Chemical transformations of characteristic hop secondary metabolites in relation to beer properties and the brewing process: A review. *Food Chemistry* **2015**, *172*, 742–756, DOI: 10.1016/j.foodchem.2014.09.139.

(319) Rodríguez-Hornedo, N.; Nehm, S. J.; Seefeldt, K. F.; Pagán-Torres, Y.; Falkiewicz, C. J. Reaction Crystallization of Pharmaceutical Molecular Complexes. *Molecular Pharmaceutics* **2006**, *3*, 362–367, DOI: 10.1021/mp050099m.

(320) Ludi, B.; Niederberger, M. Zinc oxide nanoparticles: chemical mechanisms and classical and non-classical crystallization. *Dalton Transactions* **2013**, *42*, 12554, DOI: 10.1039/c3dt50610j.

(321) Jehannin, M.; Rao, A.; Cölfen, H. New Horizons of Nonclassical Crystallization. *Journal of the American Chemical Society* **2019**, *141*, 10120–10136, DOI: 10.1021/jacs.9b01883.

(322) De Yoreo, J. In *Crystallization via Nonclassical Pathways Volume 1: Nucleation, Assembly, Observation & Application*, 2020, pp 1–17, DOI: 10.1021/bk-2020-1358.ch001.

(323) Petrou, A. L.; Terzidaki, A. Calcium carbonate and calcium sulfate precipitation, crystallization and dissolution: Evidence for the activated steps and the mechanisms from the enthalpy and entropy of activation values. *Chemical Geology* **2014**, *381*, 144–153, DOI: 10.1016/j.chemgeo.2014.05.018.

(324) Reddy, M. M. Physical-Chemical Mechanisms That Affect Regulation of Crystallization. *Chemical Aspect of Regulation of Mineralization* **1988**, 3–8.

(325) Chen, K.; Xue, D. pH-assisted crystallization of Cu_2O: chemical reactions control the evolution from nanowires to polyhedra. *CrystEngComm* **2012**, *14*, 8068, DOI: 10.1039/c2ce26084k.

(326) Zhang, X.; Yu, H.; Guo, L.; Jin, J.; Li, Q.; Guo, Y.; Fu, Y.; Shi, Y.; Zhao, L. Comprehensive model and investigation of F^- ions-induced cubic-to-hexagonal phase transformation in $NaYF_4$. *Journal of Alloys and Compounds* **2017**, *728*, 1254–1259, DOI: 10.1016/j.jallcom.2017.09.105.

(327) Lucier, B. E. G.; Johnston, K. E.; Arnold, D. C.; Lemyre, J.-L.; Beaupré, A.; Blanchette, M.; Ritcey, A. M.; Schurko, R. W. Comprehensive Solid-State Characterization of Rare Earth Fluoride Nanoparticles. *The Journal of Physical Chemistry C* **2014**, *118*, 1213–1228, DOI: 10.1021/jp408148b.

(328) Gerken, M.; Boatz, J.; Kornath, A.; Haiges, R.; Schneider, S.; Schroer, T.; Christe, K. The NMR shifts are not a measure for the nakedness of the fluoride anion. *Journal of Fluorine Chemistry* **2002**, *116*, 49–58, DOI: 10.1016/S0022-1139(02)00101-X.

(329) Zhang, L.; Yu, J. C.; Xu, A.-W.; Li, Q.; Kwong, K. W.; Yu, S.-H. Peanut-shaped nanoribbon bundle superstructures of malachite and copper oxide. *Journal of Crystal Growth* **2004**, *266*, 545–551, DOI: 10.1016/j.jcrysgro.2004.03.002.

(330) Sand, K. K.; Rodriguez-Blanco, J. D.; Makovicky, E.; Benning, L. G.; Stipp, S. L. S. Crystallization of $CaCO_3$ in Water–Alcohol Mixtures: Spherulitic Growth, Polymorph Stabilization, and Morphology Change. *Crystal Growth & Design* **2012**, *12*, 842–853, DOI: 10.1021/cg2012342.

(331) Gránásy, L.; Pusztai, T.; Tegze, G.; Warren, J. A.; Douglas, J. F. Growth and form of spherulites. *Physical Review E* **2005**, *72*, 011605, DOI: 10.1103/PhysRevE.72.011605.

(332) Chen, Y.-S.; Griffith, M. J.; Cairney, J. M. Cryo Atom Probe: Freezing atoms in place for 3D mapping.*Nano Today* **2021**, *37*, 101107, DOI: 10.1016/j.nantod.2021.101107.

(333) Perea, D. E.; Schreiber, D. K.; Ryan, J. V.; Wirth, M. G.; Deng, L.; Lu, X.; Du, J.; Vienna, J. D. Tomographic mapping of the nanoscale water-filled pore structure in corroded borosilicate glass.*npj Materials Degradation* **2020**, *4*, 8, DOI: 10.1038/s41529-020-0110-5.

(334) Perea, D.; Wirth, M. Prospects of mapping macromolecular structure and ionic gradients in hydrated biological specimens using Atom Probe Tomography.*Microscopy and Microanalysis* **2021**, *27*, 1518–1518, DOI: 10.1017/S1431927621005602.

(335) Kalish, R. Doping of diamond.*Carbon* **1999**, *37*, 781–785, DOI: 10.1016/S0008-6223(98)00270-X.

(336) Goss, J. P.; Eyre, R. J.; Briddon, P. R. Theoretical models for doping diamond for semiconductor applications.*physica status solidi (b)* **2008**, *245*, 1679–1700, DOI: 10.1002/pssb.200744115.

(337) Crawford, K. G.; Maini, I.; Macdonald, D. A.; Moran, D. A. Surface transfer doping of diamond: A review.*Progress in Surface Science* **2021**, *96*, 100613, DOI: 10.1016/j.progsurf.2021.100613.

(338) Smith, J. M.; Meynell, S. A.; Jayich, A. C. B.; Meijer, J. Colour centre generation in diamond for quantum technologies.*Nanophotonics* **2019**, *8*, 1889–1906, DOI: 10.1515/nanoph-2019-0196.

(339) Nebel, C. E. In *Diamond for Quantum Applications Part 1*, Nebel, C. E., Aharonovich, I., Mizuochi, N., Hatano, M., Eds.; Semiconductors and Semimetals, Vol. 103; Elsevier: 2020, pp 73–136, DOI: https://doi.org/10.1016/bs.semsem.2020.03.004.

(340) Achard, J.; Jacques, V.; Tallaire, A. Chemical vapour deposition diamond single crystals with nitrogen-vacancy centres: a review of material synthesis and technology for quantum sensing applications.*Journal of Physics D: Applied Physics* **2020**, *53*, 313001, DOI: 10.1088/1361-6463/ab81d1.

(341) Reineck, P.; Francis, A.; Orth, A.; Lau, D. W. M.; Nixon-Luke, R. D. V.; Rastogi, I. D.; Razali, W. A. W.; Cordina, N. M.; Parker, L. M.; Sreenivasan, V. K. A.; Brown, L. J.; Gibson, B. C. Brightness and Photostability of Emerging Red and Near-IR Fluorescent Nanomaterials for Bioimaging.*Advanced Optical Materials* **2016**, *4*, 1549–1557, DOI: 10.1002/adom.201600212.

(342) Mzyk, A.; Ong, Y.; Moreno, A. R. O.; Padamati, S. K.; Zhang, Y.; Reyes-San-Martin, C. A.; Schirhagl, R. Diamond Color Centers in Diamonds for Chemical and Biochemical Analysis and Visualization.*Analytical Chemistry* **2022**, *94*, 225–249, DOI: 10.1021/acs.analchem.1c04536.

(343) Ju, Z.; Lin, J.; Shen, S.; Wu, B.; Wu, E. Preparations and applications of single color centers in diamond.*Advances in Physics: X* **2021**, *6*, DOI: 10.1080/23746149.2020.1858721.

(344) Fu, C.-C.; Lee, H.-Y.; Chen, K.; Lim, T.-S.; Wu, H.-Y.; Lin, P.-K.; Wei, P.-K.; Tsao, P.-H.; Chang, H.-C.; Fann, W. Characterization and application of single fluorescent nanodiamonds as cellular biomarkers.*Proceedings of the National Academy of Sciences* **2007**, *104*, 727–732, DOI: 10.1073/pnas.0605409104.

(345) Ermakova, A.; Pramanik, G.; Cai, J.-M.; Algara-Siller, G.; Kaiser, U.; Weil, T.; Tzeng, Y.-K.; Chang, H. C.; McGuinness, L. P.; Plenio, M. B.; Naydenov, B.; Jelezko, F. Detection of a Few Metallo-Protein Molecules Using Color Centers in Nanodiamonds.*Nano Letters* **2013**, *13*, 3305–3309, DOI: 10.1021/nl4015233.

(346) Mainwood, A. Point Defects in Natural and Synthetic Diamond: What They Can Tell Us about CVD Diamond.*Physical Status Solidi A* **1999**, *172*, 25–35.

(347) Davies, G. Current problems in diamond: towards a quantitative understanding. *Physica B: Condensed Matter* **1999**, *273-274*, 15–23, DOI: 10.1016/S0921-4526(99)00398-1.

(348) Mast, J.; Verleysen, E.; Hodoroaba, V.-D.; Kaegi, R. Characterization of nanomaterials by transmission electron microscopy: Measurement procedures. *Characterization of Nanoparticles* **2020**, 29–48, DOI: 10.1016/B978-0-12-814182-3.00004-3.

(349) Barroo, C.; Magyar, A. P.; Akey, A. J.; Bell, D. C. Preparation and Characterization of Eu-Doped Diamond Samples by Atom Probe Tomography. *Microscopy and Microanalysis* **2016**, *22*, 694–695, DOI: 10.1017/S1431927616004323.

(350) Schirhagl, R.; Raatz, N.; Meijer, J.; Markham, M.; Gerstl, S.; Degen, C. Nanometer-scale isotope analysis of bulk diamond by atom probe tomography. *Diamond and Related Materials* **2015**, *60*, 60–65, DOI: 10.1016/j.diamond.2015.10.016.

(351) Reddy, S. M.; Saxey, D. W.; Rickard, W. D. A.; Fougerouse, D.; Montalvo, S. D.; Verberne, R.; Riessen, A. Atom Probe Tomography: Development and Application to the Geosciences. *Geostandards and Geoanalytical Research* **2020**, *44*, 5–50, DOI: 10.1111/ggr.12313.

(352) Chen, Y.-S.; Haley, D.; Gerstl, S. S. A.; London, A. J.; Sweeney, F.; Wepf, R. A.; Rainforth, W. M.; Bagot, P. A. J.; Moody, M. P. Direct observation of individual hydrogen atoms at trapping sites in a ferritic steel. *Science* **2017**, *355*, 1196–1199, DOI: 10.1126/science.aal2418.

(353) Chen, Y.-S.; Lu, H.; Liang, J.; Rosenthal, A.; Liu, H.; Sneddon, G.; McCarroll, I.; Zhao, Z.; Li, W.; Guo, A.; Cairney, J. M. Observation of hydrogen trapping at dislocations, grain boundaries, and precipitates. *Science* **2020**, *367*, 171–175, DOI: 10.1126/science.aaz0122.

(354) Sundell, G.; Thuvander, M.; Andrén, H.-O. Hydrogen analysis in APT: Methods to control adsorption and dissociation of H_2. *Ultramicroscopy* **2013**, *132*, 285–289, DOI: 10.1016/j.ultramic.2013.01.007.

(355) Tsong, T. Field ion image formation. *Surface Science* **1978**, *70*, 211–233.

(356) Mukherjee, S.; Watanabe, H.; Isheim, D.; Seidman, D. N.; Moutanabbir, O. Laser-Assisted Field Evaporation and Three-Dimensional Atom-by-Atom Mapping of Diamond Isotopic Homojunctions. *Nano Letters* **2016**, *16*, 1335–1344, DOI: 10.1021/acs.nanolett.5b04728.

(357) Gilbert, M.; Vurpillot, F.; Vella, A.; Bernas, H.; Deconihout, B. Some aspects of the silicon behaviour under femtosecond pulsed laser field evaporation. *Ultramicroscopy* **2007**, *107*, 767–772, DOI: 10.1016/j.ultramic.2007.02.027.

(358) Grill, A.; Patel, V.; Cohen, S. Electrical resistivities of diamond-like carbon. *Diamond and Related Materials* **1994**, *3*, 281–284, DOI: 10.1016/0925-9635(94)90093-0.

(359) Thompson, K.; Lawrence, D.; Larson, D.; Olson, J.; Kelly, T.; Gorman, B. In situ site-specific specimen preparation for atom probe tomography. *Ultramicroscopy* **2007**, *107*, 131–139, DOI: 10.1016/j.ultramic.2006.06.008.

(360) Wu, W.; Xu, Z.; Fang, F.; Liu, B.; Xiao, Y.; Chen, J.; Wang, X.; Liu, H. Decrease of FIB-induced lateral damage for diamond tool used in nano cutting. *Nuclear Instruments and Methods in Physics Research Section B: Beam Interactions with Materials and Atoms* **2014**, *330*, 91–98, DOI: 10.1016/j.nimb.2014.04.005.

(361) Tong, Z.; Jiang, X.; Luo, X.; Bai, Q.; Xu, Z.; Blunt, L.; Liang, Y. Review on FIB-Induced Damage in Diamond Materials. *Current Nanoscience* **2016**, *12*, 685–695.

(362) Rubanov, S.; Suvorova, A. Ion implantation in diamond using 30keV Ga+ focused ion beam. *Diamond and Related Materials* **2011**, *20*, 1160–1164, DOI: 10.1016/j.diamond.2011.06.027.

(363) Vella, A. On the interaction of an ultra-fast laser with a nanometric tip by laser assisted atom probe tomography: A review. *Ultramicroscopy* **2013**, *132*, 5–18, DOI: 10.1016/j.ultramic.2013.05.016.

(364) Blavette, D.; Kassab, T. A.; Cadel, E.; Mackel, A.; Vurpillot, F.; Gilbert, M.; Cojocaru, O.; Deconihout, B. Laser-assisted atom probe tomography and nanosciences. *International Journal of Materials Research* **2008**, *99*, 454–460, DOI: 10.3139/146.101672.

(365) Bunton, J. H.; Olson, J. D.; Lenz, D. R.; Kelly, T. F. Advances in Pulsed-Laser Atom Probe: Instrument and Specimen Design for Optimum Performance. *Microscopy and Microanalysis* **2007**, *13*, 418–427, DOI: 10.1017/S1431927607070869.

(366) Che, J.; Çağın, T.; Deng, W.; Goddard, W. A. Thermal conductivity of diamond and related materials from molecular dynamics simulations. *The Journal of Chemical Physics* **2000**, *113*, 6888–6900, DOI: 10.1063/1.1310223.

(367) Tkadletz, M.; Waldl, H.; Schiester, M.; Lechner, A.; Schusser, G.; Krause, M.; Schalk, N. Efficient preparation of microtip arrays for atom probe tomography using fs-laser processing. *Ultramicroscopy* **2023**, *246*, 113672, DOI: 10.1016/j.ultramic.2022.113672.

(368) Chiaramonti, A. N.; Miaja-Avila, L.; Caplins, B. W.; Blanchard, P. T.; Diercks, D. R.; Gorman, B. P.; Sanford, N. A. Field Ion Emission in an Atom Probe Microscope Triggered by Femtosecond-Pulsed Coherent Extreme Ultraviolet Light. *Microscopy and Microanalysis* **2020**, *26*, 258–266, DOI: 10.1017/S1431927620000203.

(369) Rutledge, K. M.; Gleason, K. K. Hydrogen in CVD Diamond Films. *Chemical Vapor Deposition* **1996**, *2*, 37–43, DOI: 10.1002/cvde.19960020203.

(370) Chen, Y.-S.; Liu, P.-Y.; Niu, R.; Devaraj, A.; Yen, H.-W.; Marceau, R. K. W.; Cairney, J. M. Atom Probe Tomography for the Observation of Hydrogen in Materials: A Review. *Microscopy and Microanalysis* **2023**, *29*, 1–15, DOI: 10.1093/micmic/ozac005.

(371) Takahashi, J.; Kawakami, K.; Miura, K.; Hirano, M.; Ohtsu, N. Quantitative Analysis of Nitrogen by Atom Probe Tomography Using Stoichiometric γ '-Fe_4 N Consisting of ^{15}N Isotope.*Microscopy and Microanalysis* **2022**, *28*, 42–52, DOI: 10.1017/S1431927621013623.

(372) Howes, V. R. The Graphitization of Diamond.*Proceedings of the Physical Society* **1962**, *80*, 648–662, DOI: 10.1088/0370-1328/80/3/310.

(373) Miaja-Avila, L.; Caplins, B. W.; Chiaramonti, A. N.; Blanchard, P. T.; Brubaker, M. D.; Davydov, A. V.; Diercks, D. R.; Gorman, B. P.; Rishinaramangalam, A.; Feezell, D. F.; Bertness, K. A.; Sanford, N. A. Extreme Ultraviolet Radiation Pulsed Atom Probe Tomography of III-Nitride Semiconductor Materials.*The Journal of Physical Chemistry C* **2021**, *125*, 2626–2635, DOI: 10.1021/acs.jpcc.0c08753.

(374) Kennedy, J. F. We choose to go to the Moon.*Speech delivered at Rice University, Houston, Texas* **1962**.

(375) Darwin, C. Letter no. 3272.*Darwin Correspondence Project*.

(376) Bard, A. B.; Lim, M. B.; Zhou, X.; Rodríguez Manzo, J. A.; Alsem, D. H.; Pauzauskie, P. J. Observation of Void Formation in Cubic $NaYF_4$ Nanocrystals Using In Situ Heating Transmission Electron Microscopy.*Microscopy and Microanalysis* **2019**, *25*, 1496–1497, DOI: 10.1017/S1431927619008213.

(377) Xia, X.; Pant, A.; Zhou, X.; Dobretsova, E. A.; Bard, A. B.; Lim, M. B.; Roh, J. Y. D.; Gamelin, D. R.; Pauzauskie, P. J. Hydrothermal Synthesis and Solid-State Laser Refrigeration of Ytterbium-Doped Potassium-Lutetium-Fluoride (KLF) Microcrystals.*Chemistry of Materials* **2021**, *33*, 4417–4424, DOI: 10.1021/acs.chemmater.1c00420.

(378) Zhou, X.; Xia, X.; Smith, B. E.; Lim, M. B.; Bard, A. B.; Pant, A.; Pauzauskie, P. J. Interface-Dependent Radiative Lifetimes of Yb^{3+}, Er^{3+} Co-doped Single $NaYF_4$

Upconversion Nanowires.*ACS Applied Materials & Interfaces* **2019**, *11*, 22817–22823, DOI: 10.1021/acsami.8b17271.

(379) Felsted, R. G.; Chun, J.; Schenter, G. K.; Bard, A. B.; Xia, X.; Pauzauskie, P. J. Optical assembly of nanostructures via surface roughness.*In Submission* **2023**.

(380) Felsted, R. G.; Pant, A.; Lu, L.; Bard, A. B.; Beck, R. A.; Bishop, B.; Erickson, C.; Perea, D. E.; Spurgeon, S. R.; Gamelin, D. R.; Holmberg, V. C.; Li, X.; Pauzauskie, P. J. Colloidal Semiconductor Quantum Dots in Dichalcogenide Cavities Prepared through Pulsed Laser Deposition.*In Preparation* **2023**.

Appendix A

DERIVATION OF ELECTRON WAVELENGTH EQUATION

This is not original research of mine, however in the process of writing this dissertation I had difficulty finding concise derivations for this formula. While it is probably too much to put into the main body of the text, I do think it is useful to refer to the derivation in order to understand where the variables come from. Lacking a satisfactory external reference, I instead am showing the derivation here:

As shown in Chapter 1.3.1, we can express the classical wavelength of an electron beam with the following equation:

$$\lambda_o = \frac{h}{\sqrt{2mE_o}} \tag{A.1}$$

Note that naught subscripts are used to differentiate the classical components from the relativistic components (which will have the subscript r), and the eV in Chapter 1.3.1 has been replaced with a more general E for conciseness.

In order to account for the relativistic momentum contribution, we need to use the momentum analogue to Einstein's mass-energy equivalence:

$$E_r^2 = (pc)^2 + (mc^2)^2 \tag{A.2}$$

We know from Planck's relation that

$$E = \frac{hc}{\lambda} \tag{A.3}$$

Therefore, we can plug equation A.2 into equation A.3, which results in

$$\sqrt{(pc)^2 + (mc^2)^2} = \frac{hc}{\lambda_r} \tag{A.4}$$

This can be arranged to

$$\lambda_r = \frac{hc}{\sqrt{(pc)^2 + (mc^2)^2}} \tag{A.5}$$

From Einstein's famous equation, we can then substitute in $E = mc^2$ to result in

$$\lambda_r = \frac{hc}{\sqrt{(pc)^2 + (E_o)^2}} \tag{A.6}$$

We can then remove the variable c from the numerator, resulting in

$$\lambda_r = \frac{h}{\sqrt{p^2 + \frac{E_o^2}{c^2}}} \tag{A.7}$$

We can then take the momentum term (the denominator) from equation A.1 and substitute it in for p in the above equation, resulting in

$$\lambda_r = \frac{h}{\sqrt{2mE_o + \frac{E_o^2}{c^2}}} \tag{A.8}$$

To put this equation into the more familiar form seen in equation 1.2, we can multiply the final term of the denominator by $\frac{2m}{2m}$ to result in

$$\lambda_r = \frac{h}{\sqrt{2mE_o + \frac{2mE_o^2}{2mc^2}}} \tag{A.9}$$

and then distribute the denominator, resulting in the final equation

$$\lambda_r = \frac{h}{\sqrt{2mE_o(1 + \frac{E_o}{2mc^2})}} \tag{A.10}$$

Appendix B

SUPPORTING INFORMATION FOR CHAPTER 2

Figure S1: STEM-EDS analysis of mixed-α nucleated β particles (percentages in atomic percent with respect to total rare earth concentration)

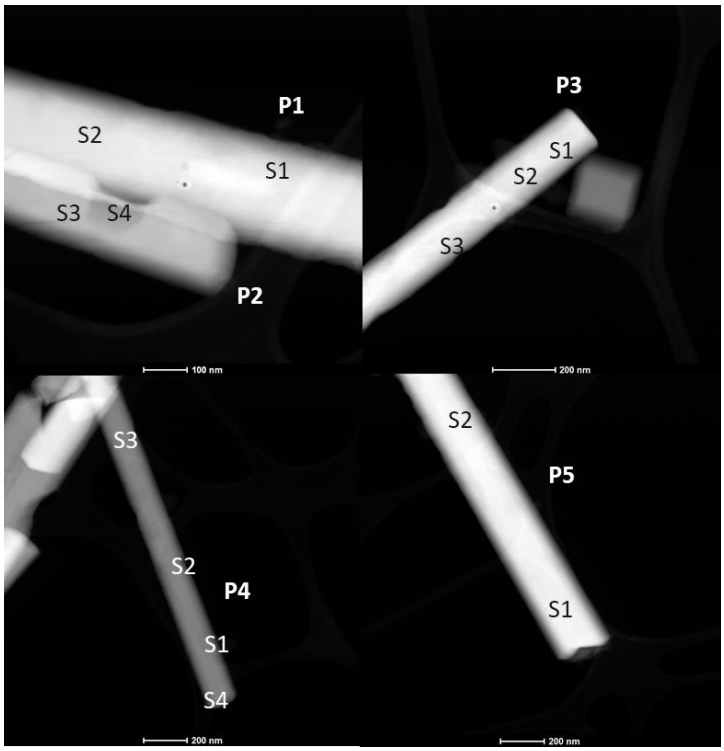

Particle	Spot	Y%	Yb%	Er%
P1	S1	93.3	6.16	0.5
	S2	94.4	4.88	0.8
P2	S1	98.4	1.32	0.3
	S2	97.1	2.73	0.2
P3	S1	98.8	0.26	1
	S2	98.7	0.47	0.9
	S3	90.6	7.8	1.6
P4	S1	94.7	5.26	0
	S2	91.6	5.32	3.1
	S3	94.7	4.72	0.6
	S4	90.3	8.15	1.6
P5	S1	89.5	8.8	1.7
	S2	90.1	8.16	1.7

Figure S2: Simulations of SAED patterns of various orientations of potential particles in the synthesis vessel with similar d spacings compared to experimental data

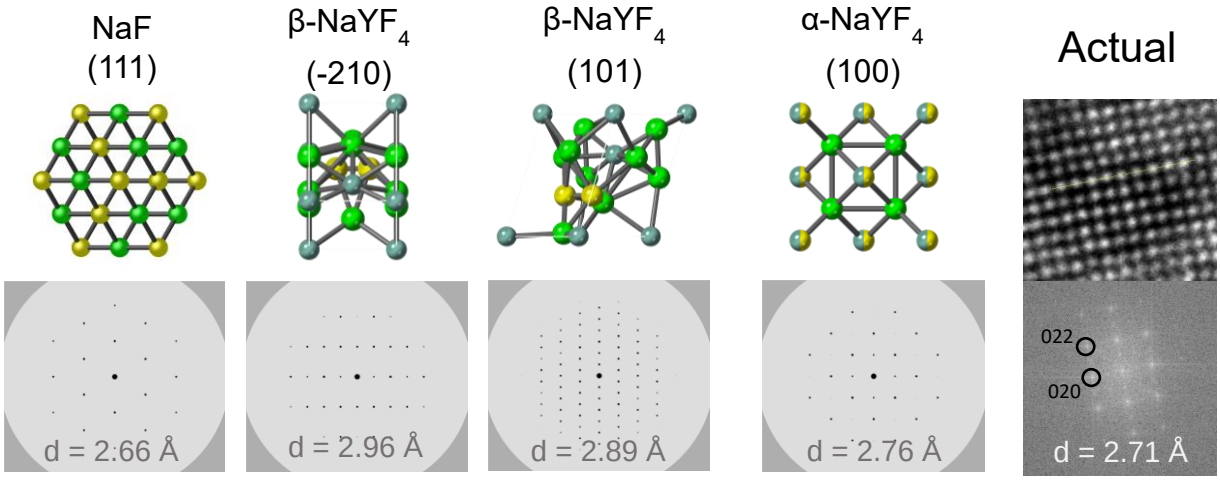

022: Theoretical = 0.514 $Å^{-1}$, Experimental = 0.515 $Å^{-1}$
020: Theoretical = 0.351 $Å^{-1}$, Experimental = 0.359 $Å^{-1}$

Figure S3: Mass Spectrum via Atom Probe Tomography of the β-$NaYF_4$ end cap

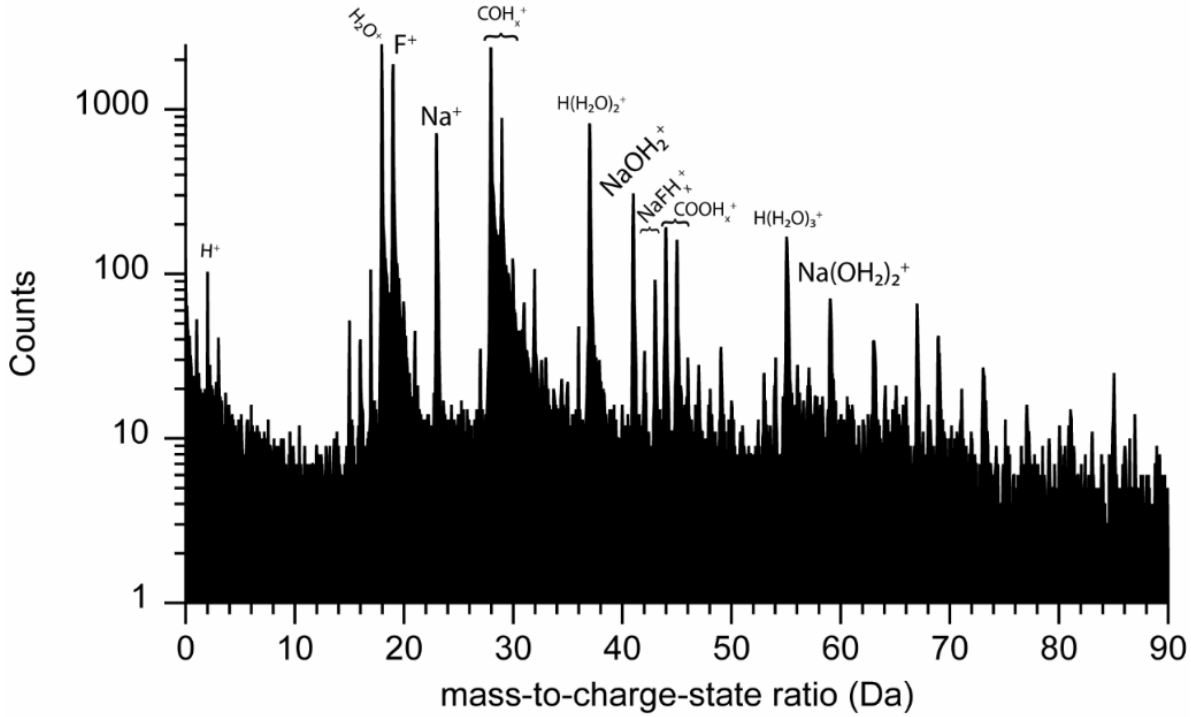

Table S4: DLS characterization of $NaYF_4$ particles

	Average hydrodynamic radius (nm)	Average Zeta Potential (mV)
α (cubic)	326.9	-71.0
β (hexagonal)	750.8	+18.7

Figure S4: Sample DLS data

Representative DLS data. Many scans were averaged in Table S4, so numbers vary slightly.

Figure S5: FTIR of $NAYF_4$ particles before and after calcination

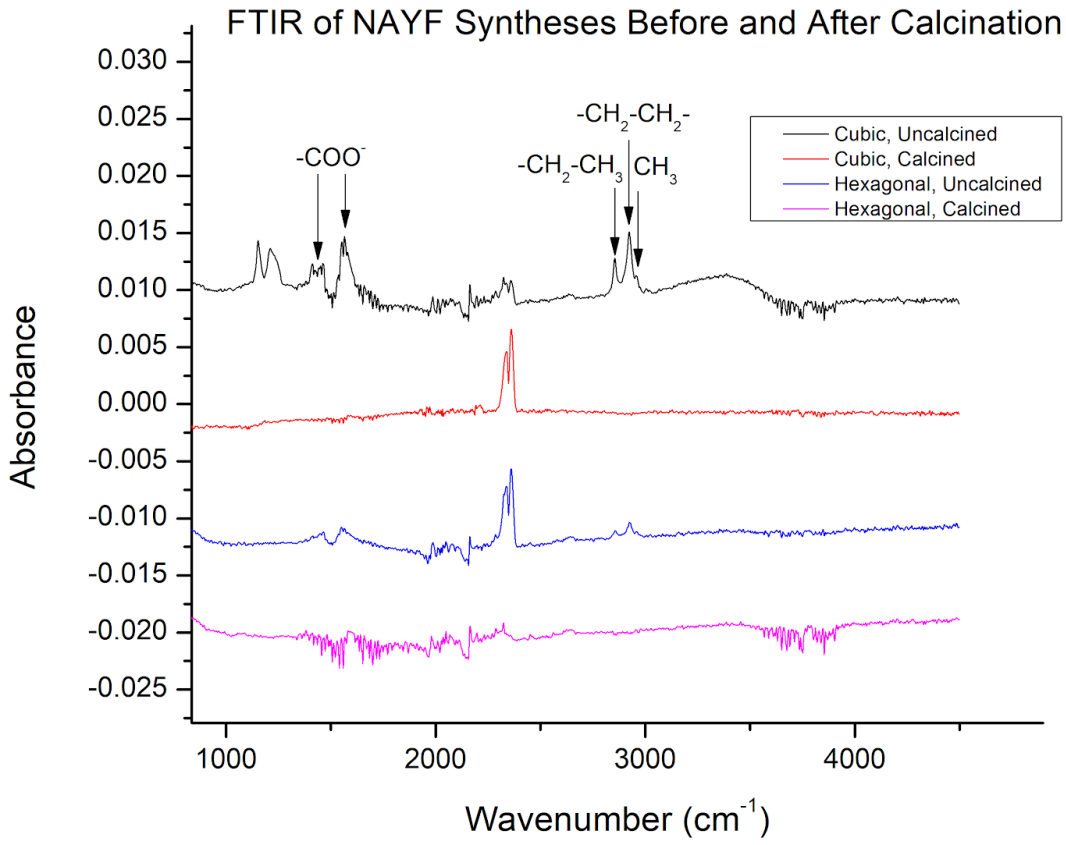

Experimental: Fourier-Transform Infrared (FTIR) spectra were taken on a Bruker VERTEX 70v FTIR Spectrometer in attenuated total reflectance (ATR) mode. Powdered $NaYF_4$ samples were placed on the diamond ATR crystal and 16 scans were averaged. The spectral resolution of the instrument is 2 cm^{-1}.

Figure S6: TEM of faceted α-$NaYF_4$ clusters

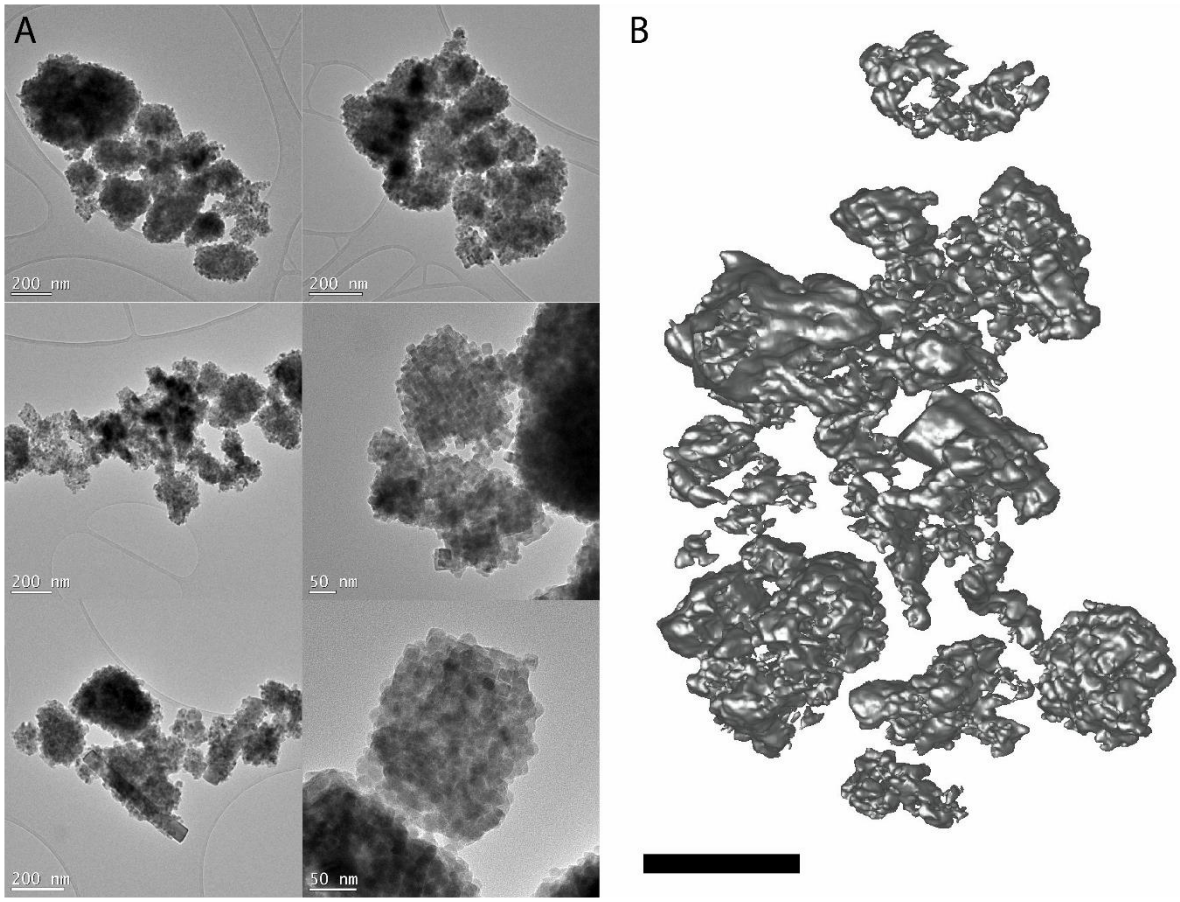

(A) Multiple clusters of α-$NaYF_4$ showing clear mesoscale faceting. (B) Tomographic reconstruction of several α-$NaYF_4$ clusters. Scale = 200 nm.

Figure S7: TEM of α-$NaYF_4$ Mesocrystals

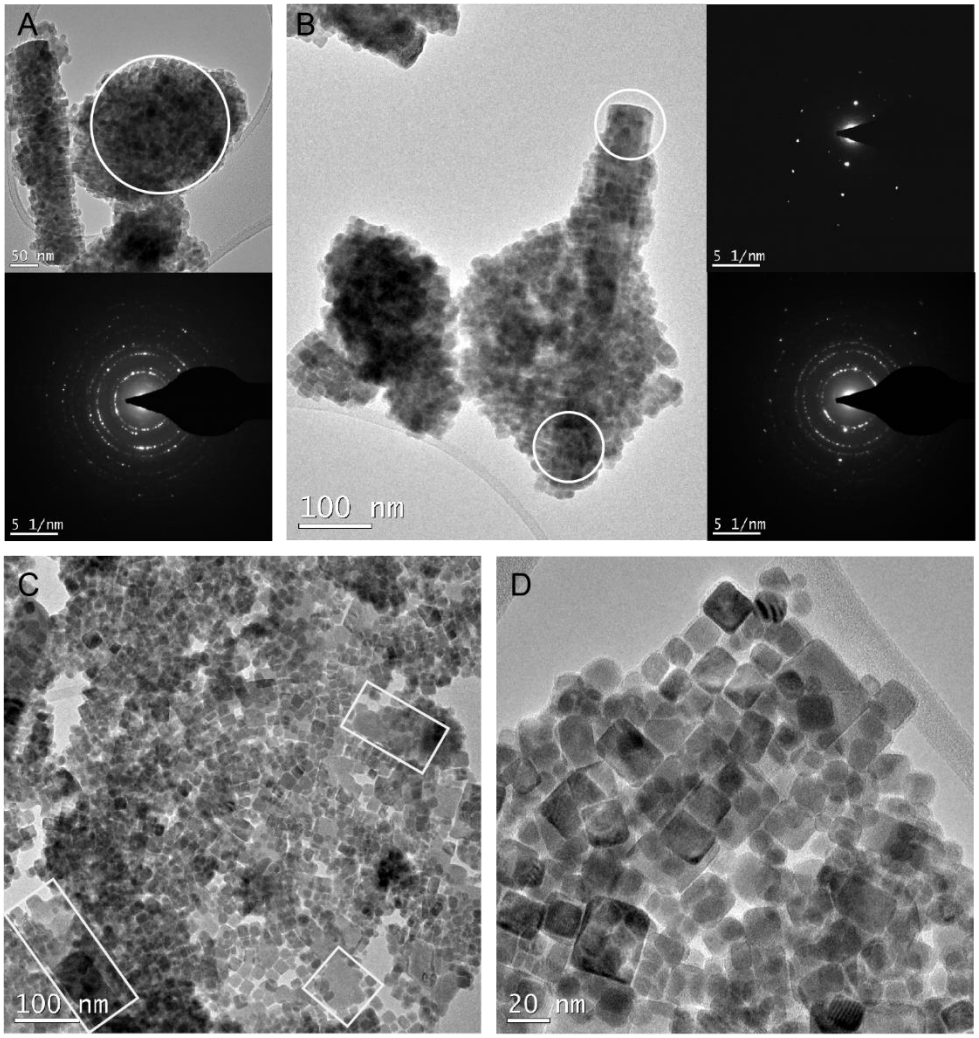

(A) TEM and SAED of an α-$NaYF_4$ cluster from the three hour synthesis showing orientation along multiple axes. Also note the single β-$NaYF_4$ nanowire growing inside a cluster of small α-$NaYF_4$. Circled region is approximate area of SAED. (B) β-$NaYF_4$ nanowire growing from a clearly faceted α-$NaYF_4$ cluster with SAED. Note crystallographic orientation of both species in bottom SAED. (C) Two dimensional layer of α-$NaYF_4$ from the same synthesis showing clear mesoscopic order. Highlighted particles appear to have undergone oriented attachment. (D) Zoom on mesoscopically ordered α-$NaYF_4$.

Figure S8: Liquid cell TEM of cubic $NaYF_4$ particles suspended in water aggregating due to the electron beam.

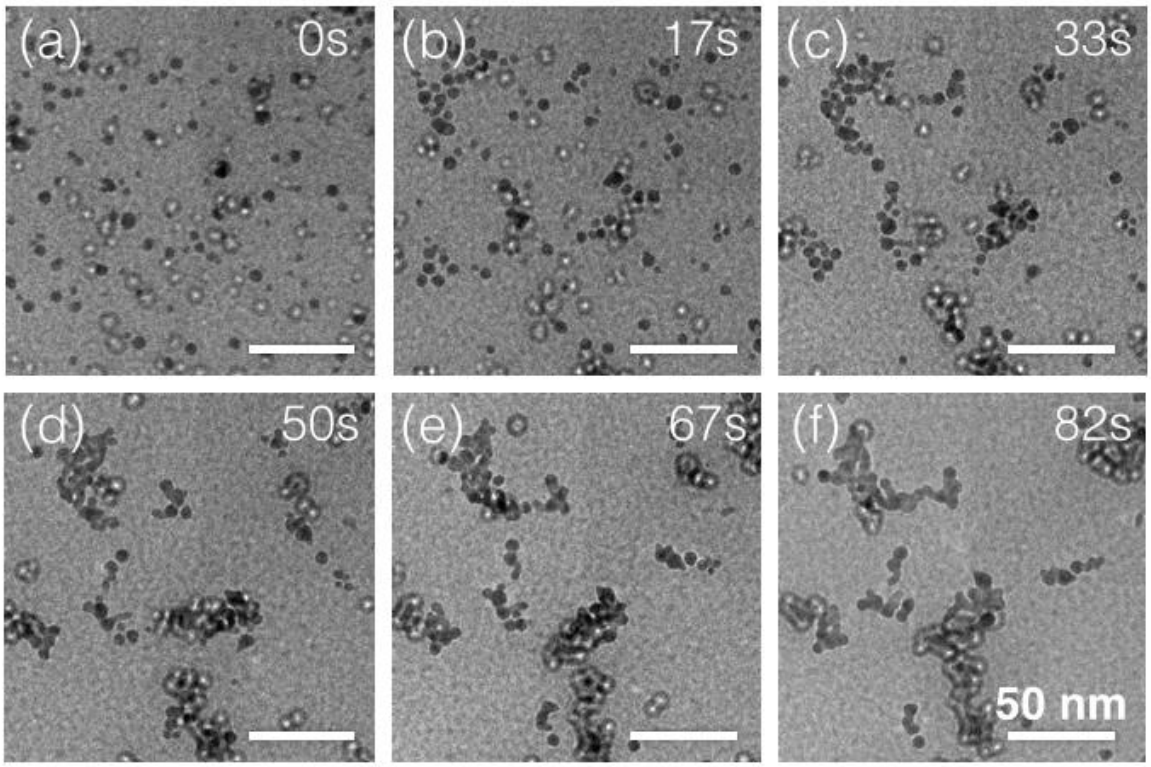

EXAFS Structural Analysis: Further details

I. Data reduction to $k^3\chi(k)$

The transmission edge jumps were about 0.025 and 0.05 optical density units. Fluorescence count rates were 70 kHz and 100 kHz near the edge. The tall white-line peak at the edge is sensitive to overabsorption, so it was possible to use the transmission data (assumed free of this effect) as a template with which to apply a simple correction to the fluorescence data. The resulting EXAFS data was good to about 14$Å^{-1}$.

2. Model for P$\bar{6}$ crystal structure

We assume that the Yb is in a Y site. To resolve the mixed occupancy of the Y2/Na1 site, we first transformed the structure into a P1 basis using WebATOMS,[1] doubled the c-axis lattice parameter, and halved the *z* position parameter of each atom, thus leaving the Cartesian-coordinate positions of all the atoms unaffected, but making an empty space in the doubled

structure. We then filled that space with a copy of the existing atoms, shifted by $\vec{c}/2$, resulting in a structure which was identical to the original but described using twice as many atoms in twice as big a cell. We then removed the Y2 site in the original half and the Na1 site in the copied half. The resulting crystal-structure description, with Yb in the Y1 site is as follows:

```
## This P1 file was generated by Demeter 0.9.26
## Demeter written by and copyright (c) Bruce Ravel, 2006-2018
#
# File modified to double c and remove Y2 in the lower copy and Na1 in
the upper.
#Note that Na2 is half-occupied, so path strengths need to
# be adjusted
space = P 1
a     =   5.91480    b    =   5.91480    c     =   6.99200
alpha =  90.00000    beta =  90.00000    gamma = 120.00000
rmax  =   5.24400    core  = Y1
polarization = 0  0  0
shift =   0  0  0
atoms
# el.     x           y           z         tag
  Yb      0.00000     0.00000     0.00000   Yb1
  Na     0.66670     0.33333     0.25000   Na1
  Na     0.33333     0.66670     0.34450   Na2
  Na     0.33333     0.66670     0.15550   Na2
  F      0.64600     0.12560     0.00000   F1
  F      0.87440     0.52040     0.00000   F1
  F      0.47960     0.35400     0.00000   F1
  F      0.69700     0.72200     0.250000   F2
  F      0.27800     0.97500     0.250000   F2
  F      0.02500     0.30300     0.250000   F2
  Yb      0.00000     0.00000     0.50000   Yb1a
  Yb      0.66670     0.33333     0.75000   Yb2a
  Na     0.33333     0.66670     0.84450   Na2a
  Na     0.33333     0.66670     0.65550   Na2a
  F      0.64600     0.12560     0.50000   F1a
  F      0.87440     0.52040     0.50000   F1a
  F      0.47960     0.35400     0.50000   F1a
  F      0.69700     0.72200     0.750000   F2a
  F      0.27800     0.97500     0.750000   F2a
  F      0.02500     0.30300     0.750000   F2a
```

This table became the input for WebATOMS to make the feff.inp file. To address the vacancies on the Na2 sites, we manually halved all the path amplitudes involving this site.

3. Fitting

We tried fitting with Yb in Y1 and Y2 sites, but found that Y1-only worked best. We ended up with 8 paths, ranging in distance from the nearest-neighbor fluorines at 2.45 Å (undistorted structure) to a Na2 shell at 4.18 Å. The free parameters used were overall E_0,

overall S_0^2, distance shifts for the two 1NN fluorine shells, the $\Delta\sigma^2$ for these shells (equal for the two), the $\Delta\sigma^2$for the higher shells, a distance shift relative to the reference structure for the F and Y atoms, and an independent one for the Na1 atom at 3.83 Å. We also tried freeing the occupancy for the Na2 sites, the distance of the Na2 shell at 3.58 Å and the $\Delta\sigma^2$for the Na2 site at 4.18 Å but none of these helped the fit.

4. Results

We find that the EXAFS fits with our substituted $P\bar{6}$ model, but with most distances shorter than in the pure $Na_{1.5}Y_{1.5}F_6$ model, which makes sense as Yb^{3+} is a smaller ion than Y^{3+}. The Yb-F distances were 2.25,2.40 Å (error bar 0.02 Å, reference structure 2.454,2.458 Å). The Na1 at a nominal distance of 3.84 Å is instead at 3.78$\pm$ 0.03 Å, and the one at 4.12 Å in the reference structure is found at 4.12$\pm$0.03 Å. The other distances are 0.05$\pm$0.02 Å greater than in the reference structure.

SI References

(1) Ravel, B.; Newville, M. ATHENA, ARTEMIS, HEPHAESTUS: Data Analysis for X-Ray Absorption Spectroscopy Using IFEFFIT. *J. Synchrotron Radiat.* **2005**, *12* (4), 537–541. https://doi.org/10.1107/S0909049505012719.

Appendix C

SUPPORTING INFORMATION FOR CHAPTER 3

Figure S1: Collapse of gel over time

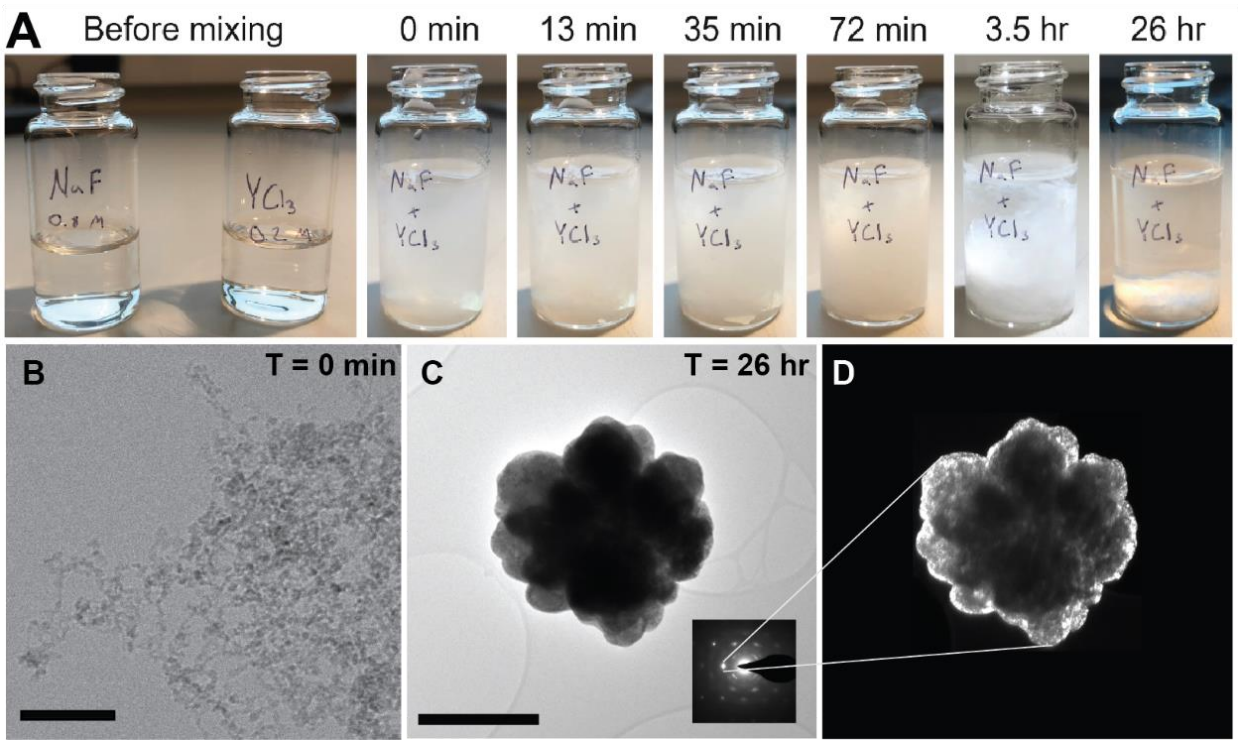

(A) Initial formation of the gel and its collapse over the course of hours. Apparent color variations are solely the result of variations in lighting from a nearby window. (B) Cryo-TEM of the product immediately after formation (scale bar = 50 nm) (C) TEM of the 26-hour product and diffraction (scale bar = 400 nm) and (D) dark field image showing its single crystalline nature (see Fig. 3A)

Figure S2: Powder X-ray Diffraction of the gel

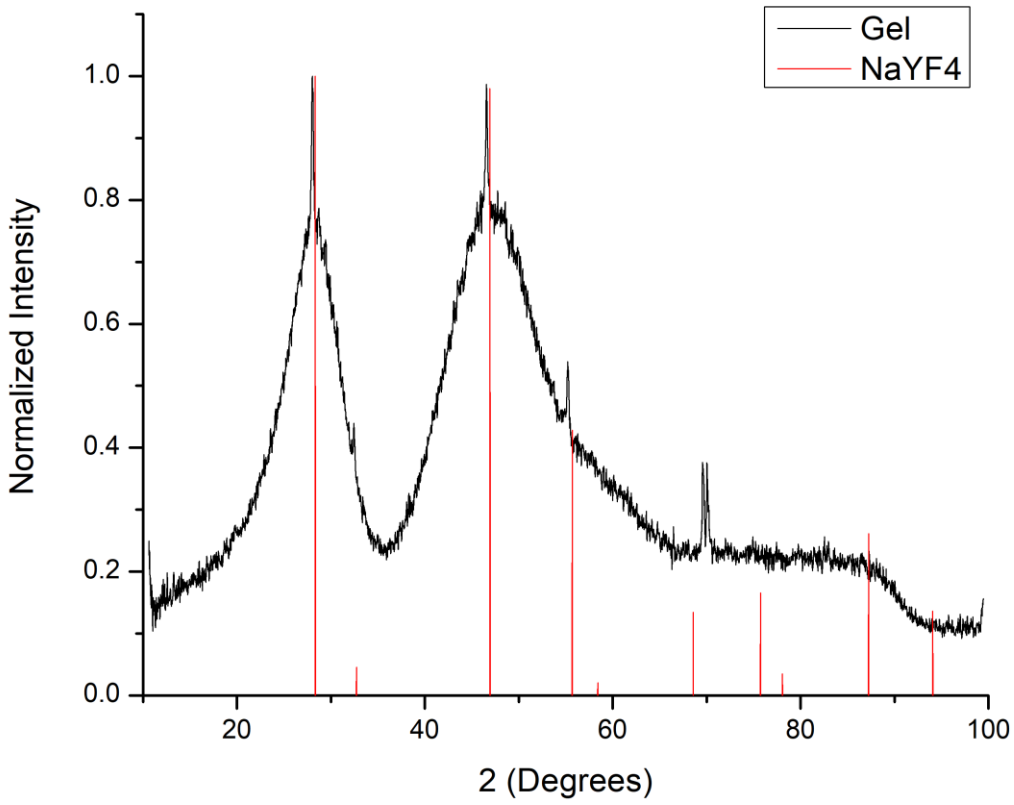

Powder X-ray diffraction measurements of the gel show very broad peaks with spacings consistent with cubic NaYF or YF_3. The sharp peaks correspond to large crystals of α-NaYF that have formed from the gel, as discussed in Fig. S1.

Figure S3: Potentials of Mean Force between YF_n particles

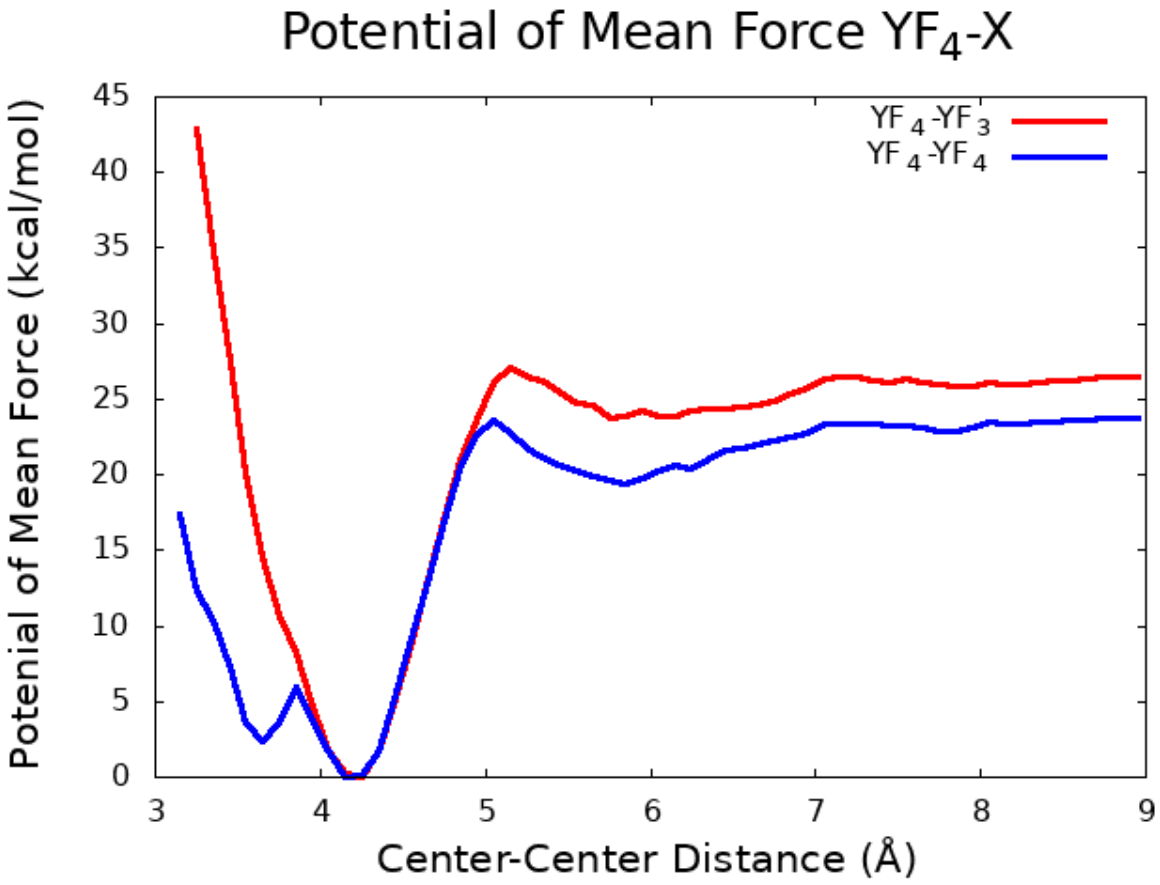

Potential of mean force between a YF_4 ion and either a YF_3 molecule or another YF_4 ion, respectively, in vacuum. Both cases show a strong attractive force at about 4.2Å, indicating that they would be likely to aggregate.

Figure S4: Beam-induced crystallization of the gel

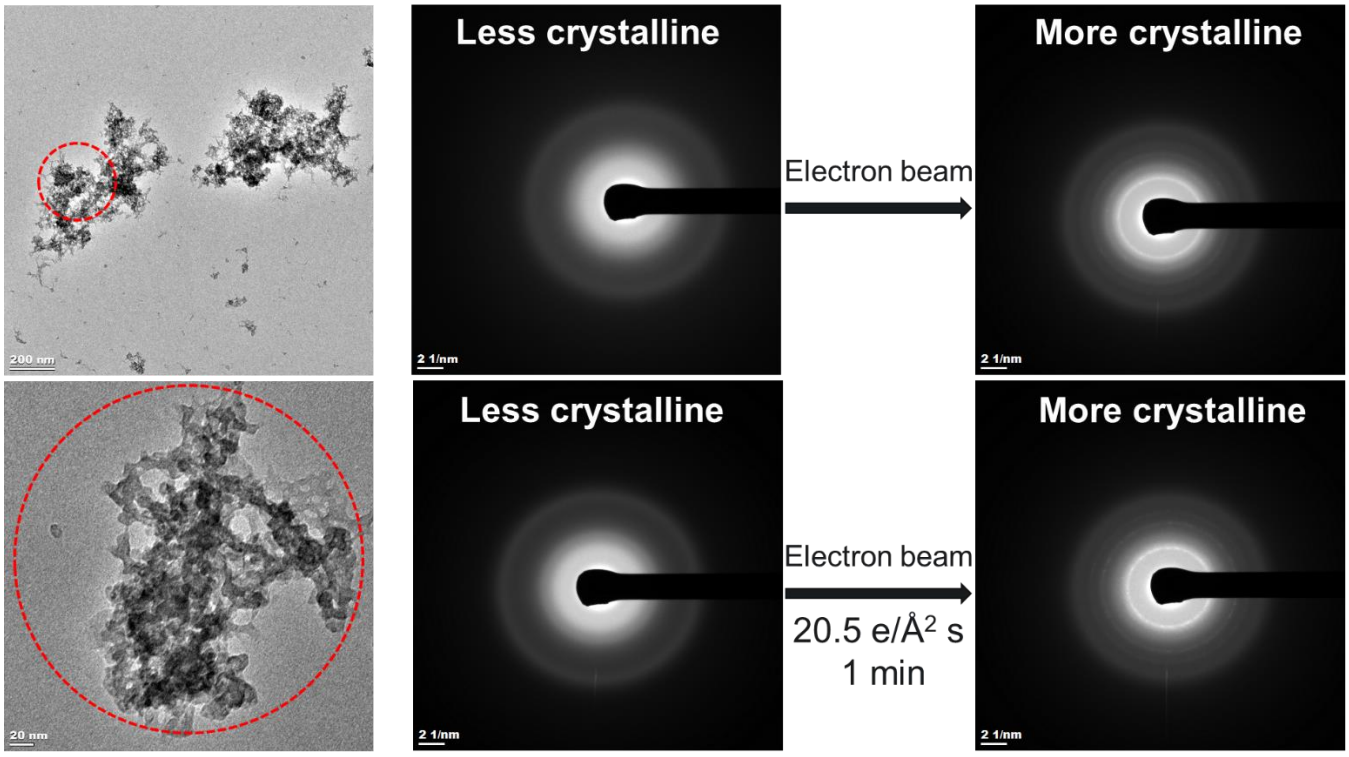

Standard TEM/SAED experiments on the gel in vacuum induced significant crystallization in the gel, as shown by the sharper rings in the SAED patterns. There is no significant change to the morphology of the particles during that time.

Figure S5: STEM-EDS data

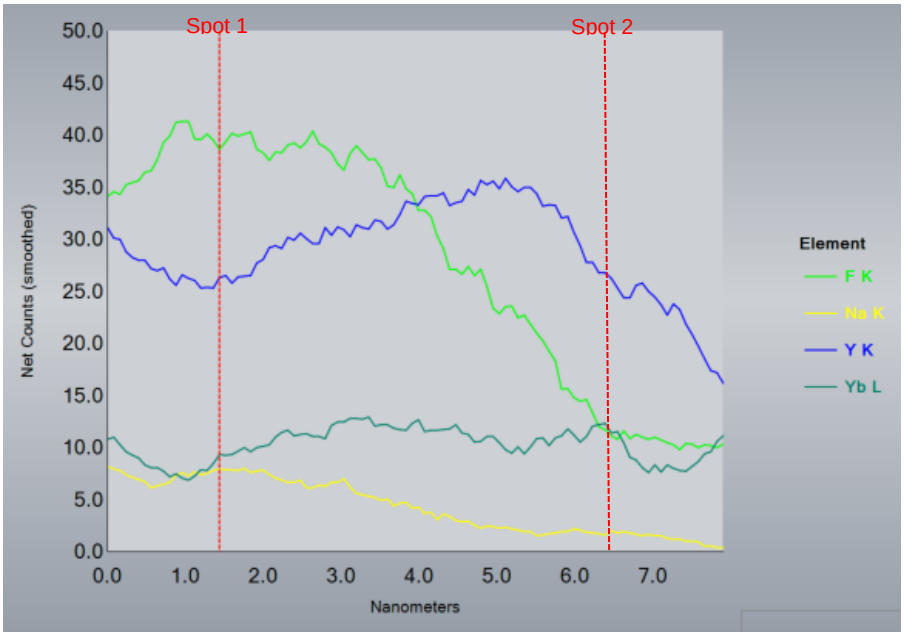

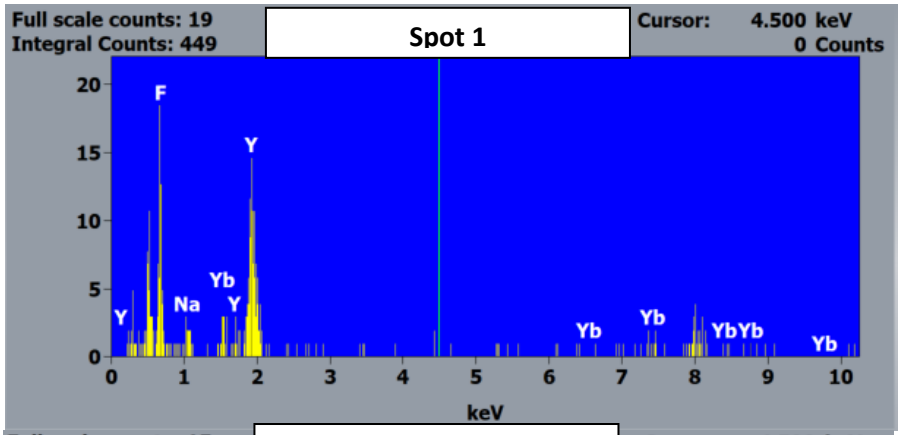

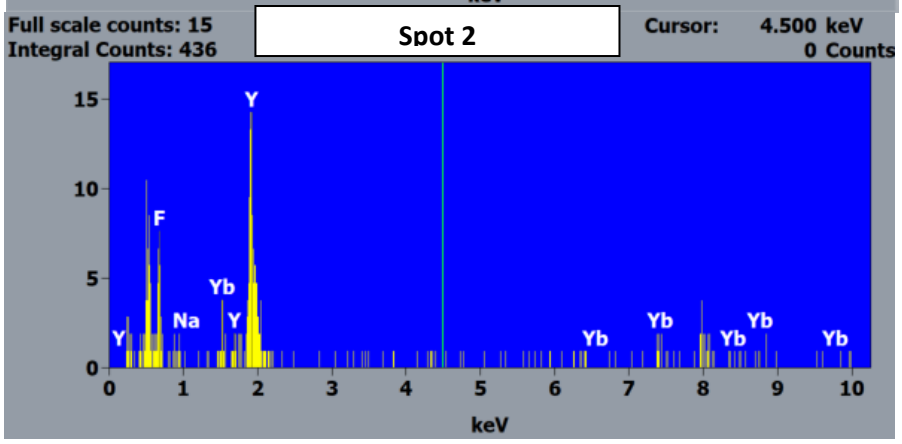

Figure S6: ^{23}Na NMR

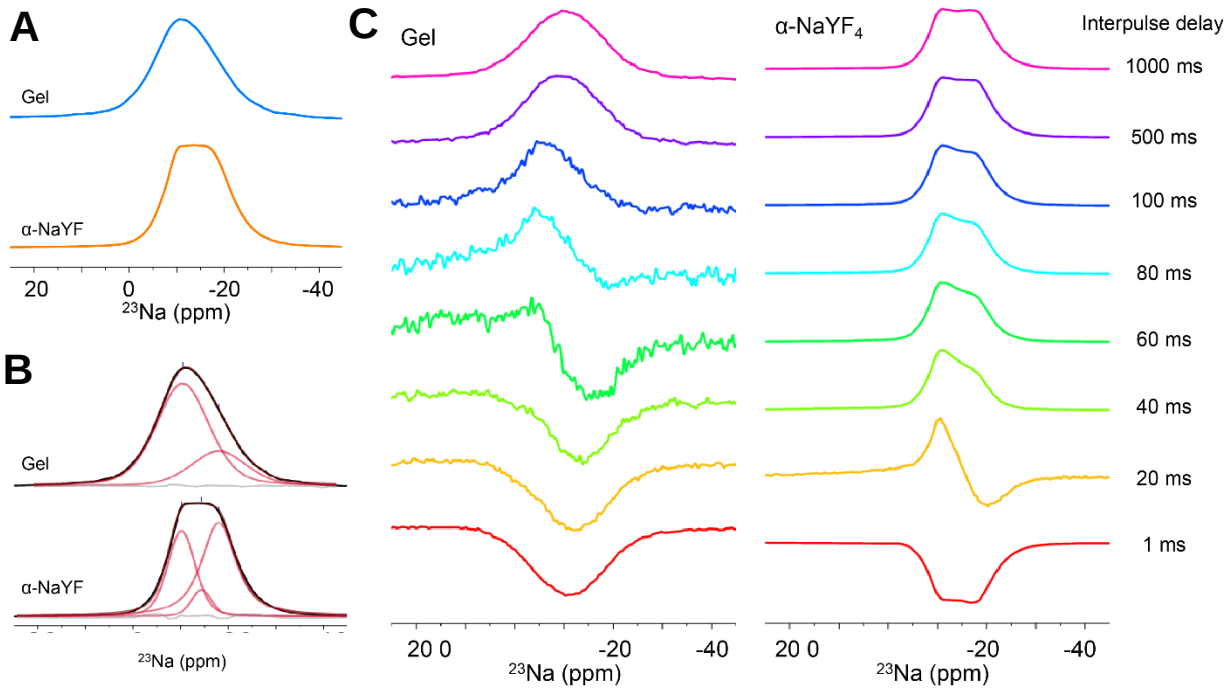

(A) Single-pulse ^{23}Na NMR of the gel and the α-NaYF. Excitation by a hard pulse at 86 kHz or a soft pulse at 17 kHz produce nearly identical results. (B) Deconvolution of (A) showing two major resonances centered at -18 ppm and -9.5 ppm, which are assigned to Na sites in the bulk and at the surface or near defects, respectively. (C) ^{23}Na inverse recovery spectra of the gel and the α-NaYF after varying Interpulse delay times.

Figure S7: MD simulation of orthorhombic YF_3

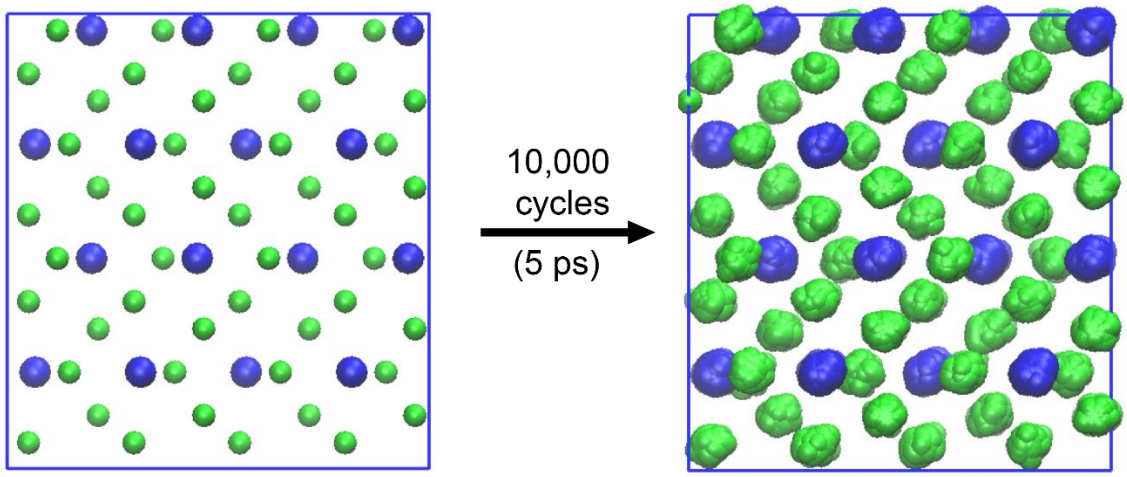

MD simulation time lapse of the orthorhombic YF_3 structure showing minimal disorder following 10,000 pulses of 0.5 fs each

Figure S8: MEPs of ions moving through the simulated cubic YF_3 lattice

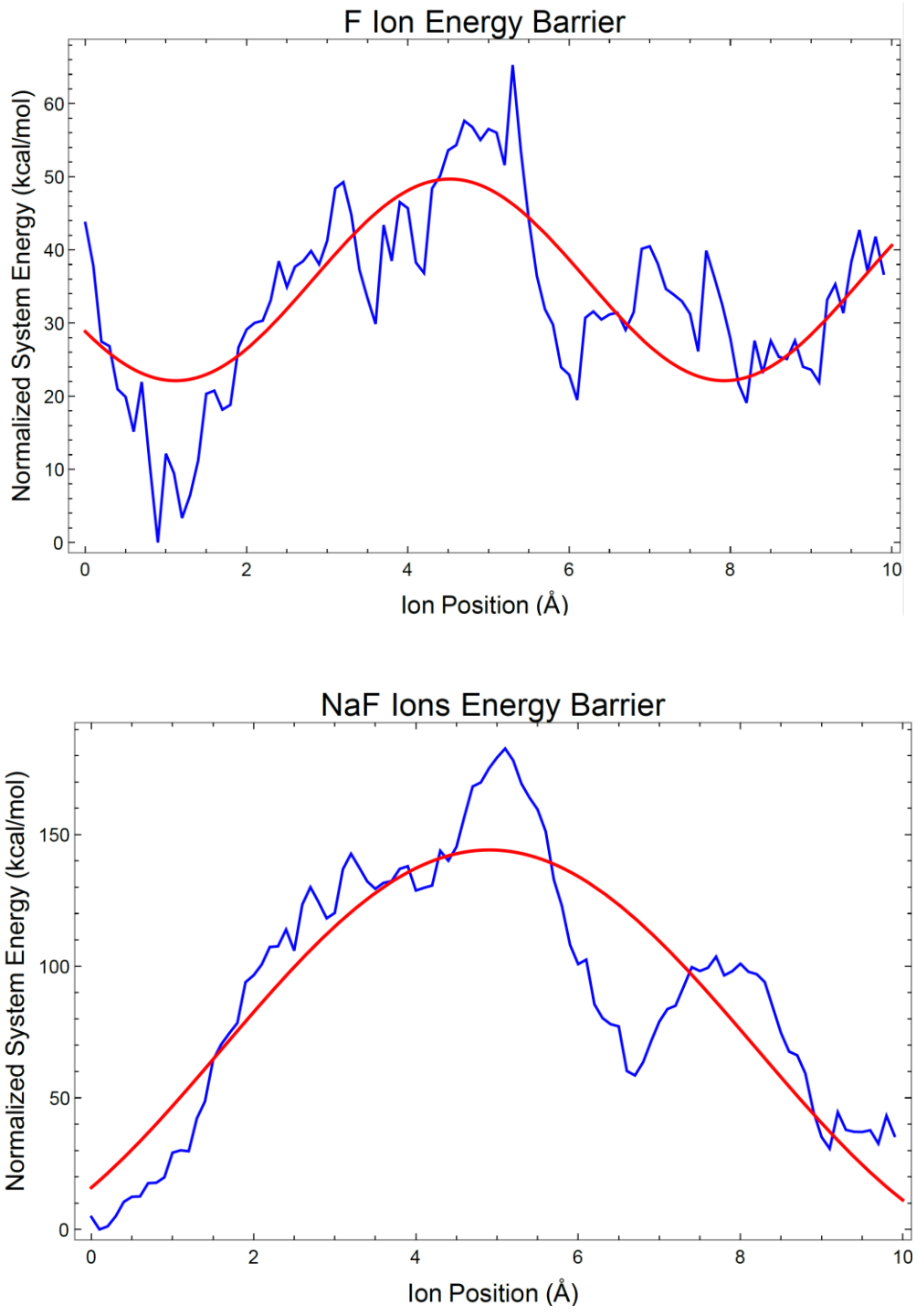

Figure S9: Selection of crystallization pathway and final product by altering ratio

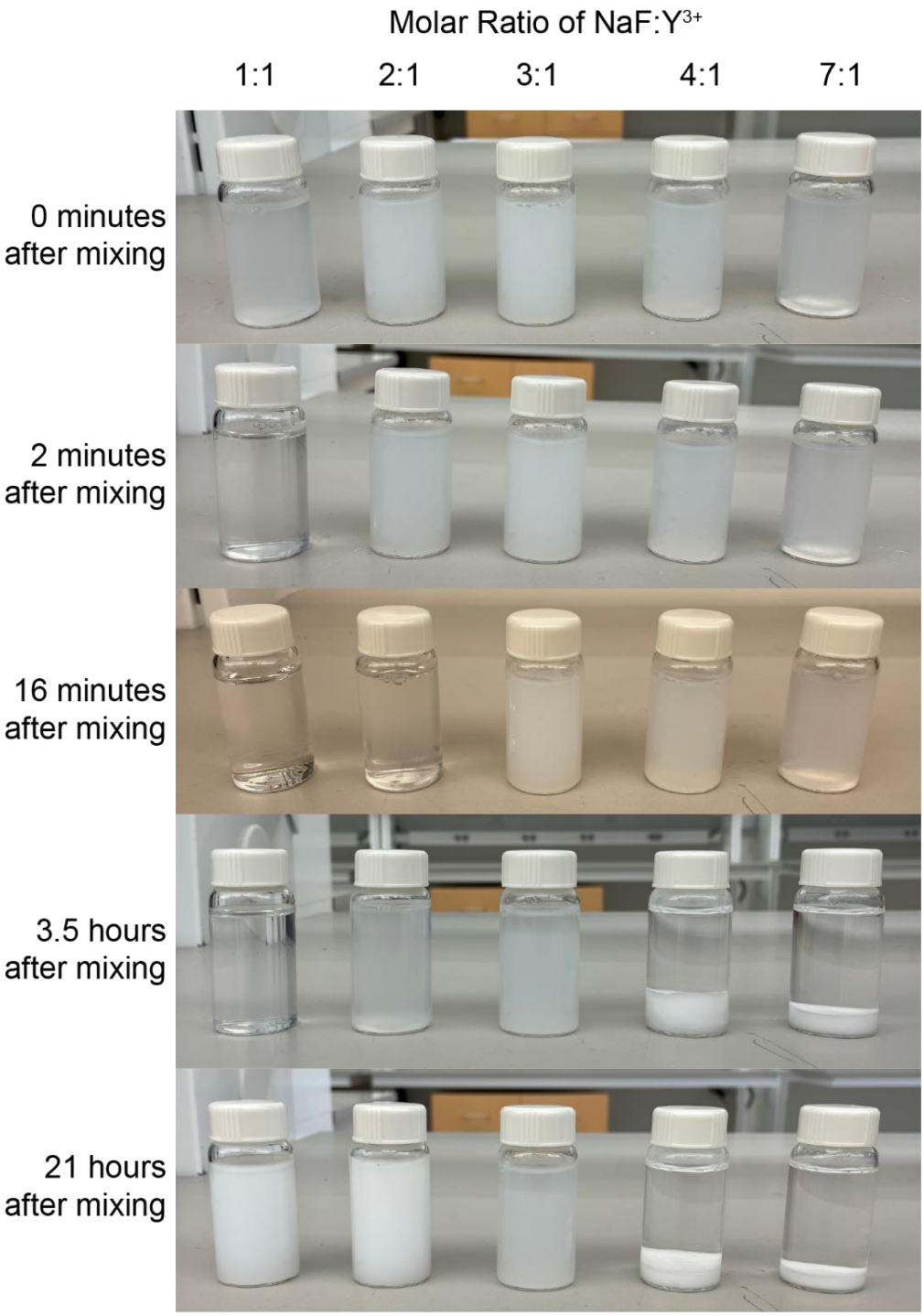

Parallel reaction of $Y(NO_3)_3$ with NaF in varying ratios, showing the multi-step process for the NaYF crystallization occurring for NaF-excess reactions and redissolution and subsequent nucleation of orthorhombic YF_3 occurring in NaF-deficient reactions. Both processes seem to occur simultaneously in the YF_3-stoichiometric reaction.

Figure S10: Cycling data of NaYF gel as a negative electrode for Li-ion batteries

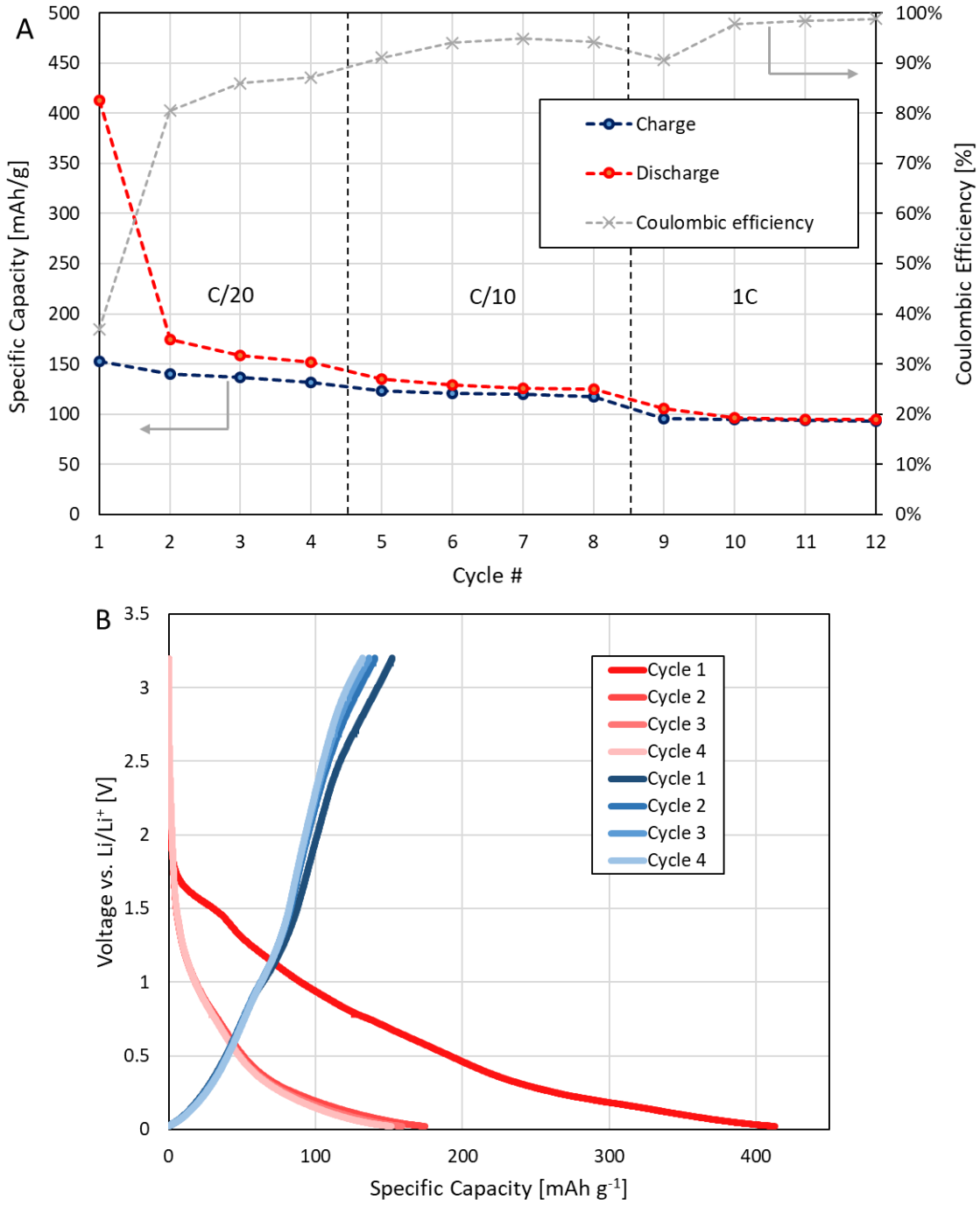

(A) Charge/discharge capabilities and coulombic efficiency against cycle number 1-4 corresponding to C/20 rate, cycle 5-8 corresponding to C/10 rate, cycle 9-12 corresponding to 1C rate. (B) The first four cycles of galvanostatic charge/discharge curves of NaYF gel. Red corresponding to discharge (lithiation) and blue corresponding to charge (delithiation), showing reversible cycling at C/20 rate.

Figure S11: Cycling data of NaYF gel as a negative electrode for Na-ion batteries

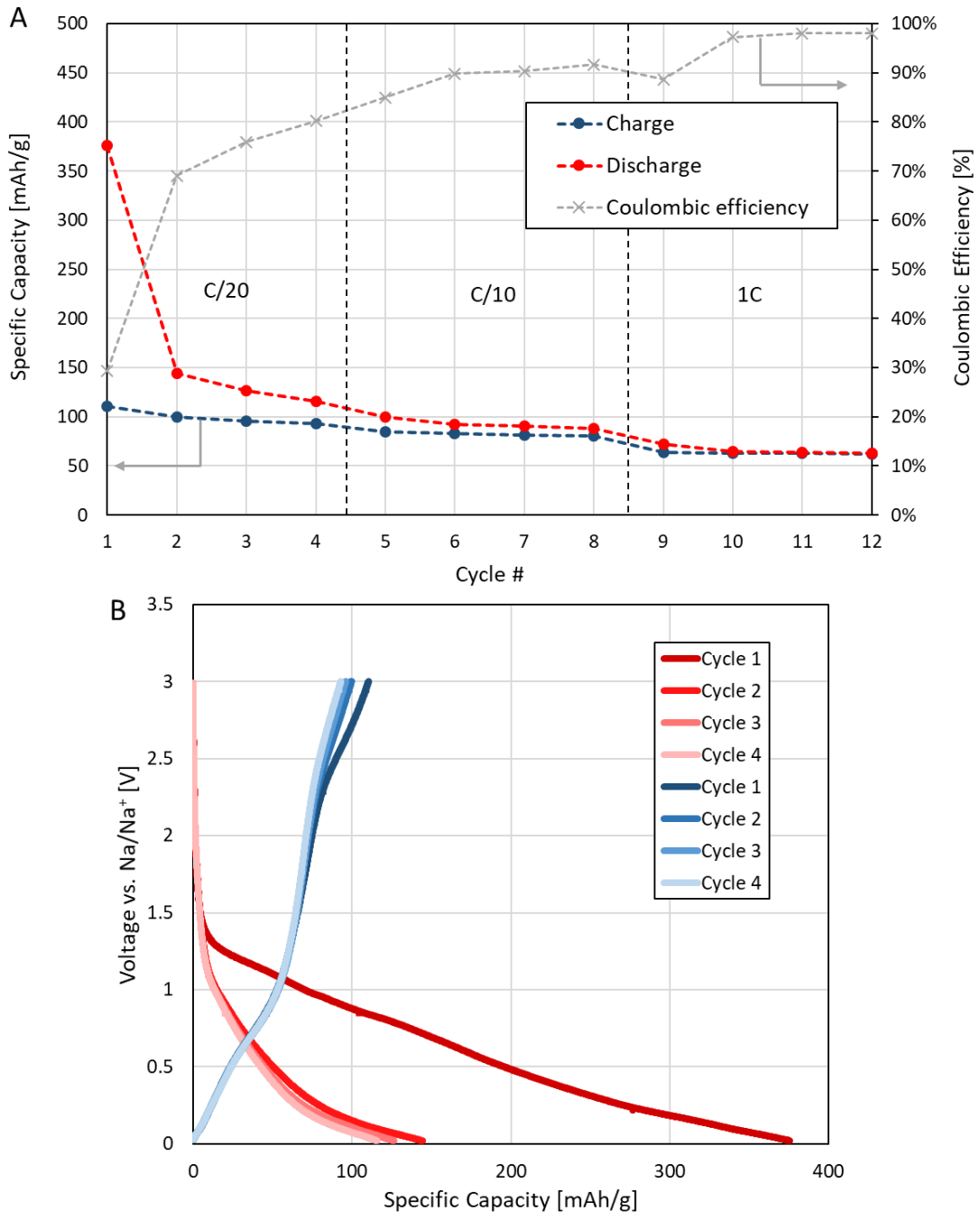

(A) Charge/discharge capacities and coulombic efficiency against cycle number 1-4 corresponding to C/20 rate, cycle 5-8 corresponding to C/10 rate, cycle 9-12 corresponding to 1C rate. (B) The first four cycles of galvanostatic charge/discharge curves of NaYF gel. Red corresponding to discharge (sodiation) and blue corresponding to charge (desodiation), showing reversible cycling at c/20.

Figure S12: Laser refrigeration of NaYF gel

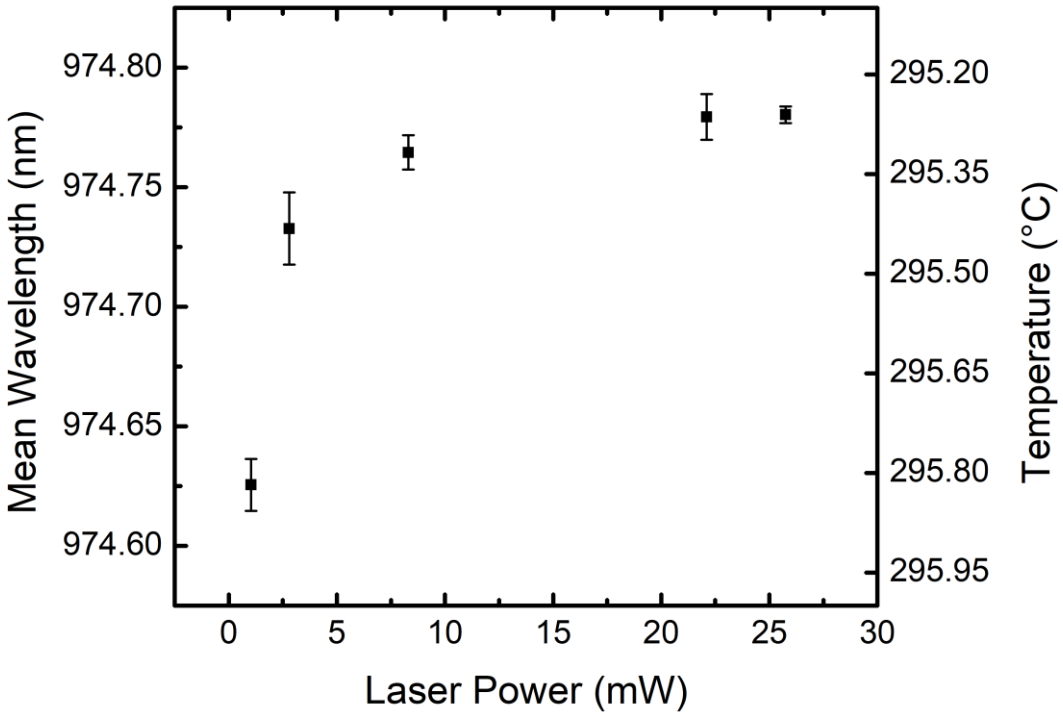

Laser refrigeration data for 10% Yb^{3+} doped NaYF gel, showing a decrease in temperature of up to 0.55°C as the 1020 nm laser power is increased to 25 mW.

SI Methods:

Battery materials

Carbon black (Vulcan® XC72, CABOT), sodium carboxymethyl cellulose (CMC, Mw ~90,000, Sigma Aldrich), sodium perchlorate (ACS reagent, >98%, Alfa Aesar), propylene carbonate (Anhydrous, 99.7%, Sigma Aldrich), 4-fluoro-1,3-dioxolan-2-one (FEC, >98% TCI America), 1M solution of lithium hexafluorophosphate in ethylene carbonate/dimethyl carbonate (EC/DMC, Sigma Aldrich), Lithium ribbon (99.9%,Sigma-Aldrich), Sodium foil (99.95%, Sigma Aldrich), Celgard Separator (MTI corporation), glass microfiber separator (GF/F, Whatman),Cu foil (>99.99%, 9 µm thickness, MTI corporation), CR2032-type coin cell parts (MTI corporation)

Electrode Fabrication, Coin Cell Assembly, and Electrochemical Testing

In a typical negative electrode preparation, $NaYF_4$ (~200 mg, 64 wt%), conductive additives carbon black (~65 mg, 21 wt%), and CMC dissolved in nanopure water with the density of 67 mg/mL (15 wt%) were thoroughly mixed using mortar and pestle. The slurry was then doctor-bladed (38 µm thickness) onto a copper foil current collector and dried on a hot plate at 80 °C in air. Electrodes were further dried in a vacuum oven at 90 °C with <15 mbar pressure overnight. CR2032-type coin cells were assembled in an argon-filled glove box (O_2 < 1 ppm, H_2O < 1 ppm) using 15 mm punch out NaYF electrode, elemental lithium metal as positive electrode, a glass fiber separator, and 1.0 M $LiPF_6$ in EC/DMC with 10% w/v FEC for the lithium-ion battery, and sodium metal and 1.0 M $NaClO_4$ in an electrolyte solution of 90% w/v propylene carbonate and 10% w/v FEC for the sodium-ion battery. All electrochemical testing was performed with a MACCOR Series 4000M 64-Channel Automated battery test system using 0.1 mA current that corresponds to a current density of 143 mA g^{-1}. Gravimetric capacities were calculated based on the weight of the active material in the electrode which averaged around 1 mg.

Laser refrigeration

Laser refrigeration measurements were performed by attaching the gel sample to an optical fiber mounted inside an optical cryostat (Janis ST500). The Yb^{3+} cations were excited with a 1020 nm diode laser (QPhotonics QFBGLD-1020-400) to induce luminescent upconversion, cooling the gel. The upconverted photoluminescence of the NaYF gel was collected at several different laser irradiances. The mean fluorescent wavelength for each spectrum was compared against calibrations at known temperatures to determine cooling efficiency.

Appendix D

SUPPORTING INFORMATION FOR CHAPTER 4

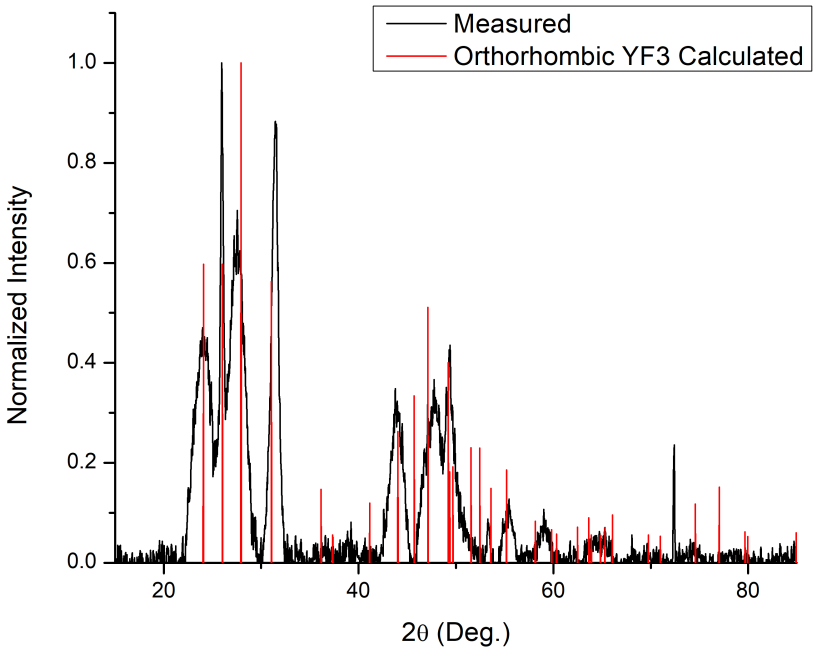

Figure S1: Powder x-ray diffraction of the YF_3 particles compared to the calculated peaks for orthorhombic YF_3

Appendix E

LIST OF PUBLICATIONS

- Bard, A. B.; Lim, M. B.; Zhou, X.; Rodríguez Manzo, J. A.; Alsem, D. H.; Pauzauskie, P. J. Observation of Void Formation in Cubic $NaYF_4$ Nanocrystals Using In Situ Heating Transmission Electron Microscopy.*Microscopy and Microanalysis* **2019**, *25*, 1496–1497, DOI: 10.1017/S1431927619008213

- Bard, A. B.; Zhou, X.; Xia, X.; Zhu, G.; Lim, M. B.; Kim, S. M.; Johnson, M. C.; Kollman, J. M.; Marcus, M. A.; Spurgeon, S. R.; Perea, D. E.; Devaraj, A.; Chun, J.; De Yoreo, J. J.; Pauzauskie, P. J. A Mechanistic Understanding of Nonclassical Crystal Growth in Hydrothermally Synthesized Sodium Yttrium Fluoride Nanowires.*Chemistry of Materials* **2020**, *32*, 2753–2763, DOI: 10.1021/acs.chemmater.9b04076

- Bard, A. B.; Felsted, R. G.; Ganas, A. S.; Pant, A.; Gupta, C.; Chen, Y.; Nakouzi, E.; Jin, B.; Washton, N. M.; LaCount, M. D.; Mundy, C. J.; Schenter, G. K.; Chun, J.; Spurgeon, S. R.; Lee, G. K.; Holmberg, V. C.; Brush, L. N.; De Yoreo, J. J.; Pauzauskie, P. J. Chemically-Driven Multi-Step Crystallization in the Synthesis of Sodium Yttrium Fluoride Via a Porous, Electrochemically-Active Intermediate.*In Submission* **2023**

- Bard, A. B.; Chen, Y.; LaCount, M. D.; Mundy, C. J.; Schenter, G. K.; Liu, J. I.; De Yoreo, J. J.; Pauzauskie, P. J. Concentration-Selective Nucleation "Switch" in the YF_3-$NaYF_4$ System.*In Preparation* **2023**

- Bard, A. B.; Felsted, R. G.; Stöhr, R.; Wrachtrup, J.; Spurgeon, S. R.; Perea, D. E.; Pauzauskie, P. J. Microfabrication from Bulk and Measurement of Nanoscale Diamond Tips for Atom Probe Tomography.*In Preparation* **2023**

- Felsted, G.; Pant, A.; Bard, A. B.; Xia, X.; Luntz-Martin, D. R.; Dadras, S.; Zhang, S.; Vamivakas, N.; Pauzauskie, P. J. In *Photonic Heat Engines: Science and Applications IV*, ed. by Kuno, M. K.; Seletskiy, D. V., SPIE: 2022, p 18, DOI: 10.1117/12.2611615

- Xia, X.; Pant, A.; Zhou, X.; Dobretsova, E. A.; Bard, A. B.; Lim, M. B.; Roh, J. Y. D.; Gamelin, D. R.; Pauzauskie, P. J. Hydrothermal Synthesis and Solid-State Laser Refrigeration of Ytterbium-Doped Potassium-Lutetium-Fluoride (KLF) Microcrystals. *Chemistry of Materials* **2021**, *33*, 4417–4424, DOI: 10.1021/acs.chemmater.1c00420

- Zhou, X.; Xia, X.; Smith, B. E.; Lim, M. B.; Bard, A. B.; Pant, A.; Pauzauskie, P. J. Interface-Dependent Radiative Lifetimes of Yb^{3+}, Er^{3+} Co-doped Single $NaYF_4$ Upconversion Nanowires. *ACS Applied Materials & Interfaces* **2019**, *11*, 22817–22823, DOI: 10.1021/acsami.8b17271

- Felsted, R. G.; Chun, J.; Schenter, G. K.; Bard, A. B.; Xia, X.; Pauzauskie, P. J. Optical assembly of nanostructures via surface roughness. *In Submission* **2023**

- Felsted, R. G.; Pant, A.; Lu, L.; Bard, A. B.; Beck, R. A.; Bishop, B.; Erickson, C.; Perea, D. E.; Spurgeon, S. R.; Gamelin, D. R.; Holmberg, V. C.; Li, X.; Pauzauskie, P. J. Colloidal Semiconductor Quantum Dots in Dichalcogenide Cavities Prepared through Pulsed Laser Deposition. *In Preparation* **2023**